

**METAL ORGANIC FRAMEWORKS BASED MICROCANTILEVER  
GAS SENSORS FOR DETECTION OF VOLATILE ORGANIC  
COMPOUNDS**

A Thesis  
Presented to  
The Academic Faculty

by

Ilya Ellern

In Partial Fulfillment  
of the Requirements for the Degree  
Master of Sciences in the  
Woodruff School of Mechanical Engineering

Georgia Institute of Technology  
August 2013

**COPYRIGHT 2013 BY ILYA ELLERN**

**METAL ORGANIC FRAMEWORKS BASED GAS SENSORS FOR  
DETECTION OF VOLATILE ORGANIC COMPOUNDS**

Approved by:

Dr. Peter Hesketh, Advisor  
School of Mechanical Engineering  
*Georgia Institute of Technology*

Dr. Todd Sulchek  
School of Mechanical Engineering  
*Georgia Institute of Technology*

Dr. Nazanin Bassiri-Gharb  
School of Mechanical Engineering  
*Georgia Institute of Technology*

Date Approved: June 14, 2013

To  
My parents for unconditional love, motivation and support  
And to  
My loved ones for their encouragement

## ACKNOWLEDGEMENTS

Many people have provided guidance, support, ideas, time and effort throughout this project and for the past three years. Inside and outside of work, these people made the graduate school experience worthwhile.

I would especially like to thank my advisor, Dr. Peter Hesketh, for his healthy degree of optimism when experiments disappointed and all seemed lost. For his guidance and zest for research which was an inspiration to keep going and not give up. I would also like to thank him for the warm and friendly atmosphere he garnered in his group; it encouraged sharing of ideas, insightful discussions and a productive work environment. I can't thank him enough for providing me with the opportunity to work on a truly intriguing project and for teaching me so much.

Next, I would like to thank my group members who encouraged me to continue to work hard when motivation was low, provided advice when I was stumped and lost, delivered comic relief when it was sorely needed and reminded me the important things in life when I forgot. I would also like to thank my undergraduate research assistants Kevin, Victoria, Jeff and Jennifer for helping me probe thousands of devices and characterize them. Without their dedication and patience the project would not have progressed nearly this fast.

I am also thankful to Dr. Lee, Dr. Choudhury and my friend Dr. Anandram Venkatasubramanian for providing the foundation of my project. Without their prior work, I would have no initial devices for experiments or a system to test them with. Also thanks to the cleanroom staff at the Georgia Tech IEN Cleanroom for training me on various equipment pieces, providing support and technical expertise. Especially, I would

like to thank Dr. Gary Spinner, Hang Chen and Vinny Nguyen for providing me with the opportunity to work at the cleanroom for a summer.

I want to thank Sandia National Laboratories for providing support for my project as well as growing all the coatings on our devices. Thanks to Dr. Mark Allendorf for his numerous comments on publication drafts, suggestions for improvements of test protocols and insight into the world of MOFs. I would also like to thank Vitalie Stavila and Alex Robinson for their suggestions on characterization protocols and new experimental setup design.

Without great friends and family, this endeavor would have concluded before it began. I would like to thank them for believing in me, encouraging me to continue going, and providing distractions from work when they were needed. In addition, I would like to thank my sister for life advice and anecdotes that always seemed to be able to cheer me up. A special gratitude is expressed to my grandparents for their words of encouragement and insight on life when I decided to pursue higher education. Especially, I would like to thank my grandfather Misha for his enthusiastic encouragement of my studies.

I want to thank my parents. It is with their help for the last 24 years that I became who I am today. Thanks for always being there for me, believing in me and motivating me to set out on my own path. I can't begin to describe how lucky I feel for having them as my parents. All opportunities and accomplishments I owe to them.

Lastly, I would like to thank my best friend Sabrina Soh, who has kept me company every day on the phone. Whether it was during my late night drives from work or while working alone in the lab on weekends. She truly knows me better than I know

myself. She kept me truthful when I was dishonest with myself, built me up when I failed and listened to me when I needed someone to listen. I would like to thank her for being the voice in the back of my head reminding me not to procrastinate, continue working and studying all throughout graduate school.

# TABLE OF CONTENTS

	Page
ACKNOWLEDGEMENTS	iv
LIST OF TABLES	xi
LIST OF FIGURES	xii
NOMONCLATURE	xviii
SUMMARY	xx
<u>CHAPTER</u>	
1 INTRODUCTION	1
1.1 Motivation	1
1.2 Overview of Microcantilevers for Sensing Applications	3
1.2.1 Cantilevers in Sensing Applications	3
1.3 Metal Organic Frameworks	5
1.3.1 Operational Principles of Metal Organic Frameworks	6
1.3.1.1 Synthesis of Metal Organic Frameworks	7
1.3.1.2 Working Principles of Metal Organic Frameworks for Gas Separation	8
1.3.2 Summary of Key Features of MOFs	10
1.4 Metal Organic Frameworks for Piezoresistive Sensors	10
1.5 Concluding Remarks	12
2 EXPERIMENTAL SETUP FOR MEASUREMENT OF CANTILEVER SENSORS RESPONSE TO GASES AND GAS MIXTURES	13
2.1 Introduction	13
2.2 Original Experimental Flow Setup and Measurement Approach	13
2.2.1 Packaging of Sensor Arrays	15
2.2.2 Instrumentation	15
2.3 Experimental Setup Modifications	16

2.3.1	Disadvantages of Old Experimental Setup	16
2.3.1.1	Temperature Control	16
2.3.1.2	Analyte Quality, Cost and Waste Management	19
2.3.1.3	Flow System	20
2.3.1.4	Instrumentation	21
2.4	New Experimental Setup Design	21
2.4.1.1	Data Acquisition System Improvements	21
2.4.1.2	Test Cell Redesign	23
2.4.1.2.1	Electrical Connections	23
2.4.1.2.2	Test Cell Physical Design	26
2.4.2	Improved Procedure for Analyte Handling	28
2.5	Mixed Experimental Setup	30
3	FABRICATION OF PIEZORESISTIVE MICROCANTILEVERS	32
3.1	Fabrication of Euler-Bernoulli Piezoresistive Microcantilevers	32
3.2	Fabrication of Temperature Compensated Wide Piezoresistive Microcantilever Plates	35
3.2.1	Modeling Results	35
3.2.2	Layout and Packaging	36
3.2.2.1	Limitations of Old Device Layout	36
3.2.2.2	Optimized Cantilever Die Design and Temperature Compensation	39
3.2.2.3	Other Designs Fabricated on the Wafer	40
3.2.3	Fabrication Process	43
3.2.4	Fabrication Challenges	47
3.2.4.1	Selecting Stress Compensation Values	47
3.2.4.2	Tuning SiO <sub>2</sub> Recipe	48
3.2.4.3	Selection of DRIE Tool	49

4	CHARACTERIZATION OF PIEZORESISTIVE MICROCANTILEVERS	53
	4.1 Temperature Response	53
	4.2 Laser Mass Characterization	56
	4.3 Characterization Protocol	59
	4.3.1 Initial Probing and Imaging	59
	4.3.2 Metal Organic Frameworks Film Characterization	62
	4.3.3 Final Pre-Test Characterization	63
5	RESPONSE OF METAL ORGANIC FRAMEWORKS ON OLD TYPE CANTILEVERS	65
	5.1 HKUST-1 (CuBTC) Response	65
	5.1.1 Introduction to HKUST-1	65
	5.1.2 Conversion of Voltage to Resistance	66
	5.1.3 Sample Preparation Procedure	67
	5.1.3.1 Mixed Setup Dehydration Procedure	67
	5.2 Response of HKUST-1 to VOCs on Old Type Devices	68
	5.2.1 Measurement of Step Response	68
	5.2.2 Measurement of Mixed Response	71
	5.3 Adsorption Results	74
	5.4 Discussion	75
	5.5 Response of Mixtures of Analytes	82
	5.6 Reliability and Stability of MOF Coated Microcantilevers	84
	5.6.1 Reliability and Precision	84
	5.7 Sensitivity and Limits of Detection	87
	5.8 Low Power Operation	88
	5.9 Summary of Results	88
6	RESPONSE OF METAL ORGANIC FRAMEWORKS ON NEW TYPE DEVICES	90

6.1 Comparison of Noise Levels	90
6.2 External Heating Methods	92
6.3 HKUST-1 Response on New Design with Heaters	94
6.3.1 New Setup Dehydration Procedure	94
6.3.2 Experimental Results and Discussion	95
7 CONCLUSION AND FUTURE WORK	98
7.1 Concluding Remarks	98
7.2 Future Work	102
APPENDIX A: FABRICATION PROCESS OUTLINE	104
APPENDIX B: PACKAGING INSTRUCTIONS	127
APPENDIX C: SAMPLE RESPONSE DATA	131
REFERENCES	133

## LIST OF TABLES

Table 1-1: A table summarizing microcantilever deflection measurement techniques [1].	4
Table 1-2: Summary of MOFs identified as potential selective layers for piezoresistive microcantilever sensors.	11
Table 2-1: Requirements list.	25
Table 3-1: Die distribution for new wafer layout.	40
Table 3-2: Various process parameters used to adjust the etch profile and reduce silicon grass.	52
Table 4-1: AFM frequency measurements before and after coating with MOF. It was estimated that frequency should be reduced by 700 Hz.	57
Table 5-1: Concentration to partial pressure conversion chart.	70
Table 5-2: Sample mixing flows and resulting concentrations for mixed water test.	72
Table 5-3: Vapor pressure models [32].	72
Table 5-4: Calculated time constants for HKUST-1 based on CuBTC on SAM response.	79
Table 5-5: Physical attributes of analytes grouped by quality of response data.	80
Table 5-6: $C_H$ and $\alpha$ values of alcohols compared to water.	87
Table 5-7: Measured data in certain PPM ranges can be used to estimate limits of detection. Such estimates were not very reliable.	88
Table 5-8: Summary of analyte properties and response.	89

## LIST OF FIGURES

Figure 1-1: Examples of a few metal ions and organic linkers that can be used for MOF synthesis [5].	5
Figure 1-2: Layer by layer growth of HKUST-1 on OH functionalized SAM [11].	6
Figure 1-3: Number of publications on MOFs [7].	9
Figure 2-1: (A) Wirebonded device inside it's package. (B) Package inside the test cell.	13
Figure 2-2: Schematic of gas delivery system via mass flow controllers and hydrator to the test cell.	14
Figure 2-3: Wheatstone bridge additive configuration.	15
Figure 2-4: This plot illustrates temperature oscillation when active temperature control was implemented.	17
Figure 2-5: Temperature controlled setup for old design microcantilevers.	18
Figure 2-6: Old experimental setup.	20
Figure 2-7: Interface of the LabView data acquisition system. Data for two bridges is collected simultaneously. Temperature of the flow cell, as well as gas flow rates, current and incoming voltage are all recorded.	22
Figure 2-8: Top left - 25 pin D-Sub socket. Bottom left - pins connected to cantilevers. Right - a devices wirebonded to the 20 pin LCC package.	23
Figure 2-9: Diagram showing distribution box for reading signals and powering the Wheatstone bridges on the new devices. All communications between the devices and this box were sent through a single six foot long D-Sub 25 pin cord.	24
Figure 2-10: New flow cell to test next generation devices. Low signal noise and high thermal stability.	26
Figure 2-11: Test cell with cover removed showing the shutoff valves.	28
Figure 2-12: Glove box used for device storage and analyte loading.	30

Figure 2-13: Mixed flow setup. Hydrators from the new test cell were used to expose old style devices in the old test cell.	31
Figure 3-1: Cross sectional view of different layer configurations.	32
Figure 3-2: A. CAD model of a microcantilever array. B. Schematic of a piezoresistive microcantilever.	33
Figure 3-3: Modeling results for old type microcantilevers showing improved response of HKUST on SiO <sub>2</sub> substrates [21].	34
Figure 3-4: Scanning Electron Microscope (SEM) image of old design piezoresistive microcantilever.	34
Figure 3-5: Optimized dimensions for new microcantilever sensors	36
Figure 3-6: Old wafer layout.	37
Figure 3-7: Illustration of wirebonding angles seen with old package and device.	38
Figure 3-8: Sample layout of the new die. Microcantilevers were surrounded on all sides by the die to protect devices from physical damage.	39
Figure 3-9: Wafer layout.	41
Figure 3-10: (A) Die layout for 3 devices with different shape heaters. (B) Disc layout. (C) Original cantilever layout. (D-F) Different shapes of heating resistors with no cutouts. (G-I) Heating resistors with cutouts. (J). Disk. (K) Old type cantilever.	42
Figure 3-11: Highlights of the fabrication process.	44
Figure 3-12: Multiple contact windows to lower resistance to piezoresistive layer.	44
Figure 3-13: Reflectance of Aluminum, Silver and Gold at varying wavelengths [26].	45
Figure 3-14: All the devices on process wafer 1 were damaged with wide portions of the cantilever breaking off and the middle section with piezoresistors A and B remaining intact but highly stressed. Left- optical image of broken off wide portion of cantilever. Right – SEM or remaining center piezoelement.	47

Figure 3-15: COMSOL model with estimated original layer stresses. Curvature of device in model reflected SEM images of damaged devices. Stresses at the base and around the piezoresistor were above failure threshold for materials.	47
Figure 3-16: COMSOL model predicted 400nm of SiO <sub>2</sub> at -300MPa of compressive stress on top would flatten the beam and reduce stresses below failure threshold.	48
Figure 3-17: STS PECVD 2 film stress vs. N <sub>2</sub> O/SiH <sub>4</sub> ratio.	49
Figure 3-18: Left - cool grease residue seen after release of a test wafer. Right - test wafer released using STS HRM with crystal bond.	50
Figure 3-19: Etch profile of STS ICP with Module 1 through etch.	51
Figure 3-20: SEM images of original recipe where silicon grass can be seen (left). Optimized recipe with well-defined trenches and no silicon grass growth (right).	52
Figure 4-1: Temperature calibration of an old type cantilever.	53
Figure 4-2: Temperature calibration of a new type wide device without heater element or cutouts. Resistor A was used for measurements.	54
Figure 4-3: Shows significant effect of heater length (resistor E) on temperature coefficient effects comparing cantilever 2 (top image) to cantilever 3 (bottom image). In both cases resistor A was measured for temperature calibration purposes.	55
Figure 4-4: Temperature compensated bridge response to temperature from 23°C to 100°C. The voltage values correspond to 2.0 Ω/°C.	55
Figure 4-5: Lorentzian model fit to measured frequency using AFM optics.	56
Figure 4-6: Average values of fundamental frequencies for 10 cantilevers of old type prior to coating.	57
Figure 4-7: Custom fabricated laser setup.	58
Figure 4-8: Left - backside view of support grid before separation from carrier. Right - Released wafer with a few missing dies illustrating ease of removal of single dies.	59

Figure 4-9: Wentworth labs probe station. Capable of probing and taking color images using custom computer software. CREE LED source was fitted to improve image quality and to enable computer control of the light intensity.	60
Figure 4-10: Shows characterization process and serial number explanation. This storage system enabled tracking of each device to a particular location on a particular wafer.	61
Figure 4-11: Both images are for process wafer 2. (A) Shows how many working resistors are available on suspended structures. (B) Shows how many complete bridges there are per die.	62
Figure 4-12: (A) XRD pattern measured vs. calculated for CuBTC. (B) AFM surface roughness of CuBTC. (C) SEM image for uniformity of CuBTC.	63
Figure 4-13: Sample characterization sheet maintained for each device throughout its lifetime.	64
Figure 5-1: (A) Uncoated device (Optical). (B) HKUST-1 coated device (Optical). (C) HKUST-1 coated device (SEM).	65
Figure 5-2: (A) Mercury model of CuBTC 13.2 Å cage. (B) Mercury model of 11.1 Å cage. (C) Volume of the two cages the smaller pocket [31].	66
Figure 5-3: Wheatstone bridge schematic. $R_{S1}$ and $R_{S2}$ are microcantilevers while $R_1$ and $R_2$ are fixed resistors. $10\Omega$ resistor is used to measure current in the bridge and may be included or ignored for calculation.	67
Figure 5-4: Sample isotherm for water response for 40 cycles of CuBTC on SAM.	69
Figure 5-5: Raw data step response of 40 cycles CuBTC on SAM to water.	70
Figure 5-6: Mixed response of 40 cycles CuBTC on SAM to methanol vapor.	71
Figure 5-7: Sample time constant calculation using methanol response with CuBTC on SAM.	73
Figure 5-8: Sample time constant calculation using water response with CuBTC on SAM.	73

Figure 5-9: Sample time constant calculation using ethanol response with CuBTC on SAM.	74
Figure 5-10: Response of alcohols and water on 40 cycles of CuBTC on SAM.	75
Figure 5-11: Response of 40 cycles of CuBTC on SAM. (A) Response to varying concentrations of water. (B) Response to varying concentrations of methanol. Response of these analytes had a good degree of reversibility.	76
Figure 5-12: Response of 40 cycles of CuBTC on SAM. (A) Response to varying concentrations of isopropanol. (B) Response to varying concentrations of ethanol.	76
Figure 5-13: Response of 50 cycles CuBTC on SiO <sub>2</sub> for alcohols compared to water and acetone [25] isotherms from mixed response data in random order similar to Table 5-2.	77
Figure 5-14: Data for 40 cycles of CuBTC on SAM. (A) Acetone was characterized by slow adsorption and desorption curves. (B) Chloroform was characterized by rapid adsorption but slow desorption.	77
Figure 5-15: Data for 40 cycles of CuBTC on SAM. (A) Mechanical relaxation in the case of toluene did not saturate response over time. (B) Hexane saturated over time.	78
Figure 5-16: Some analytes exhibited unique adsorption features making time constant calculations difficult.	78
Figure 5-17: Decane response of CuBTC on SAM.	81
Figure 5-18: Toluene response in water background was demonstrated.	83
Figure 5-19: Water concentrations were detected in a toluene background.	83
Figure 5-20: Water response on CuBTC coated device over 12 months of testing.	85
Figure 5-21: (A) Response of HKUST-1 coated microcantilever with 40 cycles on SAM @ 22°C. (B) Response of HM1500 humidity sensor by Measurements Specialties Inc. Concentrations varied from 1735ppm – 5780ppm. Humidity detector readings ranged from 2100ppm - 6330ppm.	86
Figure 6-1: Ambient noise of four identical fixed resistors.	90

Figure 6-2: Wheatstone bridge with one old type cantilever connected in place of a fixed resistor.	91
Figure 6-3: Wheatstone bridge with one new type cantilever connected in place of a fixed resistor.	91
Figure 6-4: New cantilever setup with active heating set to 25°C was more stable than old cantilever setup with set point of 30°C due to increased thermal mass.	92
Figure 6-5: Heating of cantilever device by halogen lamp exposure.	93
Figure 6-6: Wheatstone bridge as it is laid out on the microcantilevers. Conductor E can be used as a temperature sensor or heating element.	94
Figure 6-7: Response of new type device (210) with 60 cycles of CuBTC vs response of old type device with 40 CuBTC on SAM (24).	96
Figure 6-8: Step response of wide microcantilever of new type to water. 60 cycles CuBTC on SiO <sub>2</sub> .	96
Figure 6-9: 60 cycles of CuBTC on SiO <sub>2</sub> . MOF appears to have grown less uniformly than on old type cantilevers.	97

## NOMONCLATURE

AMI	Acetone Methanol Isopropanol
DAQ	Data Acquisition
DRIE	Deep Reactive Ion Etching
GPS	Global Positioning System
ICP	Inductively Coupled Plasma
LCC	Leadless Chip Carrier
LCD	Largest Cavity Diameter
LIA	Lock-in Amplifier
LOD	Limit of Detection
MEMS	Micro-Electro Mechanical Systems
MFC	Mass Flow Controller
MOF	Metal Organic Compounds
PCB	Printed Circuit Board
PECVD	Plasma Enhanced Chemical Vapor Deposition
PLCC	Plastic Leaded Chip Carrier
PLD	Pore Limiting Diameter
PPB	Parts Per Billion
PPM	Parts Per Million
RIE	Reactive Ion Etching
SAM	Self-Assembled Monolayers
SCCM	Standard Cubic Centimeters
SCS	Single Crystal Silicon
SOI	Silicon-on-Insulator

VI

Virtual Instrument

VOC

Volatile Organic Compounds

## SUMMARY

Metal Organic Frameworks (MOFs) are a new class of nanoporous materials with high surface area, thermal/chemical stability and a taylorable pore size. These properties make MOFs ideal for storage and gas separation applications. Piezoresistive microcantilever sensors are microfabricated devices that are highly sensitive to surface strain due to doped single crystal silicon regions. Changes in resistance generated by surface strain can be measured with a high degree of accuracy using a Wheatstone bridge and basic instrumentation. This thesis will discuss the use of piezoresistive microcantilever sensors as a transduction mechanism for detection of volatile organic compounds (VOC's) using MOF coatings. It will be shown that by coating a microcantilever with MOFs it is possible to detect low levels of different VOC's (hundreds of parts per million). Excellent sensitivity and a simple transduction mechanism make these devices low power and highly compact. Such devices would be capable of detecting a plethora of different analytes at low concentrations. Devices were engineered for maximum response and microfabricated in the cleanroom with high yield. A custom setup for testing the devices was designed and machined. A number of MOFs were selected and tested, their response was recorded and analyzed. Twelve different analytes including eleven VOC's and water were used to characterize the MOFs. Microcantilever sensors were shown to be durable, reliable and stable in long term testing despite being subjected to many different analytes. MOF coatings proved flexible, durable, stable and reversible. This work will show a promising new technology for a next generation gas sensor.

# **CHAPTER 1**

## **INTRODUCTION**

### **1.1 Motivation**

The search for a versatile detection device to fulfill many emerging applications for gas sensing in the environment has led to increased interest in next generation sensing techniques. Water and air quality monitoring, food safety, medicine and defense all require novel gas sensing techniques and would benefit from a device that combines a wide set of desirable characteristics such as low power requirements, selectivity, sensitivity, stability and easy calibration at an affordable cost. Micro-Electro Mechanical Systems (MEMS) show promise in providing a solution which combines many of the following desirable traits in a single device:

1. Detection of multiple analytes
2. Detection in complex mixtures
3. Detection in various media
4. Extremely selective
5. Highly sensitive
6. Ultra-low power
7. Highly portable
8. Robust
9. Low cost
10. Easy to calibrate
11. Stable
12. Reversible

There are many technologies that have been developed for sensing. In several cases current solutions perform specific detection tasks very effectively, for example Impulse XT Disposable Single Gas Detector by Honeywell is used in heavy industries to detect dangerous levels of a designated single gas in the work environment. These systems are highly portable, however, they lack versatility to detect in complex mixtures and for other applications in other environments. On the other hand, systems capable of complex mixture analysis, such as mass spectrometry, are hardly portable, low cost or low power.

Sensors are devices used to alert individuals of dangerous situations such as presence of carbon monoxide, an asphyxiant, in an enclosed space or a combustible level of methanol in a mine. Sensors typically consist of a transduction mechanism, which can quantify presence of analyte by interpreting a physical phenomenon and transmitting it to a form understood by the individual. The selective layer in a sensor is used to determine which analytes will trigger the physical response tracked by the transduction mechanism. In the case of piezoresistive microcantilevers, for example, the MOF coating determines the dangerous substance and expands. The physical expansion of the MOF causes the piezoresistive cantilever, or the transduction mechanism, to generate an electrical response which can be interpreted by an individual looking at the signal.

In broad terms, sensors capable of detecting harmful analytes around us may benefit health, quality of life and public safety. Modern portable computing devices have revolutionized every aspect of contemporary life with sensors such as gyroscopes, accelerometers, global positioning systems (GPS) and magnetometers. Pollution in big cities is a growing health concern, and air quality deterioration has been an increasingly vocal topic in the news. Introducing a MOF based portable sensor capable of accurately measuring concentrations of toxins in the surroundings would open new possibilities in the study of diseases (air quality effects on health), and have the potential to improve quality of life for millions of city dwellers. Such devices could be included in your

smartphone and further assist in detection of blood sugar levels in diabetic patients and enhanced roadway safety as portable breath analyzers.

## **1.2 Overview of Microcantilevers for Sensing Applications**

In broad terms, microcantilevers are suspended structures with at least one fixed boundary condition. Traditionally, microcantilevers are rectangular structures with length to width aspect ratio of 1:10 and thickness on same order of magnitude as the width. Such beams have been used in the construction industry for centuries to support balconies and floors. Recent drive to reduce the size of macro components for new applications in the micro and nano-scale has adapted microcantilevers for new uses. The definition of microcantilevers has also been expanded to include other shapes and aspect ratios. Commercially successful applications of microcantilevers include femtoliter array patterning of fluids on substrates (BioForce NanoEnabler) and imaging (Atomic Force Microscopy).

Cantilever sensing can be divided into two broad groups, sensing mass addition and sensing cantilever bending. The first category typically senses amount of mass adsorbed on to the surface of the microcantilever. Mass adsorption changes the fundamental frequency of the device which can be measured using various techniques described below. Cantilever bending on the other hand, generates strains in the cantilever layers causing physical changes in properties of layers that can be detected. More information regarding microcantilevers can be found at these references [1], [2].

### **1.2.1 Cantilevers in Sensing Applications**

Microcantilevers are ideally suited as transduction mechanisms for sensing applications. Physics behind their deformation is relatively simple and is well understood [2]. Suspended structures are robust and versatile allowing for different sensing schemes which are summarized in Table 1-1 below.

**Table 1-1: A table summarizing microcantilever deflection measurement techniques [1].**

Mechanism	Cost	Size	Sensitivity	Output
Optical Deflection	High	Large	Excellent	Frequency
Piezoresistive	Low	Small	Average	Voltage
Piezoelectric	Intermediate	Small	Average	Charge
Capacitive	Intermediate	Small	Excellent	Capacitance
Interferometry	High	Intermediate	Excellent	Current
Optical Diffraction	High	Large	Average	Current
Thermal	Low	Small	Average	Frequency

Optical deflection based techniques (interferometry, optical diffraction) are generally the most accurate with angstrom deflection resolutions [1]. Frequency based measurements are very accurate at predicting small mass changes on the surface of the cantilever, allowing for mass based adsorption quantification for these systems [2]. The draw backs for such detection schemes are in their cost and generally large size. To achieve such low resolutions, vibrations must be eliminated resulting in reduced portability. Lasers and photo diodes are necessary, so power requirements for such systems are generally higher. Size and power requirements makes optical techniques unlikely candidates for ultra-low power applications.

Capacitive techniques have excellent sensitivity and resolution, in addition, instrumentation may be combined on a single PCB with the sensor [1]. These techniques are hindered by the increased cost and complexity of the fabrication process, due to the need to create parallel plates in high proximity.

Piezoelectric effect does not generally require external power sources for bending measurement. Benefits of piezoelectric based devices is their ability to work both as sensors and actuators, since the piezoelectric effect is reversible. Since silicon is does not exhibit piezoelectric properties, exotic materials are required.

Thermal sensing techniques use piezoelectric elements at the base of the microcantilever to heat the device and induce thermal bending [3]. By modulating the input signal at the fundamental frequency of the cantilever, it is possible to detect small

changes in mass uptake. This technique tracks the changing frequency and unlike optical setups, does not require external equipment to detect the shift. In order to improve the resolution of these devices, it is necessary to fabricate complex geometry resonators. The main drawback of these devices is the increased power necessary to constantly excite the device during measurement.

Piezoresistive microcantilevers typically use similar piezoresistive elements to measure surface strain caused by analytes on the surface of the cantilever. A simple Wheatstone bridge is used to read the changes in resistance induced by the surface strain. These devices do not require complex external equipment or special shapes. Their simplicity makes them low cost, highly portable and most importantly very low power [4].

### 1.3 Metal Organic Frameworks

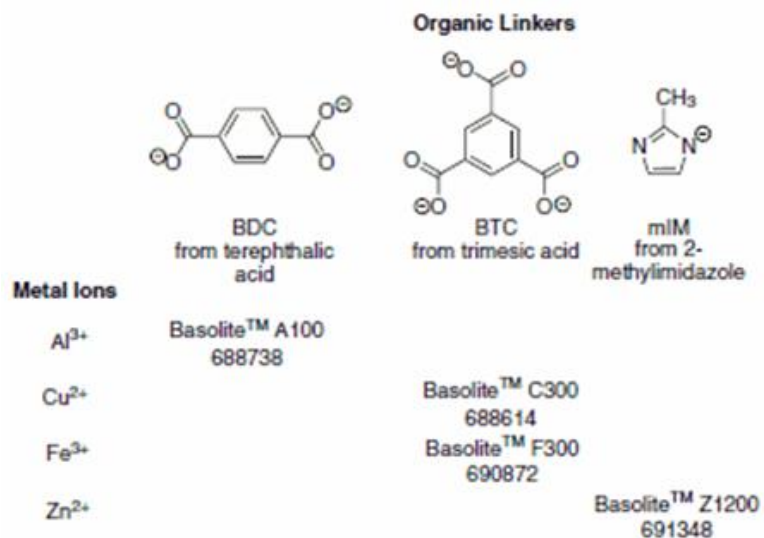


Figure 1-1: Examples of a few metal ions and organic linkers that can be used for MOF synthesis [5].

Metal organic frameworks (MOF's) is a new class of nanoporous materials with applications in catalysis, sensing, storage and separation applications [6], [7]. MOF is a class of advanced nanomaterials with highly ordered structure, nanoporous openings, growth techniques implementing layer-by-layer deposition, possibility for controlled

single crystal growth, seeding with self-assembled monolayers (SAM) and promising applications on the nano and mesoscales. As the name suggests, MOFs form when metal centers are bridged together with organic connectors (Figure 1-1). The metal centers are single ions or clusters of ions of opposite charge than the organic connectors (also referred to as linkers or ligands). These ions and linkers when brought together organize themselves into a highly regular structure, or a framework. This forms a highly porous cage that allows size selective separation of analyte molecules. Molecules can enter and exit these structures through “windows” (3-30Å), or empty spaces of taylorable size, making these materials versatile in their application as a molecular sieve [8]. High porosity and high surface area make the materials ideal for capturing and storage of gases, while their thermal stability allows for a number of desorption methods making them reusable [8]. Researchers demonstrated purification, dehumidification and capture of gases such as H<sub>2</sub>, H<sub>2</sub>O and CO<sub>2</sub> using MOFs; these methods are known as separation by adsorption [8]. MOFs are also suitable as sensing coatings for various micro-electro mechanical systems (MEMS). In rigid MOFs, uptake is controlled primarily by adsorbate-pore surface interaction and steric interaction, however, some MOFs exhibit a degree of structural flexibility not observed in traditional recognition layers [8]. This unique property allows the use of this material as a sensitive layer on mechanical devices.

### 1.3.1 Operational Principles of Metal Organic Frameworks

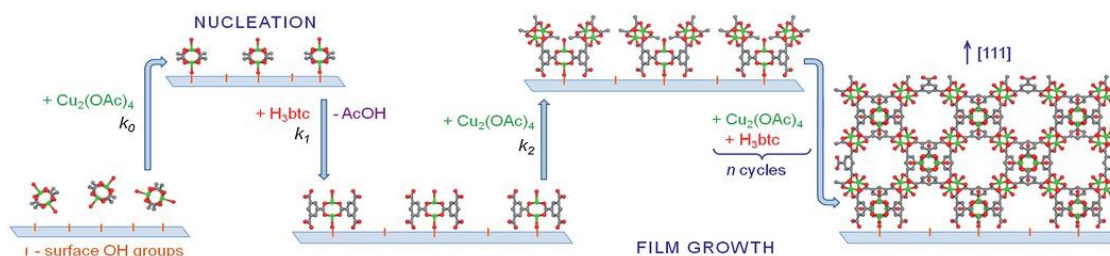


Figure 1-2: Layer by layer growth of HKUST-1 on OH functionalized SAM [11].

### 1.3.1.1 Synthesis of Metal Organic Frameworks

Although there are many different synthesis techniques for MOFs, such as solvothermal, hydrothermal, and metal plate in organic ligand complex to name a few, thin films on surfaces is of primary interest for nanotechnology. Solvothermal and hydrothermal methods use autoclaves with inert coatings to supersaturate solutions to the point of nucleation and crystal growth at high temperatures and pressures. Metal plate in organic ligand complex method uses a metal coated surface, which is subsequently dipped in the ligand solution to begin the MOF growth process.

Thin film MOFs are synthesized using layer-by-layer techniques [9], [10]. A MOF seed crystal layer on the substrate (such as gold or silicon dioxide) provides nucleation sites for subsequent growth [8]. Growth occurs by submerging the substrate in metallic ion solution, followed by a submersion in organic precursor solution. A molecular layer of MOF forms following the removal from organic solution [11]. Repeating this process allows for deposition of thicker layers on the surface. As previously discussed, the crystalline film forms due to ionic nature of linker and oppositely charged metal solutions. An alternative method to grow films (Figure 1-2) requires self-assembled monolayers (SAM) to be deposited on the surface of the substrate prior to cyclic deposition (functionalization of substrate). Selection of SAM for each MOF ensures good adhesion of the film to the surface and better control of growth patterns, however, SAM's provide an extra step in film formation and have shown inferior thermal stability and growth rates to MOFs grown directly on the surface [12]. Reactors that cycle the fluids automatically have been demonstrated as well by the Wöll group [10].

Solution submersion based methods cause growth over the whole area of the sample; however, in certain applications it may be of interest to control locations of growth. MOF growth was demonstrated using the BioForce Nanoenabler [13]. The Nanoenabler is capable of dispensing femtoliter sized droplets onto targeted areas of the

substrate. The fluid is dispensed onto the surface using a microfluidic channel etched into a cantilever and manipulated by an XYZ stage. Upon evaporation of the solvents, a MOF film is formed. Such novel deposition techniques can be used to deposit different MOFs on the same substrates in different patterns and can provide interesting applications of MOFs to micro devices.

#### 1.3.1.2 Working Principles of Metal Organic Frameworks for Gas Separation

Recent interest in MOFs stems from their potential replacement of zeolites in industry separation applications [8]. Separation process captures certain gases while letting all other gases pass through. Releasing the trapped gas results in a high purity substance. This method can also be used to capture greenhouse gases such as CO<sub>2</sub> at the source, and reuse the gas in other industrial applications [8]. Gas separation is a complicated process with unique interactions for each chemical and MOF, however, some common phenomena will be discussed.

The most basic separation technique is based on size or shape of the guest molecule and is known as molecular sieving [8]. If the guest molecule is larger than the largest opening in the MOF, it will not be able to enter the lattice. Therefore, a mixture of larger and smaller molecules can be separated by selecting a MOF with opening larger than the small molecule, yet smaller than the large molecule.

If the gas mixture molecules are of similar size, their interaction with the surface may result in one of the molecules being adsorbed while the other molecule not based on thermodynamic equilibrium giving preference to one over the other [8]. For example, a polar molecule such as water may be drawn to certain MOFs more strongly due to weak charges in the MOF lattice, whereas a molecule of similar size with no polarity effects would not be adsorbed as strongly. Van der Waals forces and hydrogen bonds may also play a role in adsorption preference [8].

Yet another method of separating two similarly sized molecules is based on different diffusion rates of the two gas molecules and is termed kinetic separation [8]. If one molecule diffuses through the MOF faster than the other molecule, the two gases will separate.

The last mechanism which is unique to flexible frameworks is pressure and temperature control of pore size. Pore size in flexible frameworks changes with pressure and temperature, thus it is possible to separate different sized molecules by changing both pressure and temperature [8]. One can imagine if there are three substantially different molecules to separate, one can start with the smaller pore size at a given temperature, and gradually increase the size of the MOF framework by increasing the temperature of the MOF, thus separating the three gases with a single MOF. Higher pressures in turn, increase the likelihood that adsorption will occur while lower pressure may aid in diffusion of the analyte out of the framework for desorption step.

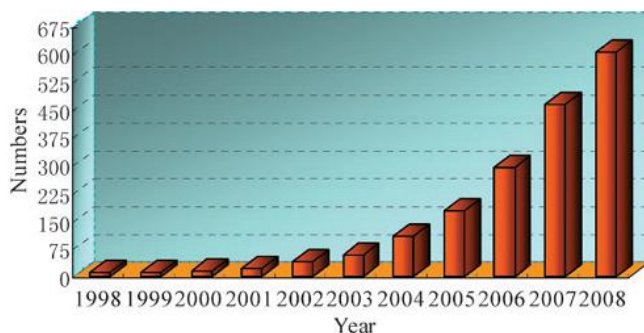


**Figure 1-3: Number of publications on MOFs [7].**

Although there are other mechanisms involved in adsorption of MOFs, and often mechanisms listed above occur simultaneously, the above phenomena are the most common explanations in literature to separation behavior using MOFs and other porous separation media.

### **1.3.2 Summary of Key Features of MOFs**

It is important to note that the flexible framework allows for applications unique to MOFs, such as temperature based separation and strain based applications in MEMS for sensing of analytes. In addition, MOF frameworks have a lesser impact on the environment as they are often reversible allowing for time durable devices [8]. Other layers such as polymers may undergo a permanent change of the surface chemistry. The wide variety of available linkers and metal ions allow for precise control of the framework openings, and in conjunction with temperature and pressure regulation can provide excellent control of pore size of MOFs [12]. Polymers on the other hand exhibit inferior selectivity, since they react with many analytes and provide no steric control. As such, MOFs are thought to be the next step in separation technology and have a strong potential in sensing applications resulting in increased interest over the last decade (Figure 1-3).

### **1.4 Metal Organic Frameworks for Piezoresistive Sensors**

As was previously mentioned, a unique property of MOFs is their ability to expand upon introduction of analytes causing surface strain on cantilever devices [14]. Not all MOFs exhibit the ability to expand upon adsorption, thus selecting appropriate films for strain sensing requires careful consideration of pore size, solvent stability, temperature stability, crystal structure and internal volume/surface area. Selection of pore size in most cases determines maximum kinetic diameter of guest molecules and dictates sieving effects of the film. Solvent stability and temperature stability are required for reliable device operation in different environments and for a wide range of analytes. Crystal structure and internal volume in turn, affect the expansion properties of the MOF as well as adsorbate-adsorbant interactions.

Allendorf group at Sandia national laboratories investigated and preselected groups of MOFs that show promise for strain based gas sensing (Table 1-2). Growth

protocols were developed and films were characterized [9].  $V_{\text{free}}$  is a measure of the porosity of the MOF, defining the percent of empty volume within the film. Pore limiting diameter (PLD) is a measure of the largest opening through which analytes can enter the MOF structures. Largest cavity diameter (LCD) determines the diameter of the largest opening within the structures. These MOFs exhibit excellent thermal and solvent stability and have high degrees of porosity [15]. In addition, the diversity of PLD's and LCD's show promise in using these MOFs to control analyte adsorption via steric interactions.

**Table 1-2: Summary of MOFs identified as potential selective layers for piezoresistive microcantilever sensors.**

MOF	$V_{\text{free}}$ (%)	PLD (Å)	LCD (Å)
CuBTC	69.8	6.5	11.1
NOTT-100	66.6	4.8	10.0
NOTT-101	72.8	5.5	11.2
PCN-14	64.2	4.5	11.2
ZIF-7	51.9	3.0	4.5
ZIF-8	58.5	3.4	10.8

By using different MOFs coated on an array of cantilevers, a sensor leveraging on steric interactions and sieving effects can be constructed. MOFs as selective layers for detection of VOC's is well documented [14], [16]. In order to identify constructive combinations of MOFs on such arrays, it is necessary to characterize the growth parameters, resulting films as well as response of such MOFs to analytes on piezoresistive microcantilevers. The team has successfully coated NOTT-100, NOTT-101, ZIF-8 and CuBTC on old design cantilevers and tests were performed with some of the analytes on all four types of films, however, only CuBTC has been completely characterized with all analytes. This thesis will only discuss the results for CuBTC, while

discussion of other MOFs will be left for future works pending further characterization of response properties.

### **1.5 Concluding Remarks**

The following chapters will discuss fabrication of MOF coated microcantilever sensors. By leveraging low cost and versatility of microcantilevers, as well as flexibility and selectivity of MOFs, this work has made an important step toward combining many aspects of the list in section 1.1. New research into larger pore sized MOFs with open new possibilities in particulate sensing [17].

## CHAPTER 2

### EXPERIMENTAL SETUP FOR MEASUREMENT OF CANTILEVER SENSORS RESPONSE TO GASES AND GAS MIXTURES

#### 2.1 Introduction

Experimental setup system was designed to expose coated piezoresistive microcantilever sensor to different concentrations of analytes. The system was composed of a number of mass flow controllers, a hydrator and a test cell. Analytes were carried into the test cell by ultra-high purity nitrogen gas. Initial experimental setup was adapted by Dr. Lee and designed by Dr. Choudhury [18], [14]. It was then further modified to improve data acquisition characteristics and redesigned to work with new generation of cantilevers. Following sections will discuss details regarding different configurations used in exposure experiments.

#### 2.2 Original Experimental Flow Setup and Measurement Approach

For accurate results it is necessary to control as many environmental variables as possible. Such variables include temperature, vibration, humidity and electromagnetic interference. To satisfy these basic requirements all equipment was setup inside a fume hood, and the device was enclosed in a chamber (Figure 2-1.B). Coaxial shielded BNC connectors were used to reduce noise in measurements. Nitrogen flow was used to control the environment immediately surrounding the device.

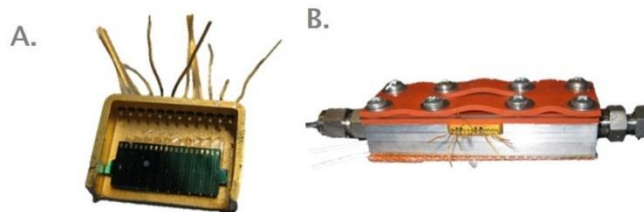


**Figure 2-1: (A) Wirebonded device inside its package. (B) Package inside the test cell.**

Original LabView program only recorded the changes in voltage measured across the bridge. Only one device at a time was measured with no multiplexing capabilities. In addition, the temperature of the setup was not measured. Mass flow controllers were adjusted by hand and temperature was recorded by hand.

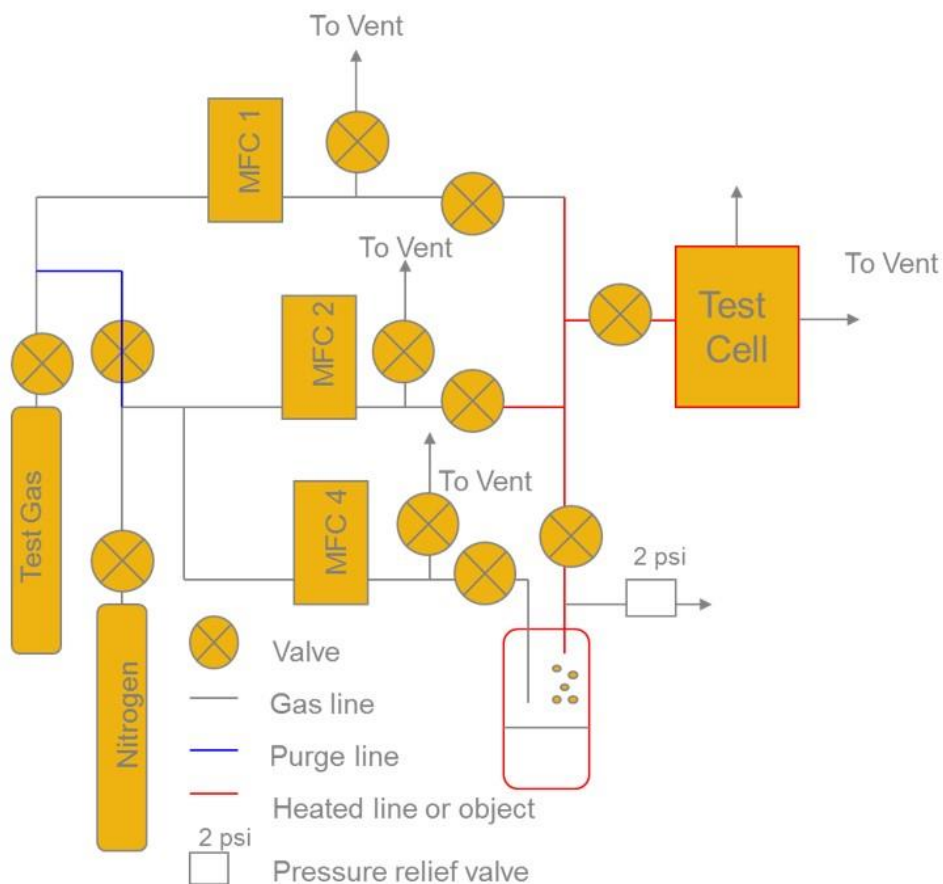


**Figure 2-2: Schematic of gas delivery system via mass flow controllers and hydrator to the test cell.**

To achieve a wide range of concentrations nitrogen gas was pumped at 20 PSI through a set of mass flow controllers (Figure 2-2). Ultra-high purity nitrogen was used as the carrier gas due to its low adsorption in MOFs of interest and its low concentrations of water. Due to hydrophilic nature of many MOFs it was necessary to use exclusively ultra-high purity nitrogen. MFC 1 and MFC 2 delivered purge nitrogen to the flow cell, while MFC 4 passed the nitrogen gas through a hydrator containing the analyte of

interest. By mixing the purge lines with the hydrator lines at different flow rates, concentration control was achieved. In addition, to test CO<sub>2</sub>, MFC2 could be disconnected from the nitrogen tank and instead connected to a CO<sub>2</sub> tank for measurements of that analyte. All three MFCs were rated 100 sccm at 100%.

### 2.2.1 Packaging of Sensor Arrays

The selected package (Figure 2-1.A) had a twelve pin connection allowing up to six devices to be connected at once. Each microchip consisted of an array of ten microcantilever sensors with a single piezoresistor on each (Figure 3-2.A). As a result only 60% of the devices on each microchip could be wirebonded at any given time. Once wirebonded the package was inserted into a custom machined aluminum test cell. Each test cell (Figure 2-1.B) could accommodate two packages for a total of 12 wirebonded microcantilevers at one time. The two ports also allowed exposure of two different coatings to the same concentrations simultaneously.

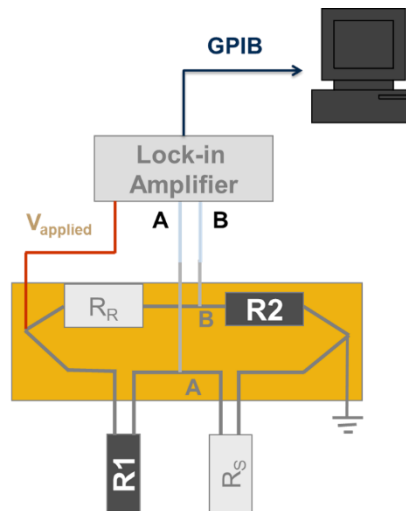


Figure 2-3: Wheatstone bridge additive configuration.

### 2.2.2 Instrumentation

Wheatstone bridge requires simple instrumentation and provides accurate measurement of small changes in resistance. Two piezoresistive microcantilevers were connected to the same Wheatstone bridge to achieve maximum response (Figure 2-3).

Initial balancing of the bridge was achieved using two stationary resistors. The sensing cantilever ( $R_s$ ) was connected on the opposite leg of the reference cantilever ( $R_r$ ) thus doubling the total response by adding response from each individual device. Devices responded strongly to temperature (see section 4.1). To measure the device response, a lock-in amplifier (LIA) from Signal Recovery (SR-7265) was connected to nodes A and B (Figure 2-3). Changes in voltage were recorded using a simple LabView Virtual Instrument (VI) by connecting the LIA via a GPIB cable to a dedicated computer. LIA was used to reduce the noise level of the measurement, thereby increasing the sensitivity of the device and hence the limit of detection (LOD). Different frequencies and time constants for the LIA were investigated to ensure signal acquisition does not heat device, filters noise and collects data quickly. Experiments were conducted at 200mV, 3000Hz with a time constant of 10ms. Range was selected to avoid overload and was based on baseline voltage after bridge was balanced. Values varied from 500 $\mu$ V to 10mV.

Changes in voltage signify changes in resistance caused by surface strain on the surface of the cantilevers. Stationary resistors  $R_1$  and  $R_2$  did not change values throughout the experiment, however, values of both  $R_s$  and  $R_r$  changed over time allowing response to different analytes to be quantified based on percent rate change ( $\Delta R/R$ ). See section 5.1.2 for calculation details.

## **2.3 Experimental Setup Modifications**

### **2.3.1 Disadvantages of Old Experimental Setup**

#### **2.3.1.1 Temperature Control**

Precise control of the environment is vital for collection of high quality data from cantilever sensors. To address temperature control concerns with the old flow setup, the combination of tube, hydrator and test cell heating were implemented so that the temperatures would be the same during an experiment. Controlling the temperature of

the old design test cell proved difficult due to the low thermal mass of the aluminum flow cell. Despite tuning the proportional controller settings for optimal operation, an oscillation of  $0.1^{\circ}\text{C}$  was still observed at  $25^{\circ}\text{C}$ . N-doped piezoresistive elements are sensitive to temperature with a measured coefficient of  $8\Omega/^{\circ}\text{C}$  which corresponds to  $.8\ \Omega$  change in resistance. These changes in resistance are significant and were easily measured with the Wheatstone bridge (Figure 2-4).

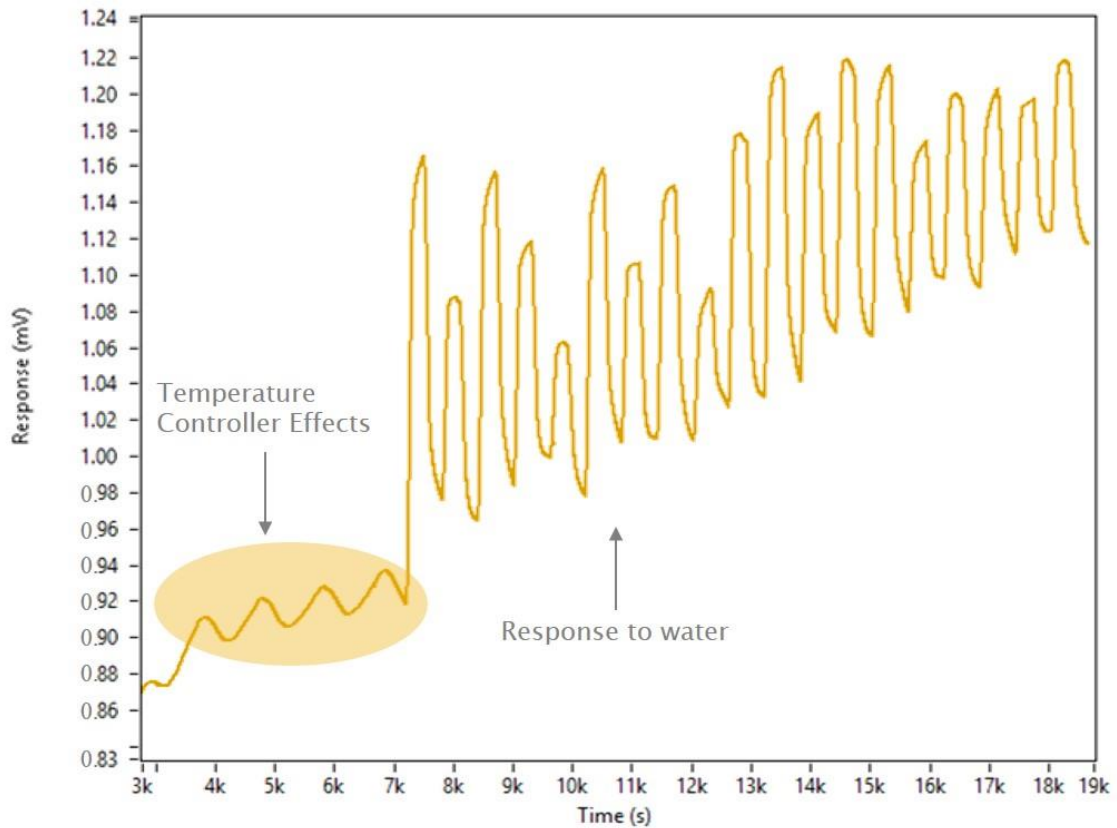


**Figure 2-4: This plot illustrates temperature oscillation when active temperature control was implemented.**

Temperature also plays an important role in the vapor pressure calculations, and therefore the concentration supplied to the test cell. A Lauda-Brinkman water bath (Figure 2-5) was setup and a hydrator was placed inside. The temperature could be set to a range of  $-15^{\circ}\text{C}$  (ethylene glycol required at low temperatures) to  $100^{\circ}\text{C}$  (water was used at other temperatures due to superior temperature control) allowing for a large range of vapor pressures. For hydrator temperatures higher than ambient, condensation would

form unless the tubing leading up to the test cell would be temperature controlled. Heating tape (HTS/Amptek AWH-102-060) was wrapped around the tubing leading from the hydrator to the flow cell, and set to temperatures 5°C higher than the hydrator to avoid condensation in the tubing. Power setting for the tape was selected by measuring the temperature of the tubing at three points along the heated section using a thermocouple. Heat settings were adjusted until desired temperature was achieved. Although an adjustable proportional-integral-derivative (PID) controller (OptiCHEM CG-15001) was used to control the temperature of the flow cell, temperature of the hydrator was controlled by a fixed PID in the Lauda-Brinkman bath. Heating tape temperature was controlled using a fixed setting on the OptiCHEM CG-15009-01 controller, therefore, temperatures achieved depended on the ambient temperatures and the selected power setting.

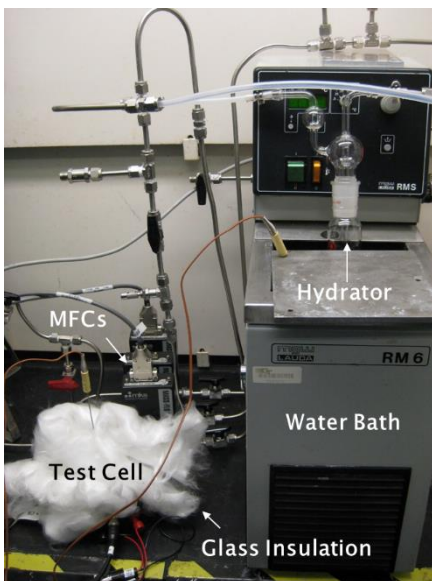


**Figure 2-5: Temperature controlled setup for old design microcantilevers.**

Due to three separate temperature control systems, difficulties arose during data acquisition. Cantilever resistance fluctuations due to flow cell temperature coupled with variations of vapor pressure in the hydrator due to a +/- 0.2°C shift in the bath temperature (nonadjustable) adversely affected collected data. Eventually, temperature

control of the system was scrapped and all experiments were conducted at ambient room temperature ranging from 16°C in the summer (air conditioning) to 26.7°C in the winter (due to heating). Lack of vapor pressure control adversely affected concentration control, since low concentrations could only be achieved using very high dilution ratios (see calculations in section 5.2.2).

#### 2.3.1.2 Analyte Quality, Cost and Waste Management

Due to HKUST-1's hydrophilic properties [19], it was essential to ensure the MOF was completely dehydrated prior to testing. Some analytes, however, have inherent hydrophilic properties and at room conditions will absorb humidity from the environment. Once analyte has been exposed to room conditions, it may be faulty to assume that any recorded response is solely due to the analyte. Response curves in such cases will include a combined effect of the water vapor and analyte mixture.

As such, the 100mL hydrator used in the experiments had a number of disadvantages in regard to analyte purity. Due to glass-glass interface, sealing the two part hydrator proved difficult and required a slight downward force from the attached tubing to maintain seal. During experiments, pressure buildup would sometimes cause the top part to come off during the experiment contaminating the analyte. Finally, the physical size of the hydrator was prohibitive for humidity free solutions such as glove boxes.

Anhydrous analytes are expensive and are generally provided in specialty containers to discourage diffusion of water vapor. Typically these containers are a few hundred mL and cost in excess of \$100 per bottle. Hence, running experiments with anhydrous solvents was eliminated due to prohibitive costs, since a whole bottle of analyte could only be used once to fill the large volume hydrator. In addition, difficulty in acquiring a humidity free environment for filling the hydrator increased the likelihood of contamination.

To reduce the likelihood of faulty data, solvents were disposed of at the end of each experiment and fresh solvent was used for each experiment. To decontaminate the 100mL bubbler an acetone, methanol and isopropanol (AMI) wash was performed. Large amounts of solvent waste were generated by each experiment, and a large quantity of analytes and cleaning solvents was consumed.

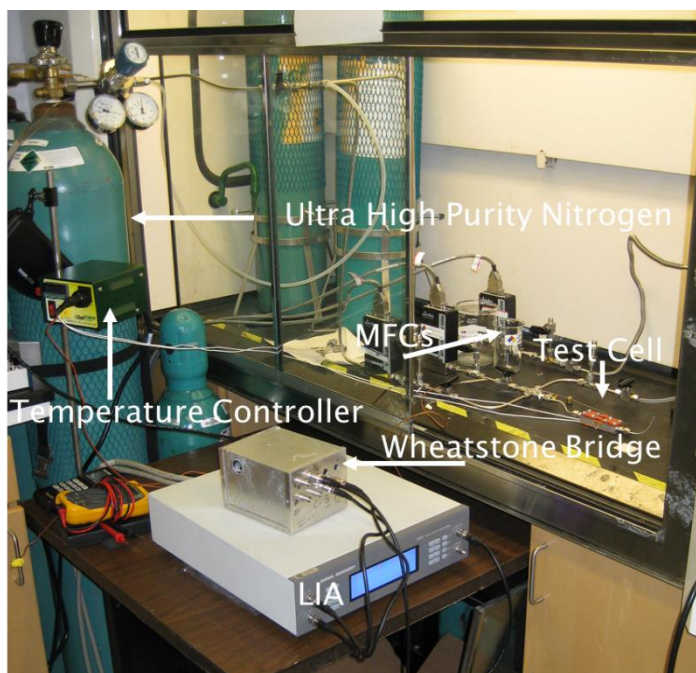


**Figure 2-6: Old experimental setup.**

### 2.3.1.3 Flow System

Dehydration of the MOF is essential to ensure only analyte response is recorded, therefore, it was important for the test cell to provide a humidity free environment. This was accomplished by purging the cell with 100 to 200 standard cubic centimeters (SCCM) of dry nitrogen. As previously mentioned, due to inability to control the temperature of the analyte, high mixing ratios were required to generate low concentrations of analyte, as described in section 5.2.2. Further, the large volume of the hydrator and the ¼” diameter tubing made the use of low flow rate MFCs difficult. In turn, large quantities of ultra-high purity nitrogen were required to run experiments. A

single nitrogen tank would only last through 10 to 15 experiments before a replacement tank was required.

#### 2.3.1.4 Instrumentation

Despite the simplicity of a Wheatstone bridge, the physical device initially suffered from a number of issues. Due to the prerequisite of two external resistors, a physical box housing the bridge was constructed (Figure 2-6). Connections were made using BNC cables. New cables were purchased due to noise issues with older cables. Test cell connections to the package were made using alligator clips. The combination of physical connections at the test cell and ports for the stationary resistors introduced locations of poor contact. On a number of occasions experiments were scrapped due to one of the connections failing midway through.

### **2.4 New Experimental Setup Design**

#### 2.4.1.1 Data Acquisition System Improvements

A new LabView program was designed with a user friendly interface (Figure 2-7). MKS PB4000 MFC controller was interfaced with LabView to control and record flow rates through the mass flow controllers. Signal Recovery (SR 3830) multiplexer was acquired to collect data from two bridges at the same time. A National Instruments Data Acquisition Card and a BNC-2120 connector were acquired to collect temperature, voltage and current in the two Wheatstone bridges. In addition to MFC control, the data acquisition (DAQ) system is capable of controlling voltages supplied to the bridge, LIA settings such as sensitivity, phase shift and range. Acquisition of another multiplexer can boost the number of simultaneous measurements to five complete bridges using the current DAQ.

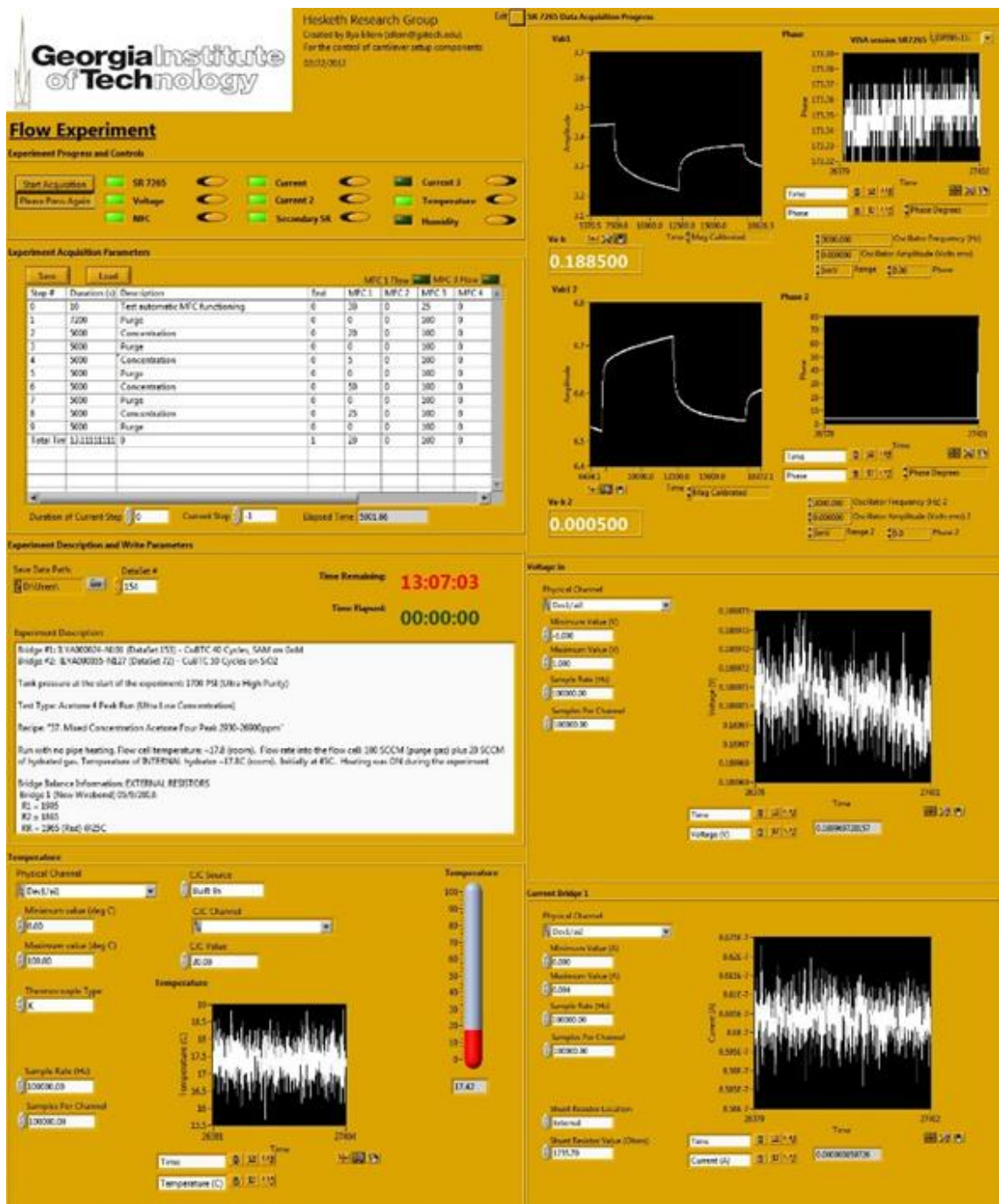


Figure 2-7: Interface of the LabView data acquisition system. Data for two bridges is collected simultaneously. Temperature of the flow cell, as well as gas flow rates, current and incoming voltage are all recorded.

### 2.4.1.2 Test Cell Redesign

To improve temperature control, reduce signal noise and analyte costs a complete redesign of the flow system was undertaken. Requirements (Table 2-1) were identified to aid in decision making. Pahl and Beitz systematic design process was applied to achieve requirements [20].

#### 2.4.1.2.1 Electrical Connections

Reduction of signal noise was achieved by selecting a 25 Pin D-Sub socket. The D-Sub socket was soldered to a plastic leaded chip carrier (PLCC) socket for ceramic package (Figure 2-8). A Leadless chip carrier (LCC) ceramic package (Figure 2-10) was chosen with 20 contacts to correspond to a five microcantilever bridges on the new device wafer.

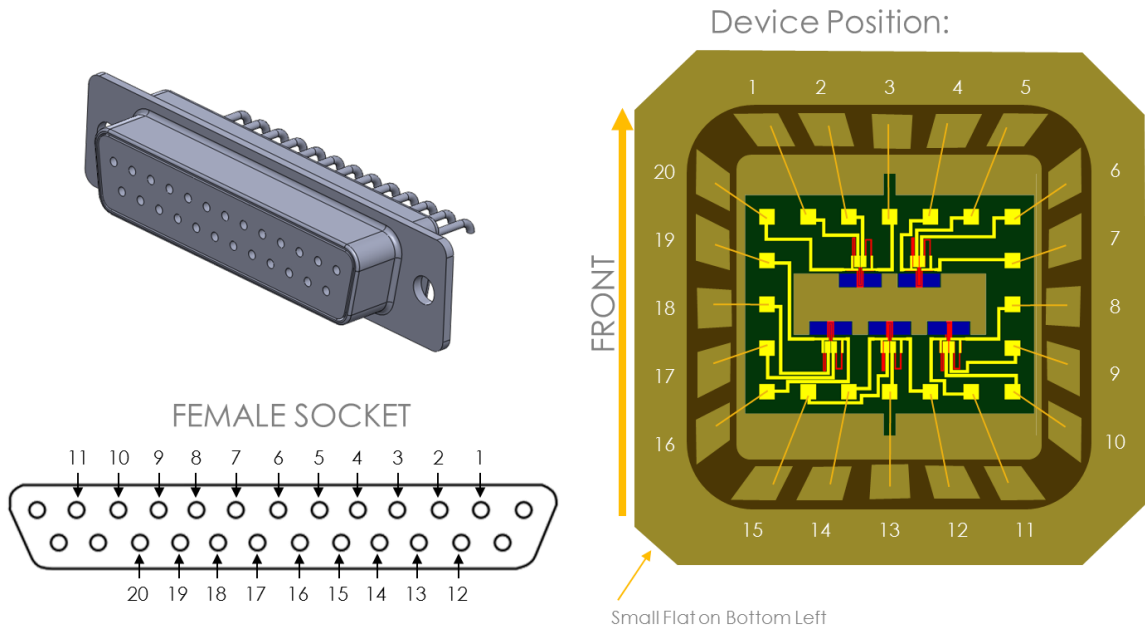


**Figure 2-8: Top left - 25 pin D-Sub socket. Bottom left - pins connected to cantilevers. Right - a devices wirebonded to the 20 pin LCC package.**

Benefits of this configuration included:

1. Better electrical contact with no loose connections
2. Simplified device loading/unloading procedures
3. Single shielded cable for signal delivery to DAQ
4. Cost savings (new package \$5 vs. \$50 for old package)
5. Wirebonding of device to new package is quicker due to improved angle of attack for wirebonding tool.
6. Improved device protection from physical damage due to enclosed nature of the new LCC package.

A direct linked 25 Pin D-Sub cord was purchased to connect the flow cell to the external distribution box (Figure 2-9). The distribution box was prewired to output voltages at nodes A and B of the Wheatstone bridge for each of the five bridges on the die. In addition it output the current in each of the bridges and provided connecting ports for voltage being supplied to the devices. Finally, an output port measured the voltage coming into the circuit. Short, high quality BNC cords were used to connect the distribution box to the multiplexer, LIA and BNC-2120 DAQ.

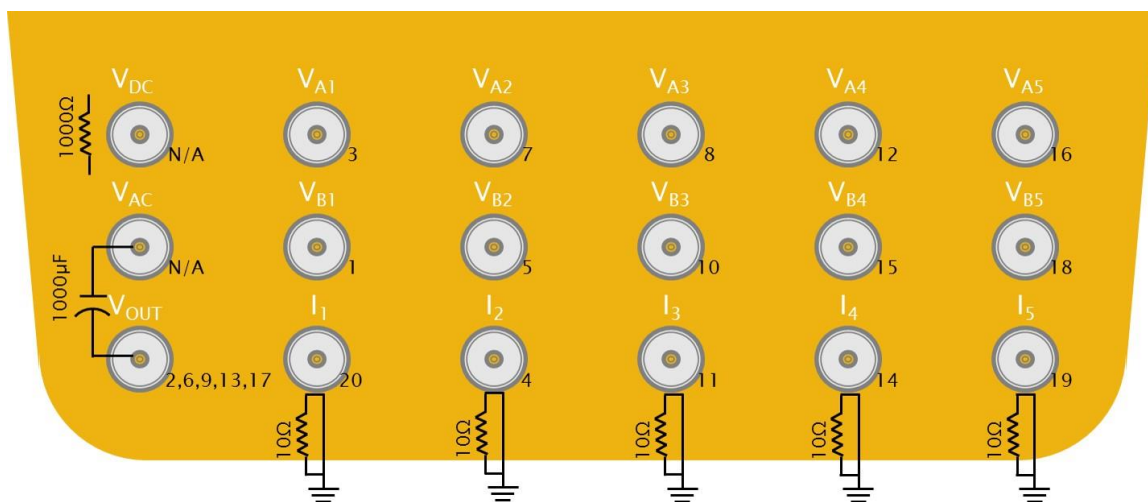


**Figure 2-9: Diagram showing distribution box for reading signals and powering the Wheatstone bridges on the new devices. All communications between the devices and this box were sent through a single six foot long D-Sub 25 pin cord.**

**Table 2-1: Requirements list.**

Updated:		Flow Cell		
5/13/2013				
<p>Redesign a flow cell which will integrate with current tubing and the new package design (LCC). Further, simplification of connections to instrumentation (lock-in amplifier and temperature probes) and integration with the laser setup should be considered.</p>				
	#	Changes	D / W	Requirements
Integration	1		W	Must interface with current supply pipe.
	2		W	Flow cell should have a window to allow laser beam through.
	3		D	Flow cell should allow for single time connection of all wires to the package.
	4		D	Flow cell should provide easy, single time connection to instrumentation.
	5		W	Flow cell should be compact enough to fit underneath the laser setup.
	6		D	Flowcell should include temperature measurement inside the cell (2 points).
Gas Flow Compatibility	7		D	All materials must withstand Ni, CO <sub>2</sub> , Ethanol, Methanol, Chloroform, CF <sub>4</sub> , Methane.
	8		W	Materials must not degrade under temperatures below 500C.
	9		W	Materials must not give off gases at temperatures below 500C.
	10		D	Flow cell must be airtight.
Physical Characteristics	11		W	Flowcell must withstand 500C temperature.
	12		D	Must withstand partial vacuum and 40 psi.
Cost	13		D	Flow cell should cost less than: \$300.

#### 2.4.1.2.2 Test Cell Physical Design

For improved temperature control of the hydrators and device, a single container was designed to house both (Figure 2-10). Four layer construction was implemented to achieve a thermally stable, self-contained test cell.

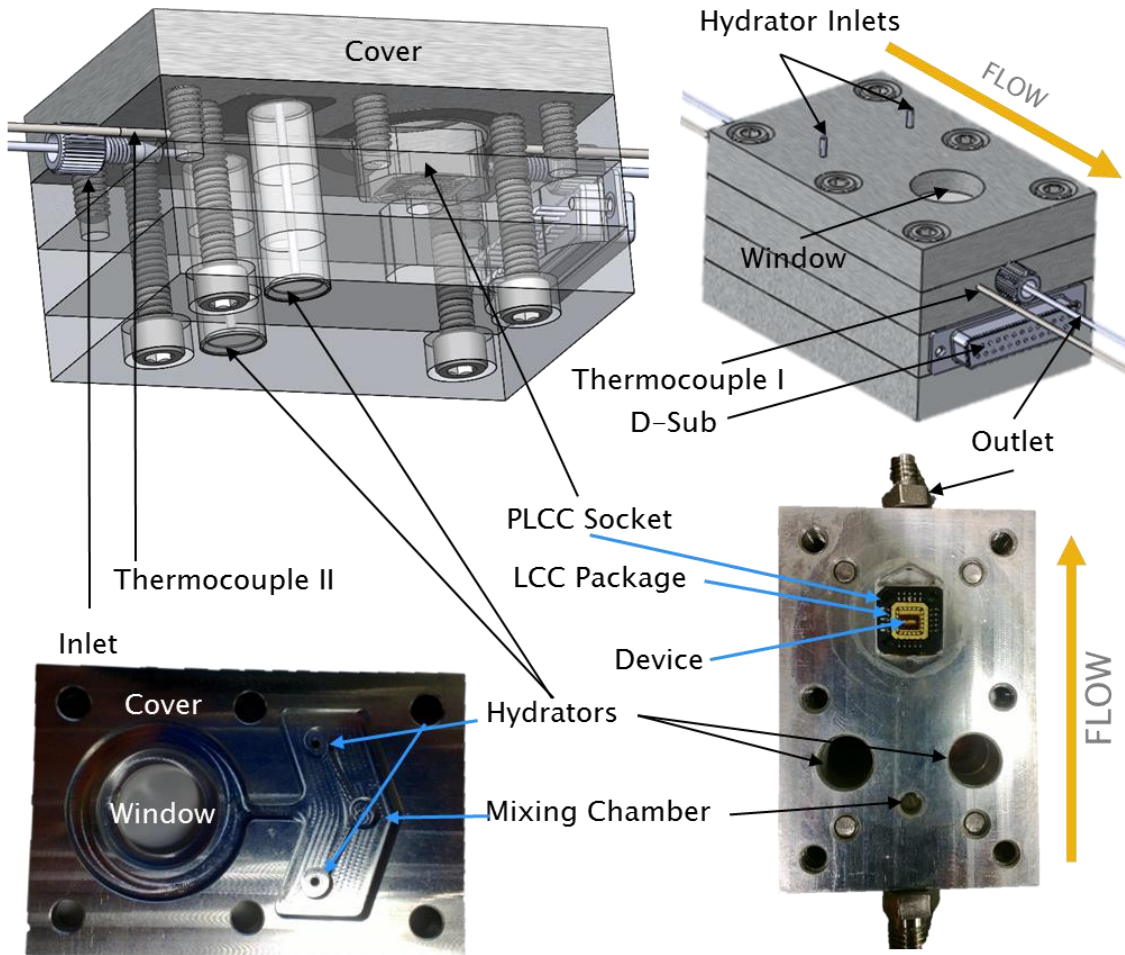


**Figure 2-10: New flow cell to test next generation devices. Low signal noise and high thermal stability.**

All layers were machined out of 6061 Aluminum alloy and was fabricated predominantly by E-Machine Shop. Four identical cells were ordered with final machining and assembly done in house. Bottom three layers were fixed with four 1/4"-20 bolts made from 18-8 stainless steel. O-rings were installed in between each of the

bottom three layers in the locations of hydrator holes to ensure sealing under vacuum and pressure. D-Sub socket was installed in second layer from the bottom with wires connecting to the PLCC socket through a countersunk hole in the third layer from the bottom. Two part 20 minute epoxy was poured to seal this hole completely, isolating the device chamber from bottom two layers.

Cover was fitted with a high strength  $\frac{1}{4}$ " extreme temperature quartz glass window for laser or camera access. A custom Teflon seal was machined to fit in the cover and seal the hydrators and device chamber from the environment.  $\frac{1}{16}$ " through hole was machined and routed through the mixing chamber and the device chamber. Swagelock fittings at both inlet and outlet of the channel ensured isolation of the flow cell from the environment.

Hydrator volume was reduced from 100mL to 2mL, with two hydrators included in each test cell. Hydrator temperature was measured by thermocouples I and II at two points to check for temperature uniformity during the experiment. One thermocouple was used to record the temperature while the other thermocouple was used to control the temperature of the cell and was connected to the PID temperature controller. Thus, the new design ensured temperature of the device, purge gas and analyte were all the same. Pressure tests were performed to ensure no leaks in the flow cell (-30MPa for one hour and 40 PSI for one hour). Both hydrator inlets and test chamber inlet/outlet were fitted with Swagelock valves to allow for isolation of the device from environment during experiment setup. Thermal mass of the test cell was increased by a factor of 10 to improve temperature stability during the experiment.

Finally, due to reduced volumes of analyte, as well as consistent tubing diameter throughout the hydrator/mixing chamber and exposure chambers, a reduction in gas flow rates was appropriate. 20 SCCM or lower MFC's were used for the hydrator lines while a single 100 SCCM MFC was used for purge line. Lower flow rates potentially played a factor in reduced signal to noise ratio and substantially reduced costs of ultra-high purity

nitrogen due to increased number of experiments per tank. Old system was capable of running 10 experiments per nitrogen tank vs. 30 experiments per tank using new system.

#### 2.4.2 Improved Procedure for Analyte Handling

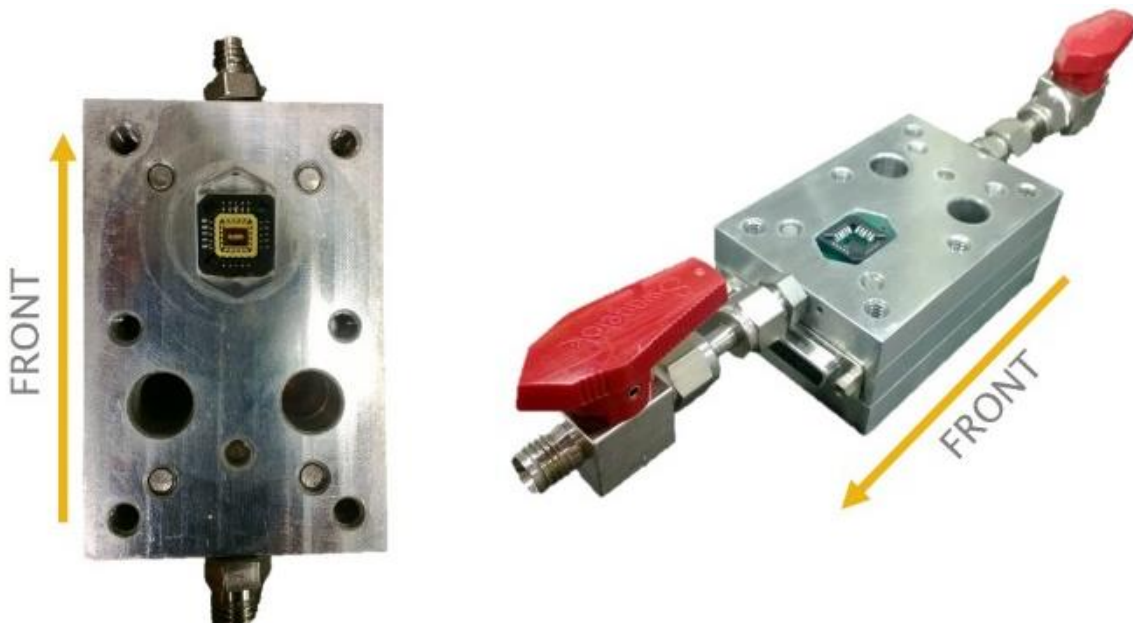


Figure 2-11: Test cell with cover removed showing the shutoff valves.

Due to added vacuum capabilities and reduced volume of analyte required for each test, anhydrous analytes became a financially viable option for device testing. Proper MOF dehydration techniques were thus developed to ensure experiment purity. Valves were installed at all inlets and outlets of the test cell allowing for complete isolation of internal tubing from atmospheric conditions (Figure 2-11).

The following procedure was used when testing devices using the new experimental cell:

1. Devices with MOFs were placed for 24 hours in the glove box with silica desiccant (Figure 2-12).
2. Device was removed from glove box and inserted in the test cell.
3. Cover was installed and bolted.
4. All three inlet valves were rotated to the off position.

5. Exit valve was rotated to on position and connected to an oil free scroll pump.
6. Cell was heated to 50°C
7. The chamber was evacuated for 1 minute.
8. Exit valve was rotated to the off position and pump was shut off.
9. Test cell was moved into a glove box maintained at 0% humidity and pumped with nitrogen.
10. Anhydrous analyte was loaded into the test cell inside the glove box environment and all inlets/outlets were closed prior to removal of the test cell from the glove box.
11. Test cell was connected to the flow setup.
12. Flow setup tubing was purged with nitrogen for 1 minute.
13. Test cell valves were opened and LabView experiment was started.
14. A 5PSI one way valve was installed at the outlet valve to ensure no atmospheric air can enter the system once the experiment concludes.

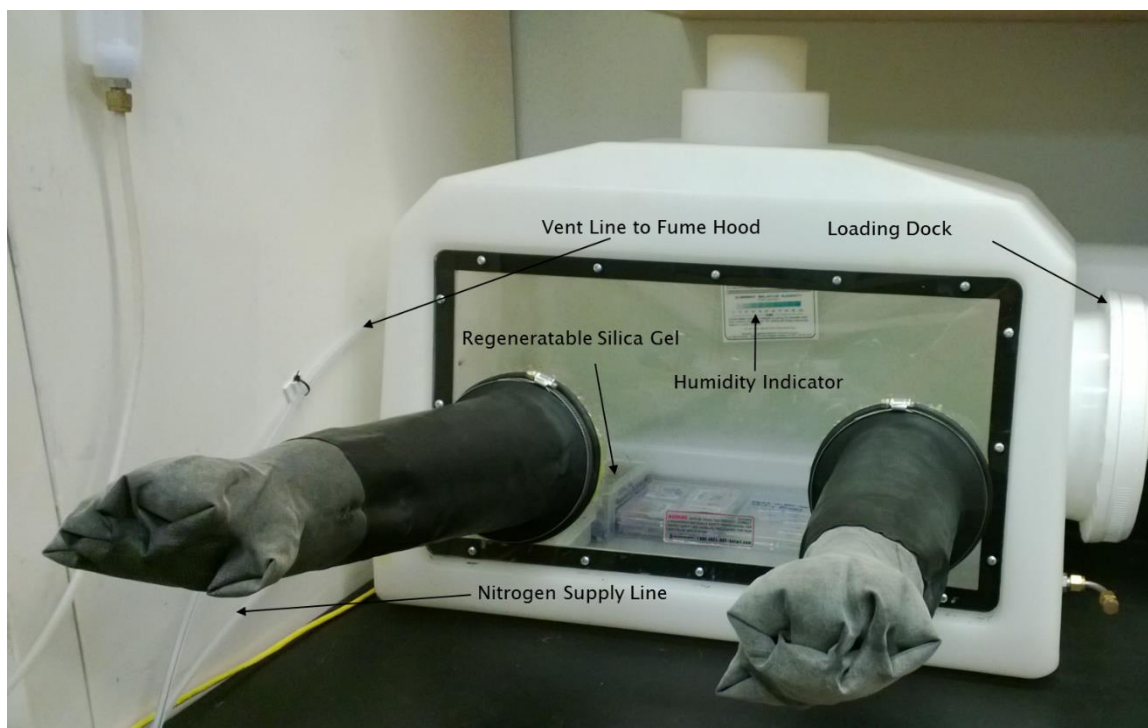


**Figure 2-12: Glove box used for device storage and analyte loading.**

## **2.5 Mixed Experimental Setup**

Due to fabrication delays, much of the testing was done using a mixed experimental setup. Reduced flow MFC's were used in conjunction with the bubblers embedded in the new test cell. Old test cell was connected in series with the new test cell, allowing for hydration and mixing of gases to take place in the new test cell, while the exposure to analytes to occur in the old test cell (Figure 2-13). Old devices with MOF coatings were used without special dehydration techniques. Analytes were laboratory grade and no special anhydrous solvents were used.

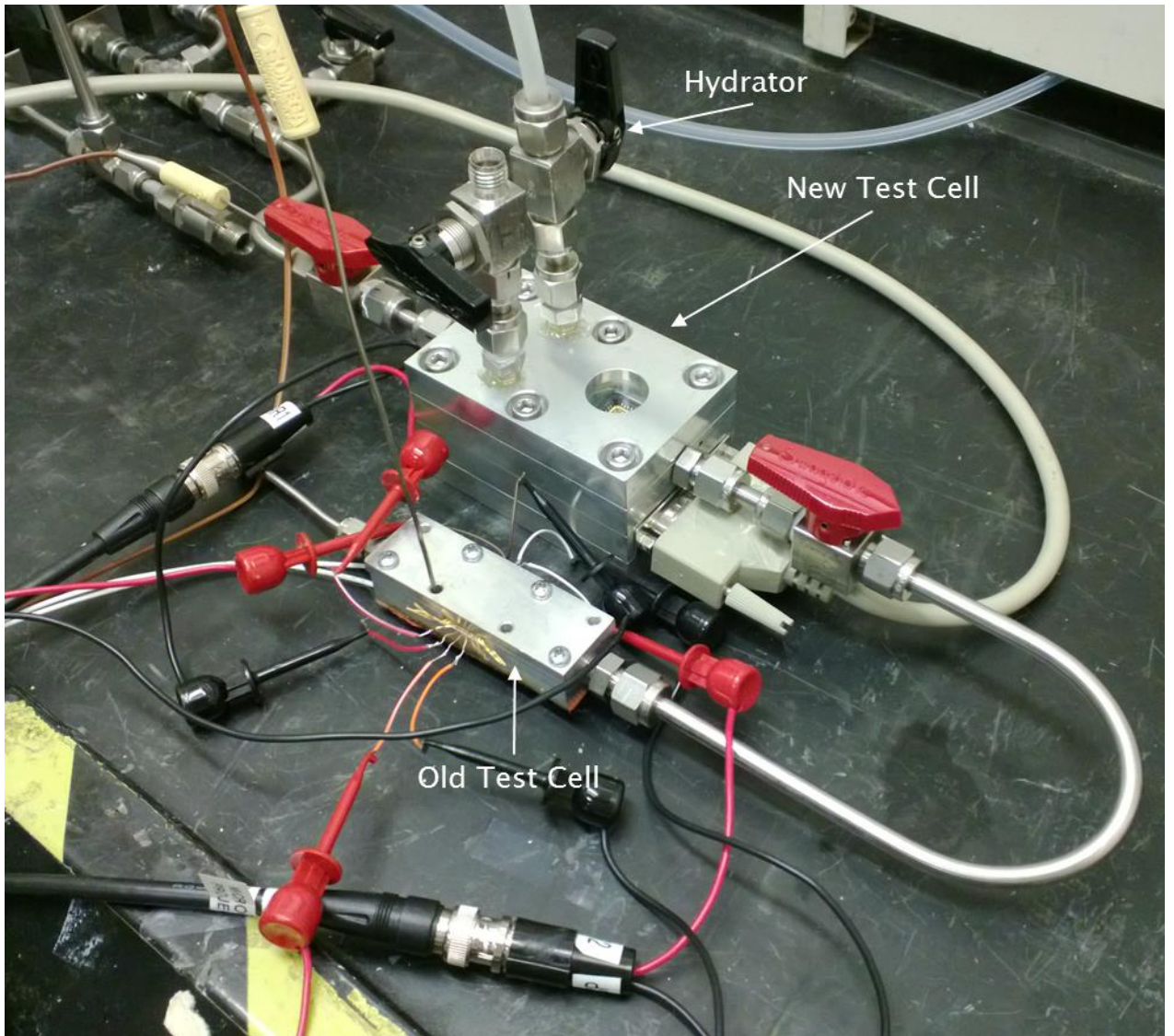


**Figure 2-13: Mixed flow setup. Hydrators from the new test cell were used to expose old style devices in the old test cell.**

## CHAPTER 3

### FABRICATION OF PIEZORESISTIVE MICROCANTILEVERS

#### 3.1 Fabrication of Euler-Bernoulli Piezoresistive Microcantilevers

Piezoresistive microcantilevers were fabricated as described in J.H. Lee et. al [14]. Three different designs (Figure 3-1) were developed with varying layer construction to test the effect of the mechanical properties of combinations of dielectric films and their influence on the relative sensitivity of the strain response of the MOF (Figure 3-2).

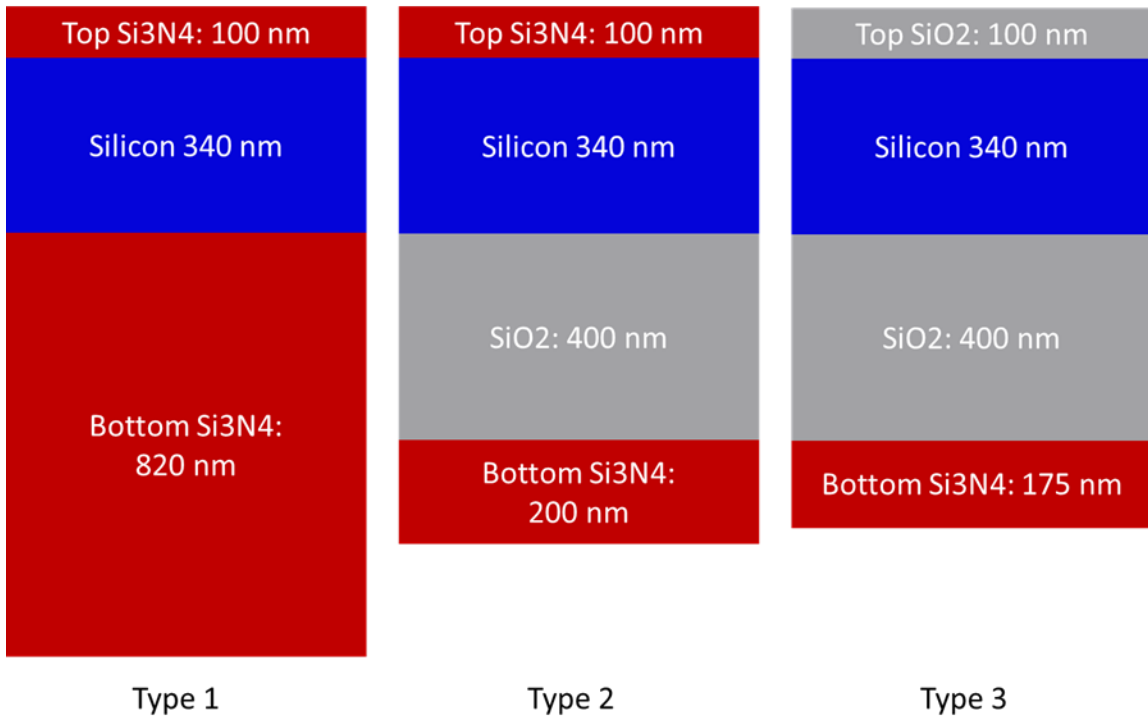
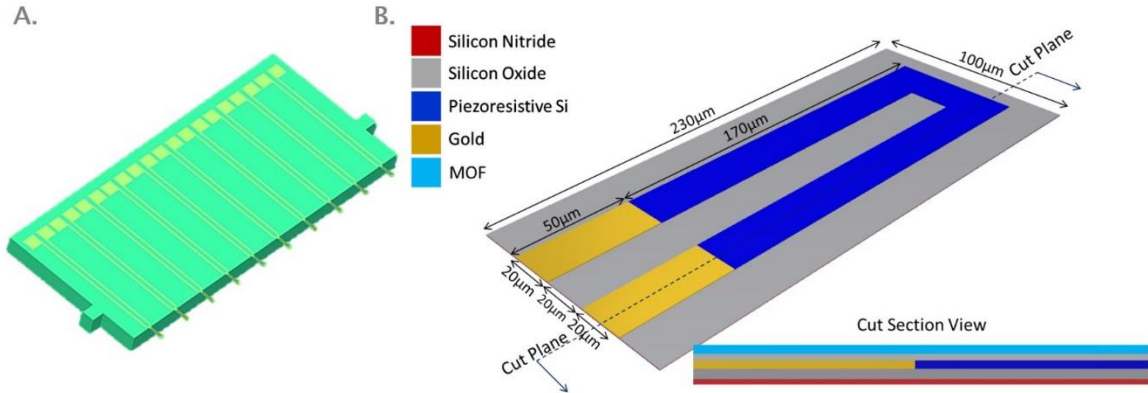


Figure 3-1: Cross sectional view of different layer configurations.



**Figure 3-2: A. CAD model of a microcantilever array. B. Schematic of a piezoresistive microcantilever.**

The fabrication process was carried out on three wafers with identical steps, with the exception of dielectric layer composition and will be briefly described here. Full details are provided in the Ph.D. dissertation of A. Chaudhury [18]. Starting with a (100) silicon on insulator (SOI) n-doped wafer, the 340nm layer of single crystal silicon (SCS) silicon was doped with phosphorous to achieve n-doping. An annealing process activated the SCS piezoresistors and reactive ion etch (RIE) was performed to shape the resistor elements. A metallization step evaporated titanium and gold contact pads and achieved electrical connection to the piezoresistive elements. Insulation was achieved by chemical vapor deposition of a 100nm layer of dielectric. To ensure high yield of released structures aluminum and nitride layers were deposited on the surface of the device, and a two-step release process was performed to suspend the microcantilevers.

Modeling was done investigate the effect of different compositions of layers on response of microcantilevers (Figure 3-3). It was revealed that  $\text{SiO}_2$  top coated microcantilevers were more sensitive to strain than microcantilevers with SAM on gold, silicon nitride coated cantilevers and alumina coated cantilevers. In addition, it was discovered that some MOFs exhibit preferential growth  $\text{SiO}_2$  substrates.

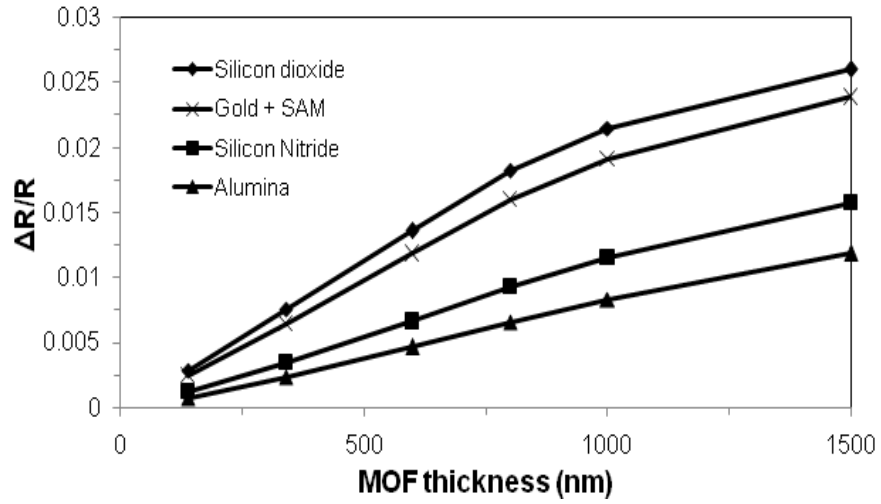


Figure 3-3: Modeling results for old type microcantilevers showing improved response of HKUST on SiO<sub>2</sub> substrates [21].

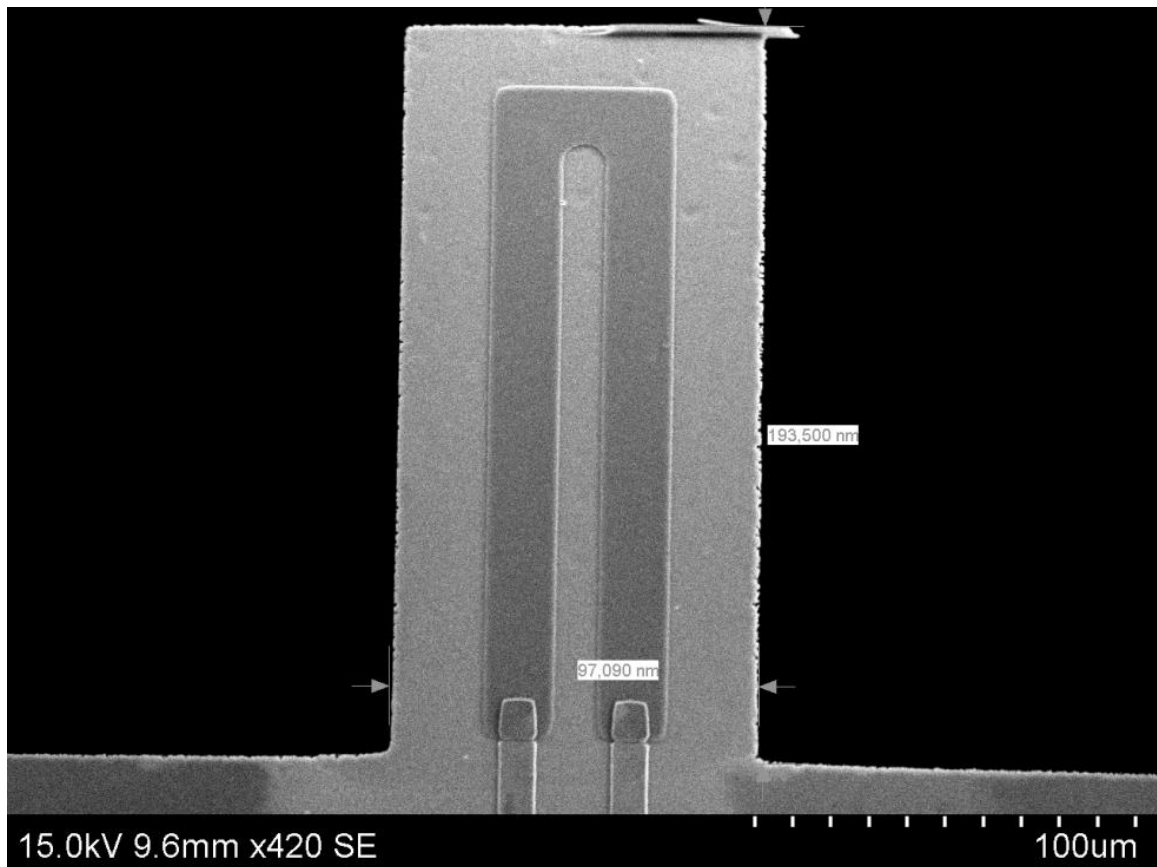


Figure 3-4: Scanning Electron Microscope (SEM) image of old design piezoresistive microcantilever.

## **3.2 Fabrication of Temperature Compensated Wide Piezoresistive Microcantilever Plates**

Unlike sensitivity in optical and frequency based cantilever systems, piezoresistive microcantilever sensitivity greatly depends on the modulus of elasticity (E) and the flexibility of the beam, quantified by the stiffness constant (k). The most effective method for improving the flexibility of suspended beams is to reduce the thickness of materials with high moduli of elasticity, reducing the effective stiffness of the beam. Resulting cantilevers bend and elongate at lower strains, increasing sensitivity and lowering the limits of detection. Thus, due to high modulus of elasticity of SCS as compared to moduli of other layers such as SiO<sub>2</sub>, reduction in thickness of the piezoresistor corresponds to an increased response and lower limits of detection. The silicon nitride (SiN<sub>4</sub>) was removed as a structural layer from the device due to its higher modulus of elasticity compared to that of SiO<sub>2</sub> and was used strictly for passivation. Silicon nitride has a decreased likelihood for corrosive analyte or water vapor to penetration in the film [22]. The nitride layers were coated with a thin layer of silicon dioxide layer, to provide preferential growth of MOFs such as CuBTC compared to the nitride film on the back of the cantilever.

### **3.2.1 Modeling Results**

Optimization of the dimensions of the cantilever and selected layers was implemented using COMSOL modeling by Dr. Venkatasubramanian [21]. Width of the microcantilevers as well as shape and geometry of the doped SCS was varied to investigate its effect on the sensitivity to stress. A surface strain was induced in the model via volumetric expansion of a simulated MOF layer based on artificial change in temperature. Strength of response was gauged based on percent change in resistance exhibited for each value of induced constant strain. The modeling showed that a wider microcantilever with two piezoresistors close to the axis of symmetry, resulted in the

strongest change of resistance per induced unit of strain compared to narrow beam and placement of the piezoresistors at other locations on the plate. Final dimensions [21] were selected as  $720\ \mu\text{m} \times 230\ \mu\text{m}$  while the layer configuration thickness will be discussed in section 3.2.3.

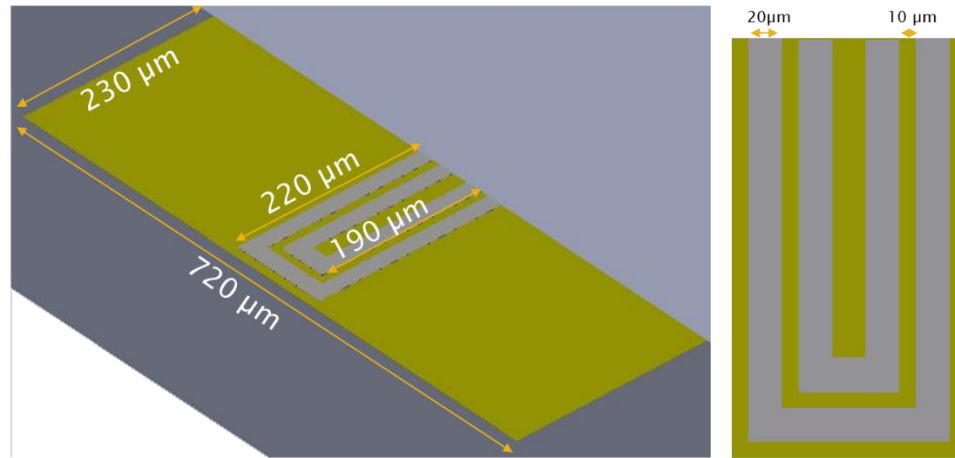


**Figure 3-5: Optimized dimensions for new microcantilever sensors**

## **3.2.2 Layout and Packaging**

### **3.2.2.1 Limitations of Old Device Layout**

Previous generation of microcantilevers had a number of disadvantages in terms of packaging. Firstly, each die consisted of an array of ten microcantilever devices, however, each cantilever had only a single piezoresistive element. Each wafer contained 38 dies with five bridges per die, totaling 190 bridges per wafer (Figure 3-6).

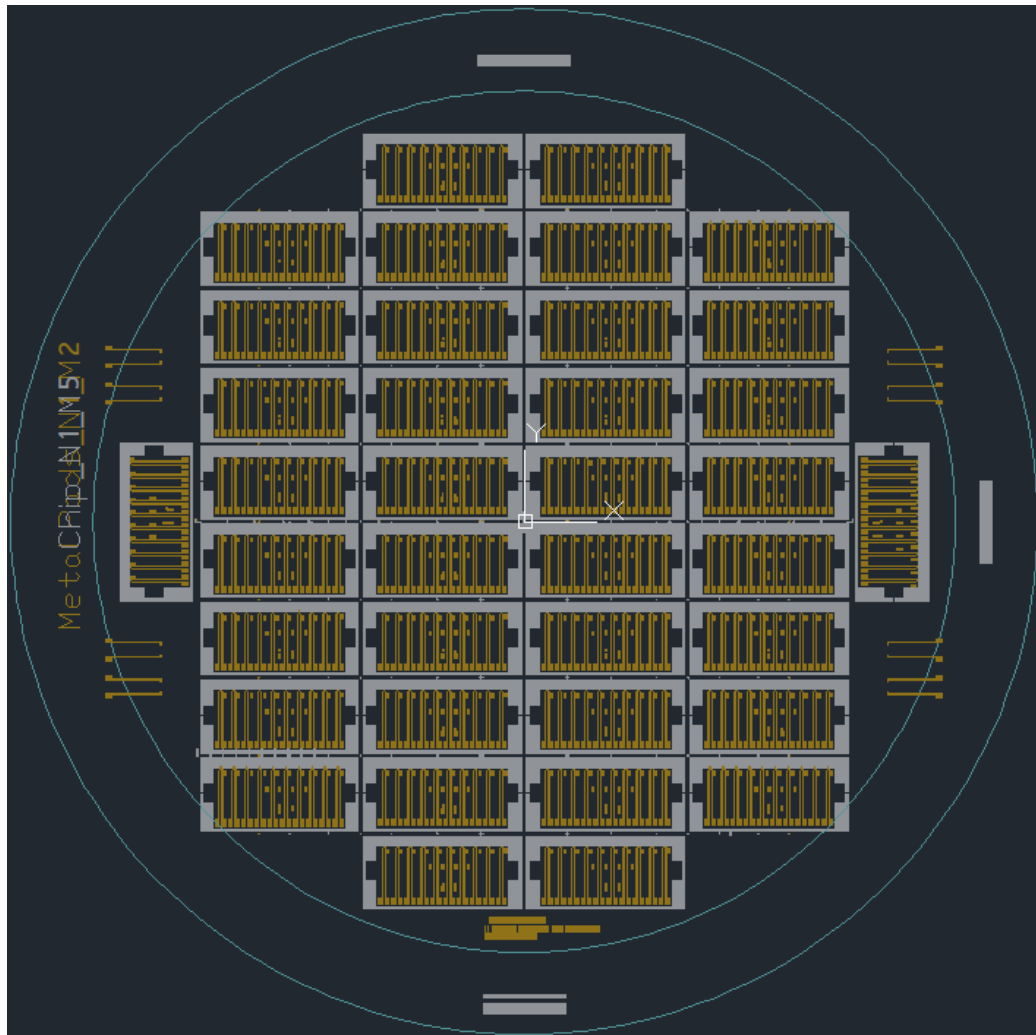


**Figure 3-6: Old wafer layout.**

Secondly, each cantilever required two contact pads, bringing the total number of pads to twenty per die. As was previously mentioned in section 2.3.1, only 12 pins were available on the package. Wirebonding to these pins was difficult due to their elevation above the die, resulting in a steep angle (Figure 3-7). This angle resulted in many failed wirebonds due to stresses created by the sharply bent wire. Each die required over an hour to wirebond.

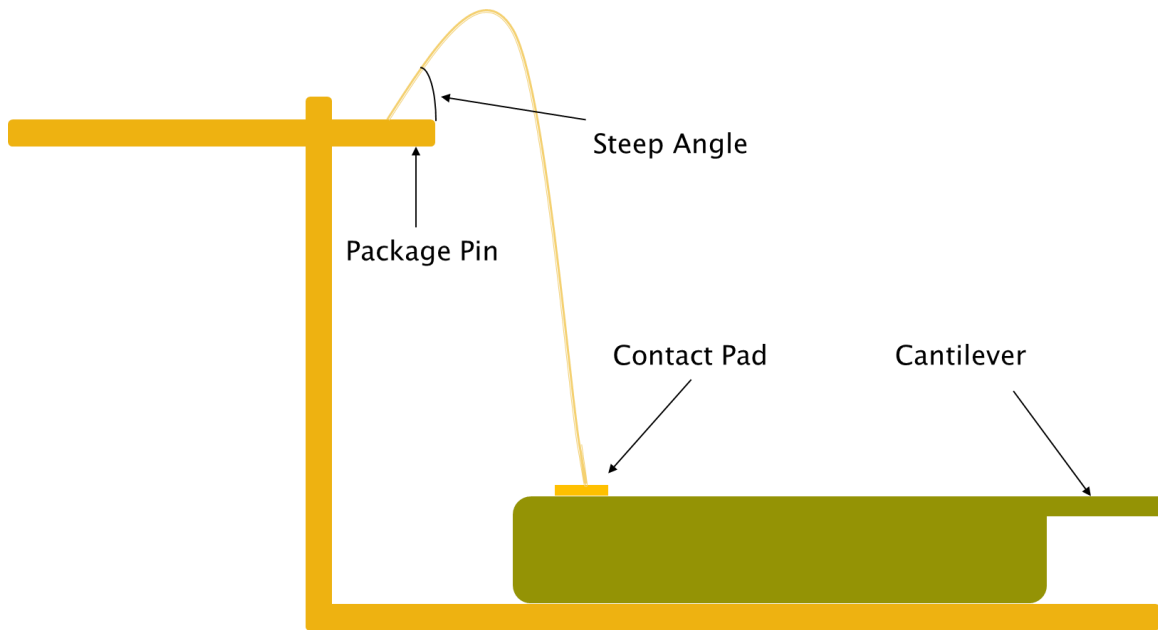


**Figure 3-7: Illustration of wirebonding angles seen with old package and device.**

Final packaging was difficult to handle leading to excessive breakage of devices during handling. This was due to the array being located on the edge of the die, leaving the devices exposed to tweezers or any other objects. Partial protection of the devices was achieved once the device was placed in the package since the package walls provided some degree of protection. As such, most damage was incurred due to handling of the devices during shipping, coating and characterization. A substantial number of devices were lost during these activities.

As previously discussed in section 2.3.1.1, the devices were sensitive to temperature changes such that any changes in temperature during the experiment would affect the collected data. This limitation introduced instrumentation difficulties to control the temperature of the experimental setup as discussed in detail in section 2.3.1.1.

### 3.2.2.2 Optimized Cantilever Die Design and Temperature Compensation

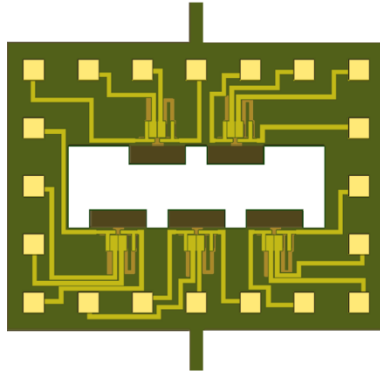


**Figure 3-8: Sample layout of the new die. Microcantilevers were surrounded on all sides by the die to protect devices from physical damage.**

To address disadvantages of the old layout, each microcantilever sensor was outfitted with two piezoresistors with each cantilever connected to a single bridge. The devices were placed in the center of the die (Figure 3-8) and surrounded by the contact pads. Temperature compensation was accomplished by placing two resistors on the die below each cantilever. The stationary resistors were identical lengths as the two resistors on the cantilever, ensuring a well-balanced bridge. Thus, any temperature changes experienced by the die would in theory change all four resistances by the same amount, hence leaving the voltage at the measurement nodes of the bridge unchanged.

The number of dies on each wafer was increased to 187 due to the smaller size of each die. Each wafer was divided into two halves, with half of a wafer consisting of optimized design cantilevers (Figure 3-8) while the other half contained variations of the optimized design with specific improvements which will be discussed next. Overall, the number of Wheatstone bridges per wafer increased by over four times to 827 (Table 3-1). If a single design was implemented in the future, then 935 complete Wheatstone bridges can be placed on a single wafer.

**Table 3-1: Die distribution for new wafer layout.**

Type	Number of Bridges	Number of Dies
Optimized	470	94
Optimized Devices with Heaters	81	27
Optimized Devices with Heaters and Cutouts	81	27
Old Geometry Devices	45	9
Disk Structures	150	30
<b>Total</b>	<b>827</b>	<b>187</b>

### 3.2.2.3 Other Designs Fabricated on the Wafer

A few experimental designs were placed on the wafer to provide extra features and also to compare the responses for different geometries (Figure 3-10). First designs incorporated differently shaped outer piezoresistors, placed as a single outer conductor for heating purposes (Figure 3-10.A). Different shapes of these conductors were employed to study effects of geometry on heating capabilities (Figure 3-10.D-F). These conductors could also be used to measure the temperature of the cantilever.

A variation of the above design implemented small through holes located at the base of the cantilever (Figure 3-10.G-I). The intent of this design was to study effects of such cutouts on yield and on the mechanical response of the device. It was hypothesized that such cutouts would improve the response of the devices due to the added flexibility at the base of the cantilever and thermally isolate the cantilever from the silicon substrate. No COMSOL modeling, however, was conducted to substantiate this assumption.

Another design replicated the overall geometry of the old design microcantilever with dimensions identical to the previous device (Figure 3-10.C). Two piezoresistive elements were placed on the surface (Figure 3-10.K), and a complete Wheatstone bridge was fabricated for these devices, thus allowing temperature compensated data to be collected for direct comparison to the wide design devices.



**Figure 3-9: Wafer layout.**

The final geometry was a circular disc suspended by four microbridges (Figure 3-10.B). This is based on the work of G. Yoshikawa et. Al. which demonstrated higher sensitivity for disk shaped bending stress sensors compared to cantilever surface stress sensor [23], [24]. The piezoresistors embedded in the bridges formed two distinct strain gauges which were connected as a Wheatstone bridge to two stationary resistors (Figure 3-10.J). The surface area of the disk was equal to the surface are of the wide design microcantilevers for direct comparison of response ( $.165600\text{mm}^2$ ). Overall wafer layout is shown in Figure 3-9.

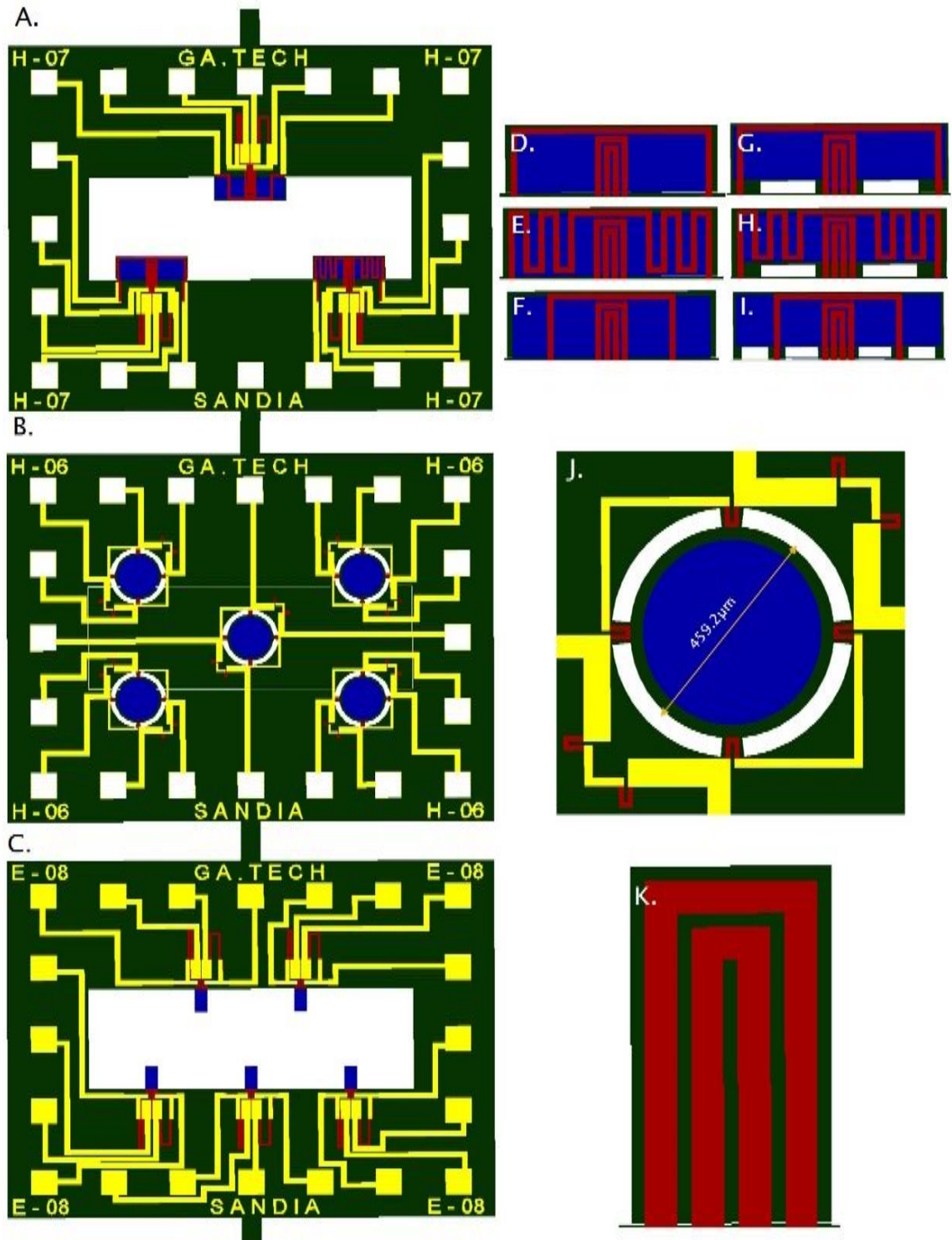


Figure 3-10: (A) Die layout for 3 devices with different shape heaters. (B) Disc layout. (C) Original cantilever layout. (D-F) Different shapes of heating resistors with no cutouts. (G-I) Heating resistors with cutouts. (J). Disk. (K) Old type cantilever.

### 3.2.3 Fabrication Process

Piezoresistive microcantilever sensors were fabricated using traditional microfabrication techniques [25]. Detailed fabrication steps are available in APPENDIX A. Silicon-on-insulator (SOI) wafers were purchased with a 340nm single crystal silicon (SCS) on a 400nm thermal oxide ( $\text{SiO}_2$ ) substrate (Figure 3-11.A). Wafers were outsourced for phosphorous implantation and doping (n-doped) at an external facility. Shipley Microposit 1830 positive resist was patterned using a chrome mask and Karl Suss MA6 mask aligner (Figure 3-11.B). Piezoresistors were etched using dry reactive ion etching (RIE) plasma (Plasma-therm RIE), and photoresist was subsequently removed using acetone (Figure 3-11.C). Thermal oxide was grown in Tystar furnace, resulting in the SCS layer being consumed to a final thickness of 130nm with a 400nm  $\text{SiO}_2$  encapsulating the piezoresistors (Figure 3-11.D). Thinning out of the piezoresistor in this step reduced the effective stiffness of the cantilever to improve overall device response.

To improve reflectivity of the devices for measurement of the resonant frequency of the cantilever, a 40nm layer of aluminum was evaporated using CHA-2 Electron Beam Evaporator (Figure 3-11.E). Aluminum was selected due to its high reflectance even at low coat thicknesses and for superior reflectance in the low wavelength range as compared to gold and silver (Figure 3-13). Shipley positive photoresist and aluminum etch were used to remove aluminum from the wafer, leaving micro mirrors on the surface of the devices (Figure 3-11.F).

Contacts were patterned using positive photoresist, with multiple contact windows, as shown in Figure 3-12. This was done to lower the contact resistance to the piezoresistive layer. Plasma-therm RIE was used to etch the  $\text{SiO}_2$  forming the contact windows. In addition, the outline of the cantilevers and dies was etched in this step also.

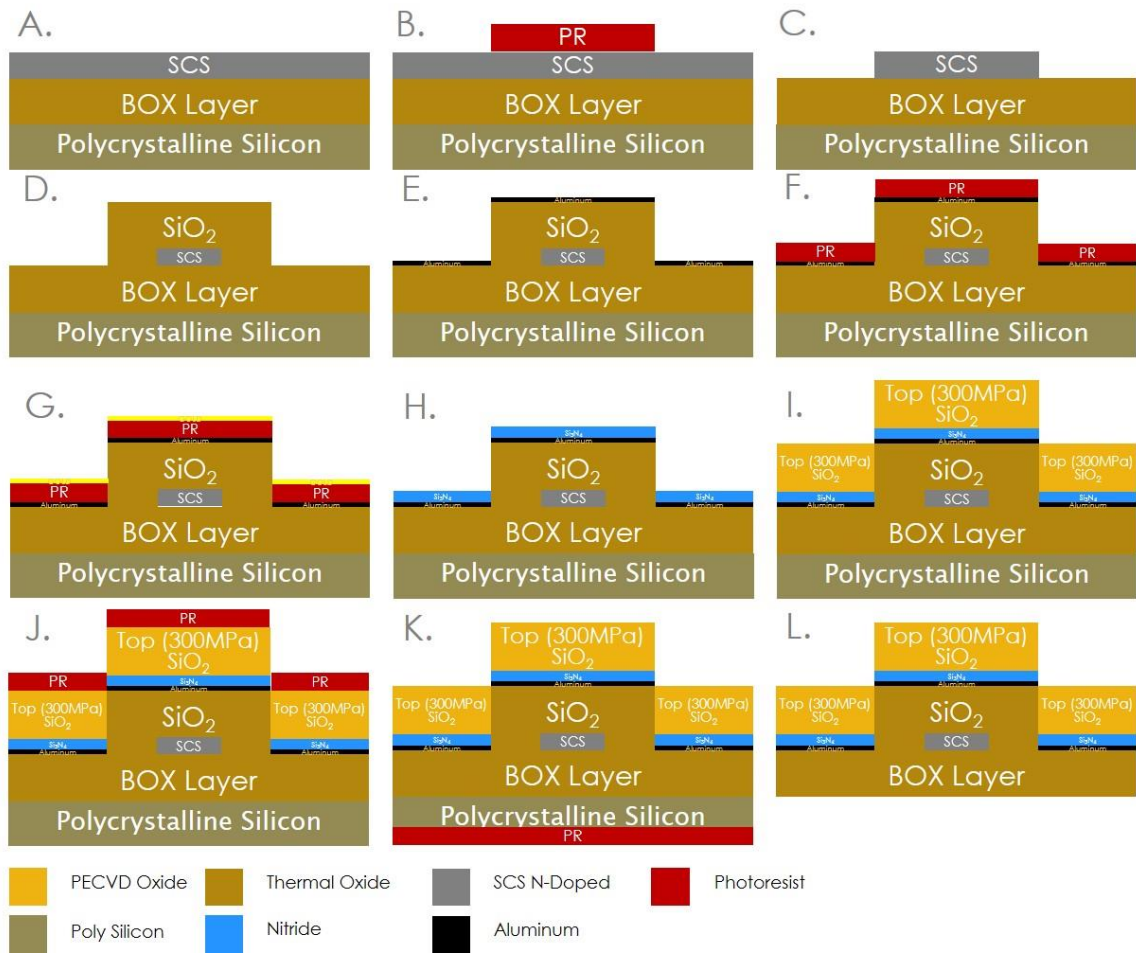


**Figure 3-11: Highlights of the fabrication process.**

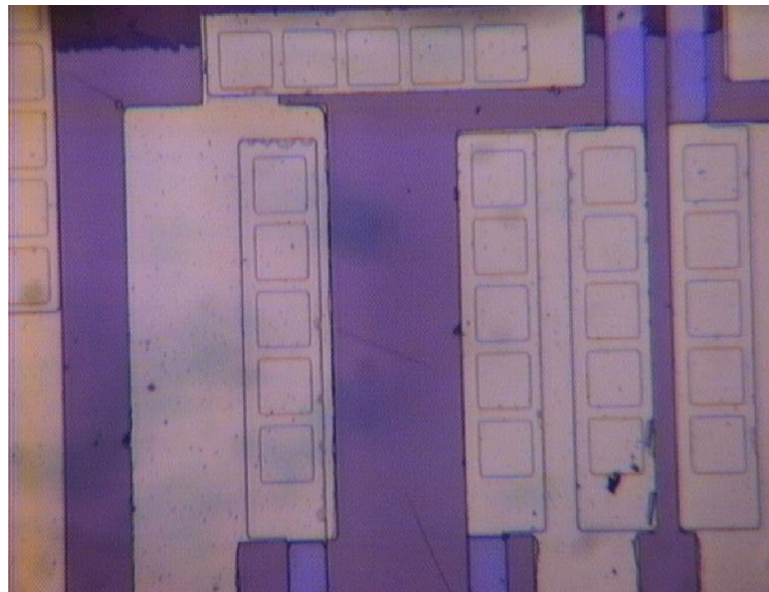


**Figure 3-12: Multiple contact windows to lower resistance to piezoresistive layer.**

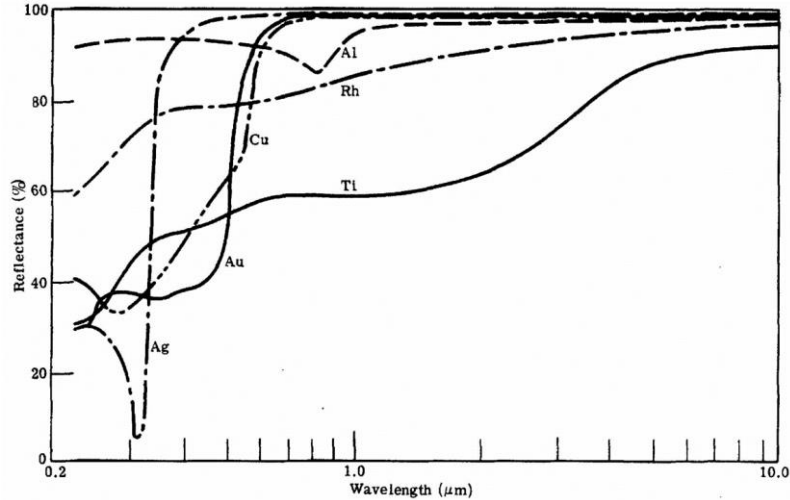


**Figure 3-13: Reflectance of Aluminum, Silver and Gold at varying wavelengths [26].**

Negative photoresist (NR71-3000P) was used to pattern gold wires and contacts (Figure 3-11.G). CVC Electron-Beam evaporator was used to coat a 50nm titanium adhesion layer, 100nm platinum barrier and 500nm thick gold layer. Gold liftoff was achieved by soaking the wafer in acetone overnight. An annealing step was performed at 330°C in nitrogen overnight to improve bonding between the doped silicon and metal contacts.

Using Oxford Inductively Coupled Plasma PECVD (ICP PECVD) nitride recipe, 100nm layer of low temperature SiN<sub>4</sub> was deposited as a passivation layer (Figure 3-11.H). Next, stress compensated SiO<sub>2</sub> was deposited using STS 2 PECVD (Figure 3-11.I). Negative resist was used to pattern the contact pad openings as well as the outline of the cantilevers and dies. Vision RIE was used to etch SiO<sub>2</sub> and Si<sub>2</sub>N<sub>4</sub> (Figure 3-11.J). Acetone was used to remove the photoresist, finishing top side processing.

SPR220 positive photoresist was patterned on the backside of the process wafer. HMDS was spun prior to SPR 220 to ensure adhesion of the photoresist. EVG 620 backside mask aligner was used to align the back side pattern to the front side of the wafer. Crystal bond 509 by SPI Supplies was heated to 130°C and spread thinly on a carrier wafer using a razor blade. The patterned process wafer was placed on top of the

carrier wafer and wafer flats were aligned. Pressure was manually applied via tweezers to ensure uniform adhesion and the wafers were cooled to room temperature.

Final processing step was the deep RIE (DRIE) etch of the backside. First SiO<sub>2</sub> was etched away from the back side of the wafer using Vision RIE 2. Next the device was placed in STS HRM and etched for 450 cycles (0.9µm/cycle) etching majority of the way through. Subsequently, the wafer was etched 30 cycles at a time until all dies were etched all the way through. The wafers were soaked in acetone overnight and the carrier wafer was removed from the process wafer by sliding them in opposite directions relative to each other. In order to avoid damage to cantilevers, the wafers were slid perpendicular to the direction of the cantilevers and contact between the process wafer and the carrier wafer was maintained throughout. Lifting the wafer up was shown to destroy the cantilevers due to capillary forces from the acetone.

A final AMI (Acetone, Methanol, Isopropanol) wash was performed on the released devices to ensure crystal bond has been dissolved completely and no residue remained. The final step was performed by placing the wafer in a 150mm diameter Pyrex dish (17mm deep). A syringe was used to submerge the wafer in each of the chemicals in order (Acetone, Methanol then Isopropanol). Liquids were syringed in very slowly to reduce likelihood of physical damage to devices. To vacate the dish, the syringe was used to slowly remove the liquid. Repeating the AMI wash three times ensured no residue remained on the surface.

### 3.2.4 Fabrication Challenges

#### 3.2.4.1 Selecting Stress Compensation Values

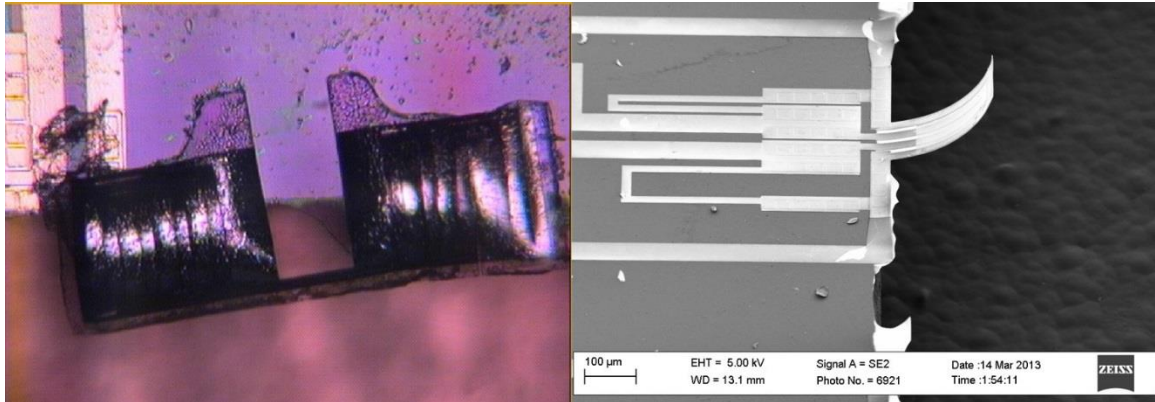


**Figure 3-14: All the devices on process wafer 1 were damaged with wide portions of the cantilever breaking off and the middle section with piezoresistors A and B remaining intact but highly stressed. Left- optical image of broken off wide portion of cantilever. Right – SEM of remaining center piezoelement.**

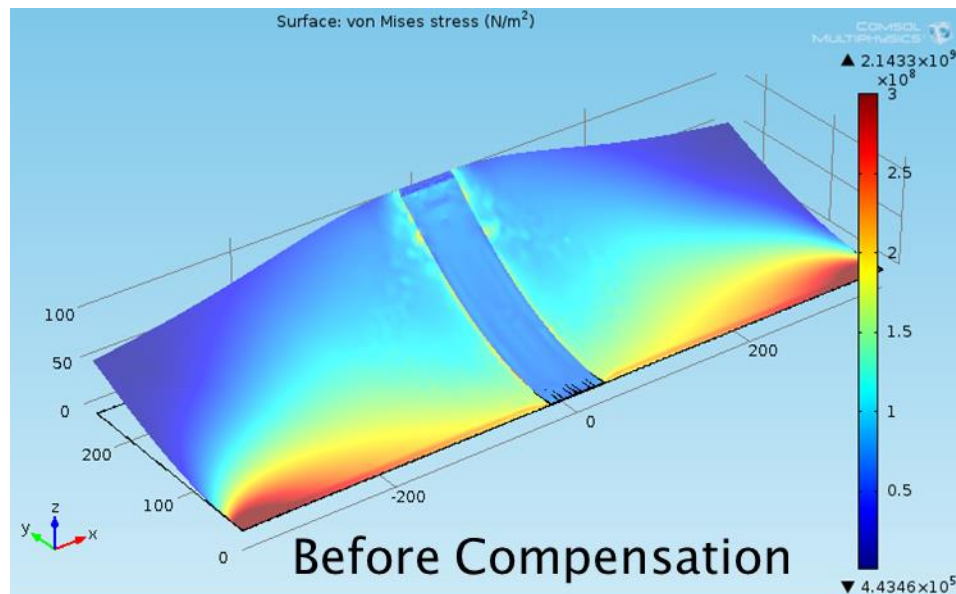


**Figure 3-15: COMSOL model with estimated original layer stresses. Curvature of device in model reflected SEM images of damaged devices. Stresses at the base and around the piezoresistor were above failure threshold for materials.**

Breakage on the first released process wafer was not consisted with previous test wafer released run (Figure 3-14). In order to ensure flat devices and reduce number of

broken cantilevers, a COMSOL model was implemented to calculate the correct stress value for the top layer. Layer thickness was defined as 400nm of top oxide, bottom layer was set to -320 MPa compressive stress, a typical value for thermal oxide. Geometry and other layers were assumed to be stress free and were modeled with appropriate thickness and dimensions (Figure 3-15). Top layer stress was varied until the model predicted a flat microcantilever structure (Figure 3-16). This value was determined to be -300MPa of compressive stress.

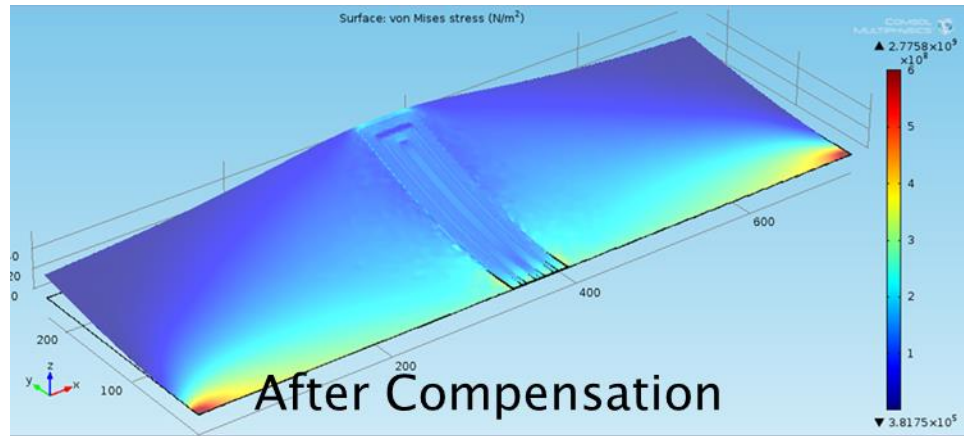


**Figure 3-16: COMSOL model predicted 400nm of SiO<sub>2</sub> at -300MPa of compressive stress on top would flatten the beam and reduce stresses below failure threshold.**

#### 3.2.4.2 Tuning SiO<sub>2</sub> Recipe

PECVD systems and recipes are designed for low stress film depositions, therefore, it was necessary to adjust the recipe chemistry to achieve the required stress. BowOptic 208 stress measurement tool was used to calibrate five fresh test wafers, it was important to use fresh wafers, since reclaimed wafers may have residual curvature due to the reclaim process. Each wafer's curvature was measured before and after deposition of 400nm thick PECVD SiO<sub>2</sub>. Oxide stress was measured for the Oxford PECVD, Unaxis PECVD, STS PECVD, STS PECVD 2 and Oxford ICP PECVD. Majority of the recipes resulted in 10MPa to -10MPa stress range, however, STS PECVD 2 standard recipe yielded -350MPa of compressive stress. To reduce the stress to the desired value, the

ratio of  $N_2O/SiH_4$  was reduced, resulting in a -300MPa film at 400nm thickness (Figure 3-17).

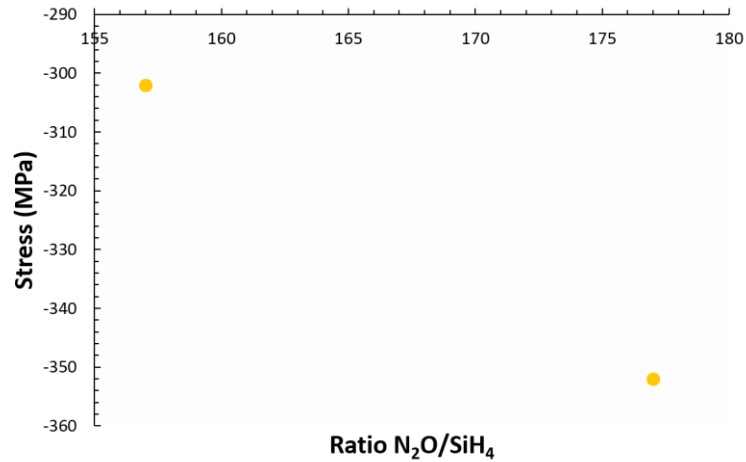


**Figure 3-17: STS PECVD 2 film stress vs.  $N_2O/SiH_4$  ratio.**

#### 3.2.4.3 Selection of DRIE Tool

Original process used by Dr. Lee [14] outlined the use of STS ICP for the backside release of the microcantilevers. Initial test runs with the new masks showed substantial residue of material was left on the wafer when using this method (Figure 3-18). The residue was from *cool grease*, a paste by AIT used to adhere the carrier wafer to the process wafer and to aid in heat transfer during DRIE etching. Difficulties of removing the residue using toluene, hexane, acetone and other solvents led to the desire to replace cool grease with an alternative.

In the original process ([18], [14]), aluminum masking layer was used to define the layout of the cantilever and support the devices during the backside silicon DRIE release to increase the yield of the microcantilevers. When using this process the step for etching away the aluminum aided in the removal of *cool grease* residue from the surface of the devices, leaving a cleaner substrate. To reduce the number of fabrication steps for the new fabrication process, the aluminum masking step had been removed. It is likely that due to the removal of this step test wafers in STS ICP displayed substantial residue from the *cool grease*.

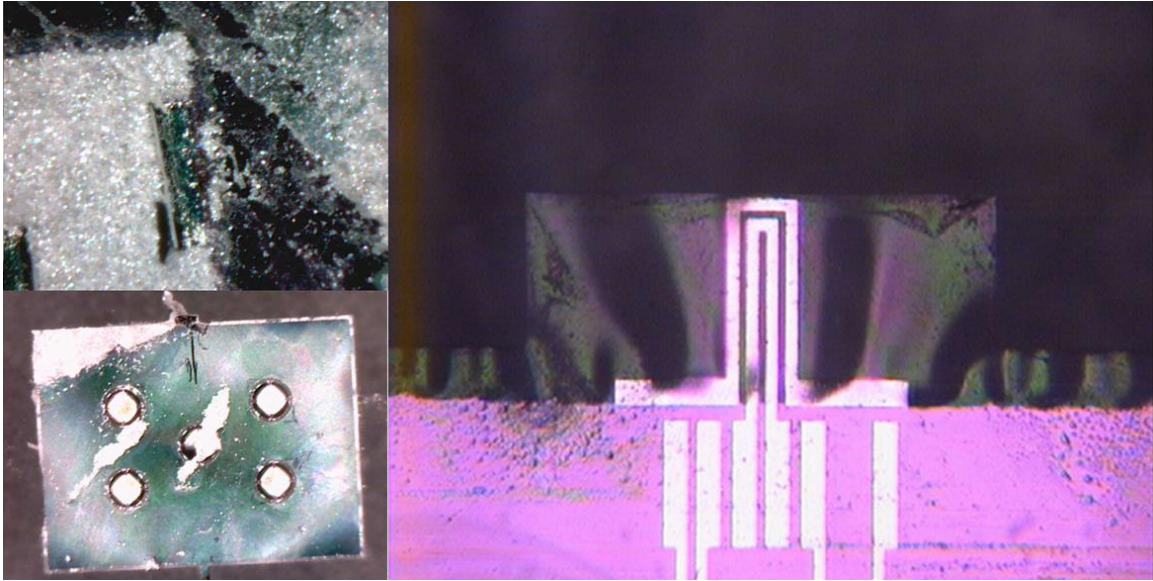


**Figure 3-18: Left - cool grease residue seen after release of a test wafer. Right - test wafer released using STS HRM with crystal bond.**

A substitute polymer was identified to replace *cool grease* as the adhesion layer. Crystal Bond 509 by SPI supplies is a polymer with a low melting temperature used as the bonding media for etching in the STS HRM. Replacing *cool grease* with Crystal Bond 509 did not show a reduction in etching performance of the tool with etch rates remaining constant ( $0.4\mu\text{m}/\text{cycle}$ ) and etch profiles unaltered. Acetone completely dissolves crystal bond, and subsequent wash in methanol and isopropanol leaves a residue-free substrate.

To further improve the performance of the DRIE step, STS ICP was replaced with the STS HRM. Although the STS ICP was a better characterized tool with a well-tuned recipe, its relatively slow etch rate was a significant disadvantage. Further, after etching through the majority of the wafer it was necessary to switch to a different recipe, since the etch rates and profiles change significantly as the trench depth increases. Etching for  $400\mu\text{m}$  was done using Module 1 recipe, while the last  $100\mu\text{m}$  were etched using Module 2 recipe (Figure 3-19). These drawbacks resulted in release time of roughly six hours per

wafer. Difficulty in scheduling a tool for such a large block of time caused delays in fabrication.

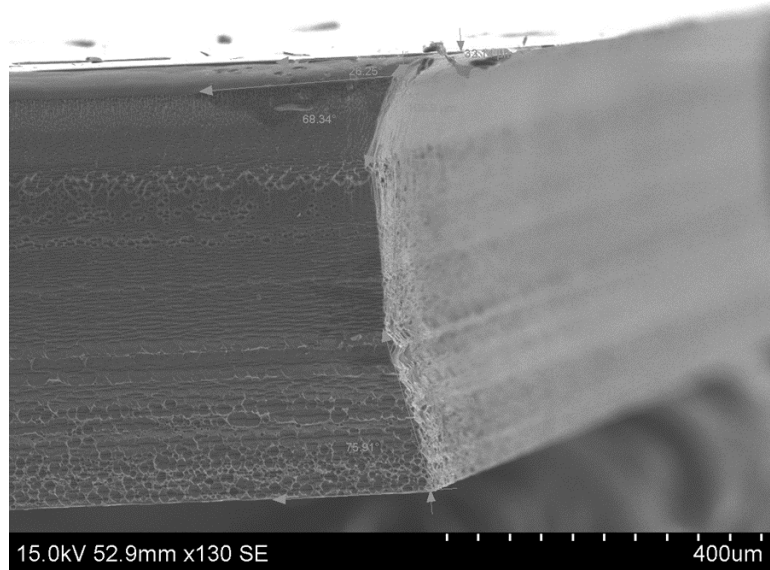


**Figure 3-19: Etch profile of STS ICP with Module 1 through etch.**

STS HRM's initial etch rates of  $0.9\mu\text{m}/\text{cycle}$  were a substantial improvement over the etch rates of the STS ICP, however, due to the novelty of the tool no fine-tuned recipes were available. The standard recipe on the tool resulted in silicon grass growth (Figure 3-20) at the bottom of the trench at depth of roughly  $300\mu\text{m}$ . To address this issue, etch intensity of the Bosch process was altered (Table 3-2). Platen power and coil generator power were increased after every cycle by a predetermined amount. Increased power ensured full removal of the passivation layer at the bottom of the trench. This adjustment resulted in improved etch profile, and resolved the silicon grass growth issue. Using this recipe a wafer could be released in as little as two hours, solving the scheduling difficulty present with the STS ICP.

**Table 3-2: Various process parameters used to adjust the etch profile and reduce silicon grass.**

# Cycles	13.56Mhz Generator Power				Platen Generator			
	Etch	Ramp Rate	Passivation	Ramp Rate2	Etch2	Ramp Rate3	Passivation2	Ramp Rate4
300	2200	5	1500	0	40	0.5	0	0
300	2200	4	1500	0	40	0.4	0	0
300	2200	3	1500	0	40	0.3	0	0
200	2200	2	1500	0	40	0.2	0	0
300	2200	3.5	1500	0	40	0.35	0	0
300	2200	3.3	1500	0	40	0.33	0	0
400	2200	3.5	1500	0	40	0.35	0	0
400	2200	3.5	1500	0	40	0.35	0	0
250	2200	3.5	1500	0	40	0.35	0	0
250	2200	3.5	1500	0	40	0.35	0	0

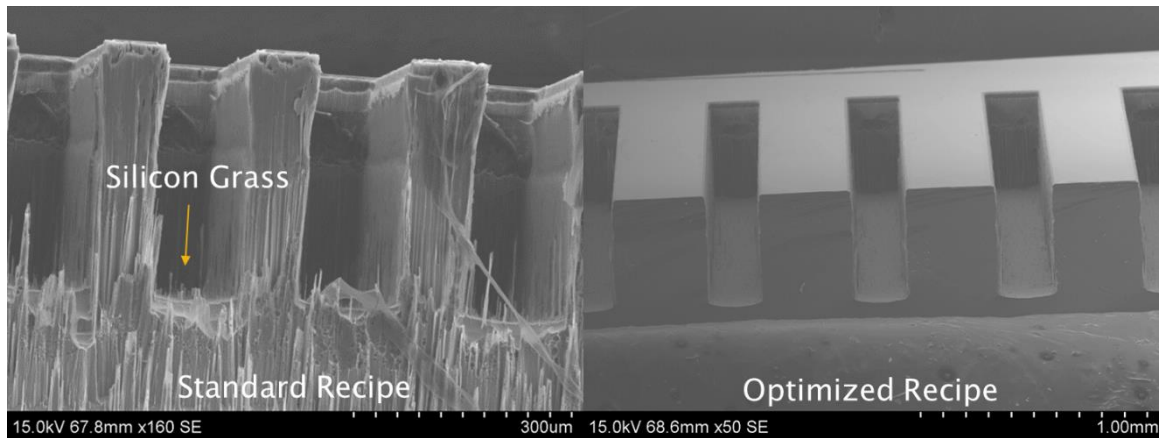


**Figure 3-20: SEM images of original recipe where silicon grass can be seen (left). Optimized recipe with well-defined trenches and no silicon grass growth (right).**

# CHAPTER 4

## CHARACTERIZATION OF PIEZORESISTIVE MICROCANTILEVERS

### 4.1 Temperature Response

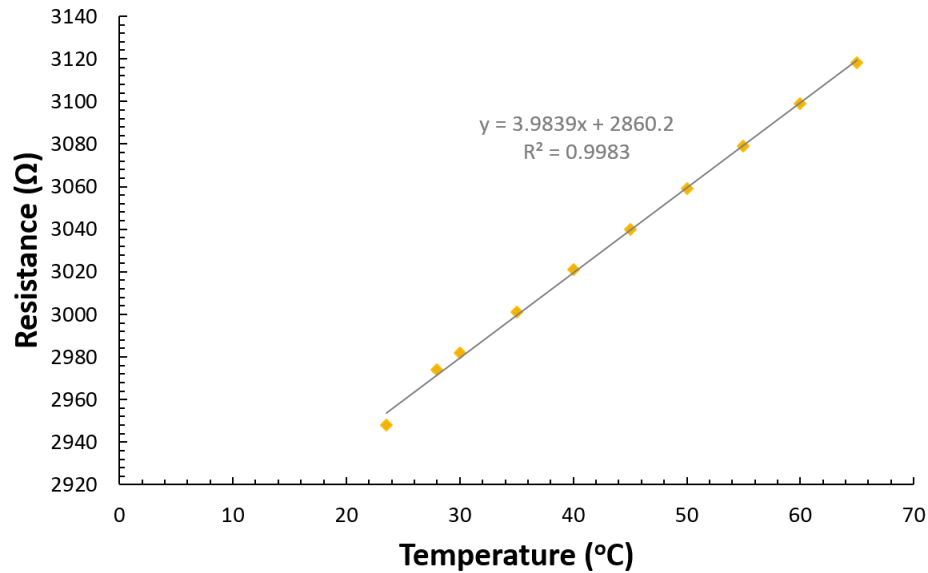


**Figure 4-1: Temperature calibration of an old type cantilever.**

Temperature calibration was performed on both old and new devices. Agilent 34401A digital multimeter was used to measure the resistance of the sensor. The sensor was placed in the test cell. Test cell was heated up to 60°C or higher, and resistance was measured for a single piezoresistive element at different temperatures throughout. Temperature was measured using K type thermocouple (Omega KMTSS-062U-6). Relations for the old devices did not include temperature compensation in any cases, however, new devices were measured with temperature compensated bridges and without temperature compensated bridges. Measurement without compensation on the new devices was performed by measuring the resistance of a single resistor on the microcantilever (resistor A).

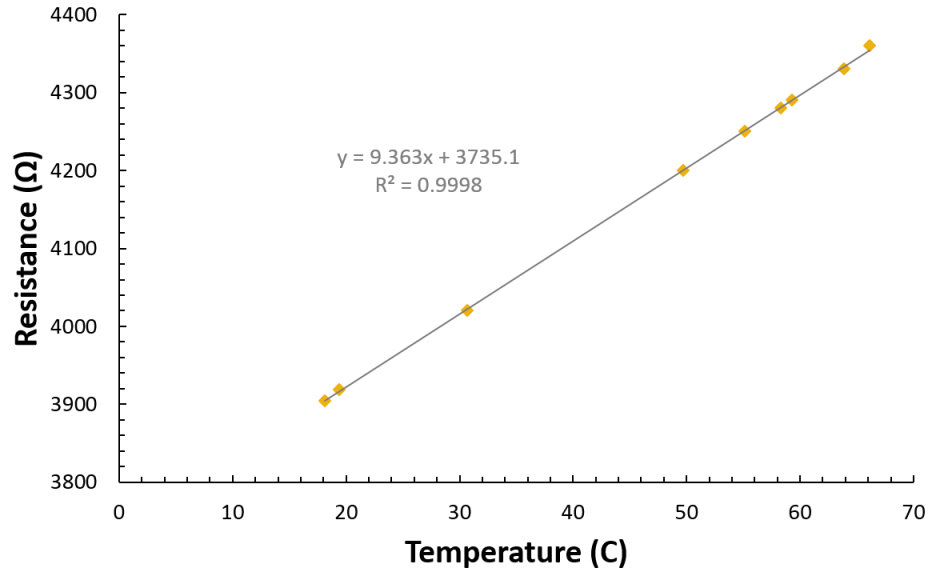


**Figure 4-2: Temperature calibration of a new type wide device without heater element or cutouts. Resistor A was used for measurements.**

Old type devices had temperature coefficient of roughly  $4.0 \Omega/^{\circ}\text{C}$  (Figure 4-1). The temperature relationship can be fitted to a linear relation with a high degree of correlation. Resistance values for the new device with no temperature compensation showed a strong correlation with similar temperature coefficient of  $9.4 \Omega/^{\circ}\text{C}$  (Figure 4-2). Addition of heating elements on the cantilever had a significant effect on the temperature coefficient with longer heating conductors resulting in lower temperature coefficients of all other resistors on the device (Figure 4-3). This suggests reduced sensitivity to bending in devices with longer heating conductors.

Temperature compensation on new devices was shown to reduce the temperature coefficient to  $2.0 \Omega/^{\circ}\text{C}$ , reducing the temperature dependence of the measurement by two times (Figure 4-4).

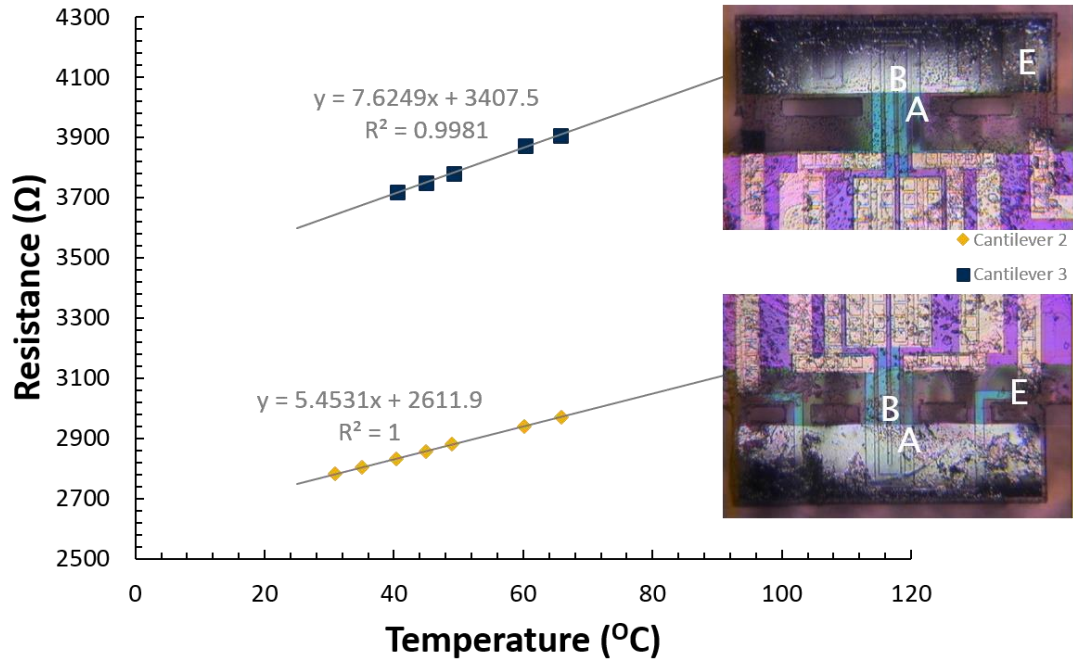


Figure 4-3: Shows significant effect of heater length (resistor E) on temperature coefficient effects comparing cantilever 2 (top image) to cantilever 3 (bottom image). In both cases resistor A was measured for temperature calibration purposes.

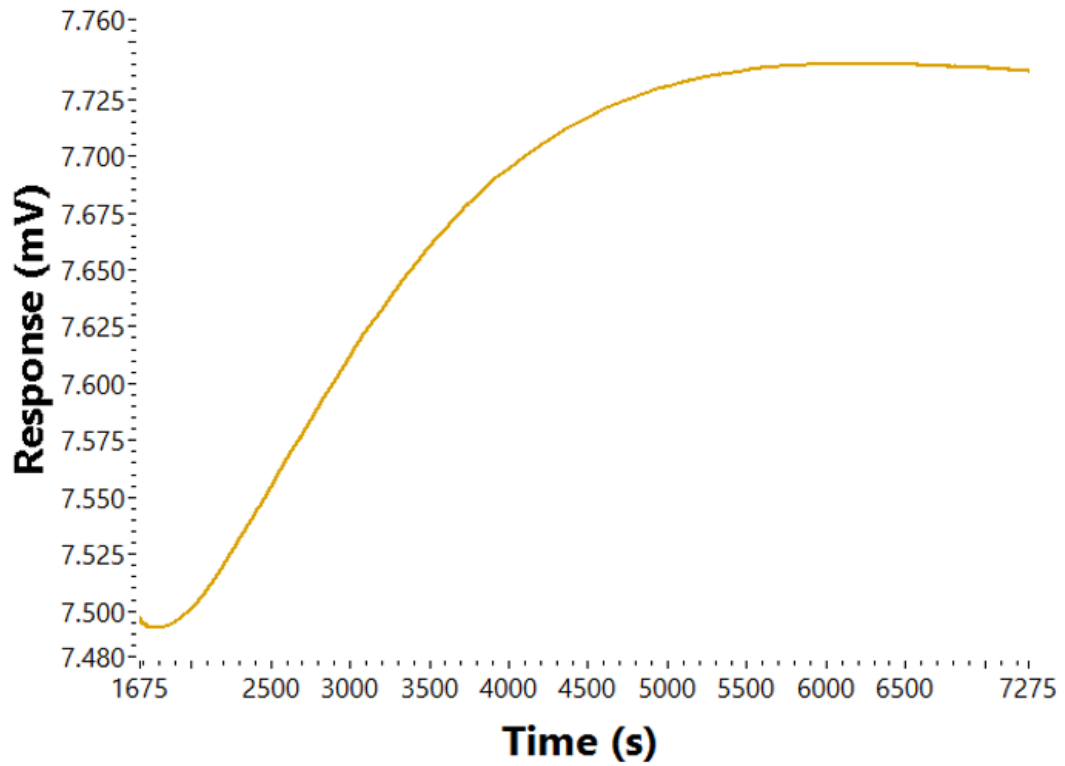


Figure 4-4: Temperature compensated bridge response to temperature from  $23^{\circ}\text{C}$  to  $100^{\circ}\text{C}$ . The voltage values correspond to  $2.0 \Omega/^{\circ}\text{C}$ .

## 4.2 Laser Mass Characterization

Attempts were made to measure deposited mass of MOF by using AFM frequency measurements before and after deposition. For a simple cantilever sensor the fundamental frequency is related to spring constant (k) and mass (m) by the following relation:

$$f = \frac{1}{2\pi} \sqrt{\frac{k}{m}}$$

Old type cantilevers with dimensions of 80 $\mu\text{m}$  by 230 $\mu\text{m}$  may be approximated using this relationship resulting in an estimate of the deposited mass. AFM optics were used to measure the fundamental frequency in thermal noise mode (no piezoactuation of cantilevers). Peaks were fitted with Lorentzian (Air) model (Figure 4-5). Measurements were repeated ten times for each cantilever to ensure statistical significance. All ten devices on old microcantilever array were measured, and frequency measurements were averaged (Figure 4-6).

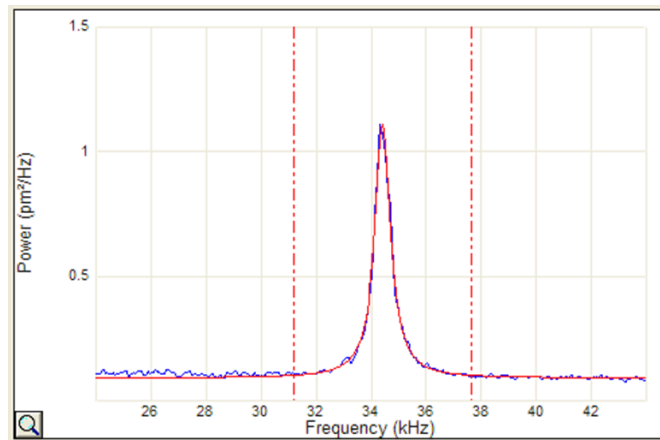


**Figure 4-5: Lorentzian model fit to measured frequency using AFM optics.**

Cantilever frequencies ranged from 21 kHz to 35 kHz for old type devices. After coating devices with CuBTC MOF the fundamental frequencies were measured again. Assuming a constant stiffness (k), a shift of 700 Hz was expected. Due to the difficulty of placing the device in precisely the same spot every time, such measurements proved to

be less reliable than expected (Table 4-1). Some of the frequencies shifted down indicating mass added, while other frequencies shifted up indicating mass reduced.

**Table 4-1: AFM frequency measurements before and after coating with MOF. It was estimated that frequency should be reduced by 700 Hz.**

Device 24	Before MOF	After MOF
Cantilever 4	28863 Hz	25091 Hz
Cantilever 6	27748 Hz	34336 Hz
Cantilever 7	21741 Hz	31007 Hz

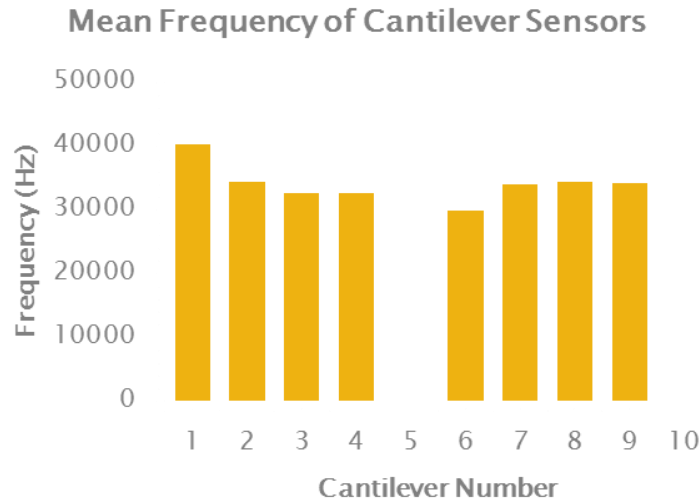


**Figure 4-6: Average values of fundamental frequencies for 10 cantilevers of old type prior to coating.**

To improve measurement quality, a custom laser setup was fabricated. 1mW 625nm wavelength laser diode with a four region sensitive photodiode detector were acquired and a holder was machined (Figure 4-7). ThorLabs lenses and laser control circuits were acquired to ensure constant laser properties. XYZ stage was assembled to aid in positioning of devices under the focused laser beam. DinoLite USB microscope was purchased to aid in positioning of the laser beam onto the microcantilever. A piezodisk was placed underneath the die, and double sided sticky tape was used to couple the die to the disk. LabView program and National Instruments PCIe 6351 DAQ board were used to collect Fast Fourier Transforms (FFT) of the photodiode current. A

function generator in sweep mode excited the piezodisk in frequencies ranging from 100 Hz to 100 kHz. The laser setup successfully detected fundamental frequencies in the same range as the AFM, however, proved as unreliable in mass measurements.

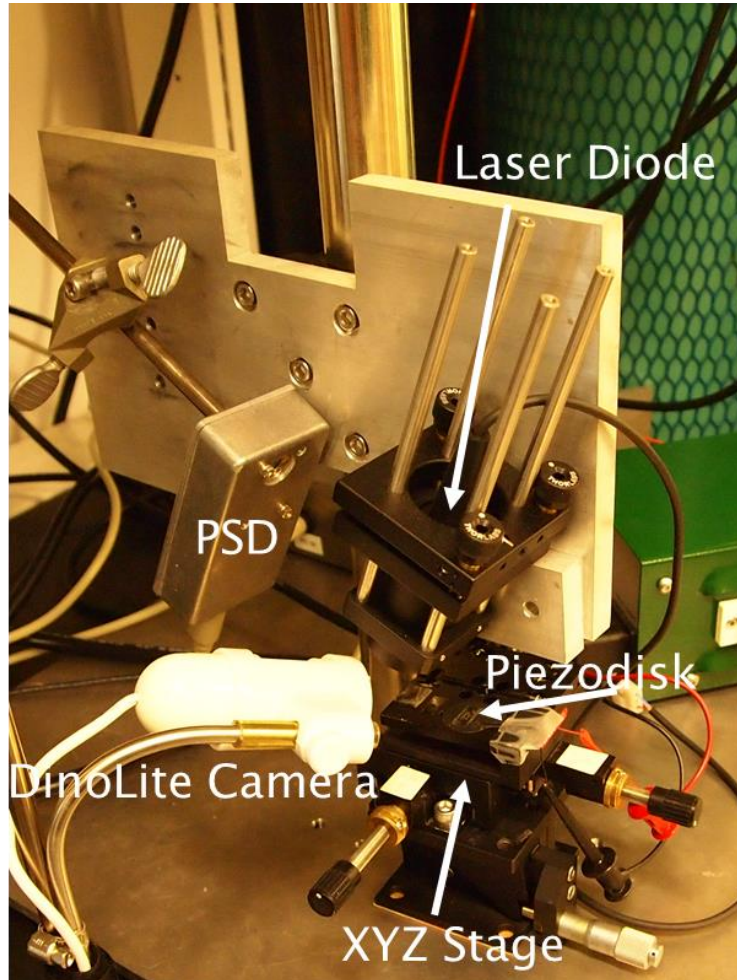


**Figure 4-7: Custom fabricated laser setup.**

Poor reliability of laser measurement setup can be attributed to difficulty in positioning of laser in identical place every time on the cantilever, coupled with differing position on piezodisk. In addition, double sided sticky tape introduces damping of varying degrees depending on cleanliness and age of the tape, further complicating the physics of vibration. Finally, new wider design cantilever exhibit multiple vibrational modes due to their more complex shape. As such, the simple frequency mass relationship

does not apply, and positioning of laser on the cantilever is of even greater importance. Due to above stated obstacles, mass measurements were not routinely used for characterization of new type devices.

### 4.3 Characterization Protocol

#### 4.3.1 Initial Probing and Imaging

Each new wafer contained 187 distinct dies to a total of 827 suspended structures with four resistors on every device. It was therefore necessary to identify which devices are in working order by probing each connection and measuring the resistance and ensuring we know which wafer each device came from. Each wafer was assigned a number during processing, a total of six were processed. Only three wafers had proper stress compensation and therefore were successfully released (#2, #4 and #6). The other three wafers had faulty doping and very few resistors working, thus their loss was not critical (#1, #3 and #5).

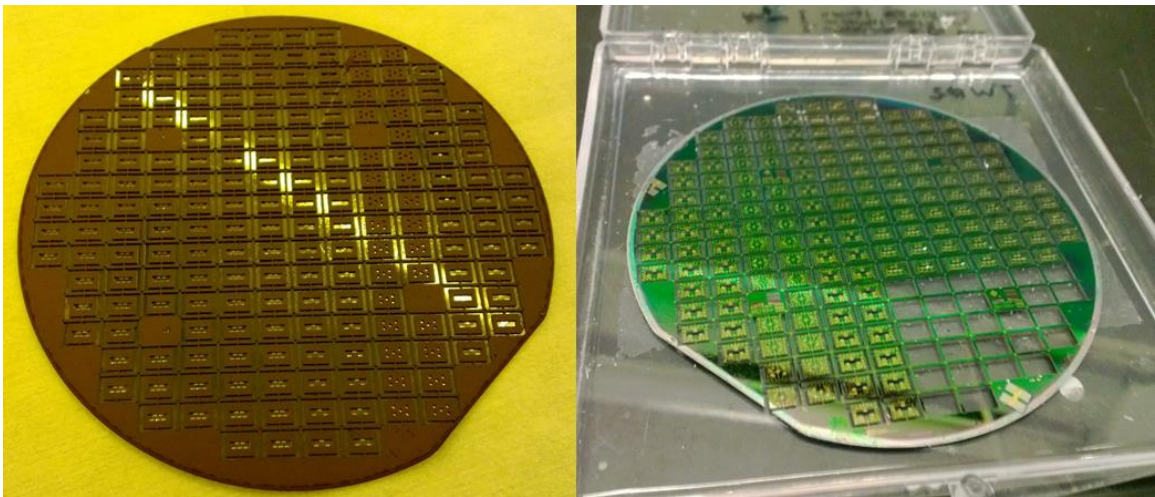


**Figure 4-8: Left - backside view of support grid before separation from carrier. Right - Released wafer with a few missing dies illustrating ease of removal of single dies.**

Dies were designed on a grid, with each die suspended by two 200 $\mu$ m wide pillars that could easily be broken free. Thus, by sliding tweezers under the die and lightly lifting up, the die could be removed from the wafer without the need for dicing, saving

significant amounts of time and improving yield (Figure 4-8). A 4”x 4” box was filled with PDMS, and cured overnight. Process wafers were placed in separate such boxes. The PDMS promoted adhesion between the process wafer and the box. This adhesion ensured that the wafer did not move during die removal. In addition, the slight adhesion between the box and the die during removal reduced the likelihood that a die would fly off (regular occurrence before PDMS lining was practiced). Finally, the wafer was less likely to get damaged during handling since bumping of the wafer against the box sides damaged a number of test wafer grids destroying mock devices in the process.

Upon removal, dies were placed in 1” x 1” boxes lined with PDMS. Each box had a unique barcode to ensure each die could be found from an excel database. The device was probed using a two point probe station (Wentworth Labs Microzoom) seen in Figure 4-9.



**Figure 4-9: Wentworth labs probe station. Capable of probing and taking color images using custom computer software. CREE LED source was fitted to improve image quality and to enable computer control of the light intensity.**

Each resistor's value was initially measured and entered into a master excel datasheet for each wafer. This datasheet contained initial resistances for all the dies on that wafer, as well as the barcode number for each die's storage box. In addition, a unique device folder was created. Each folder was named with a unique serial number for each box which identified the barcode, process wafer, unique die ID and date of initial probing (Figure 4-10).

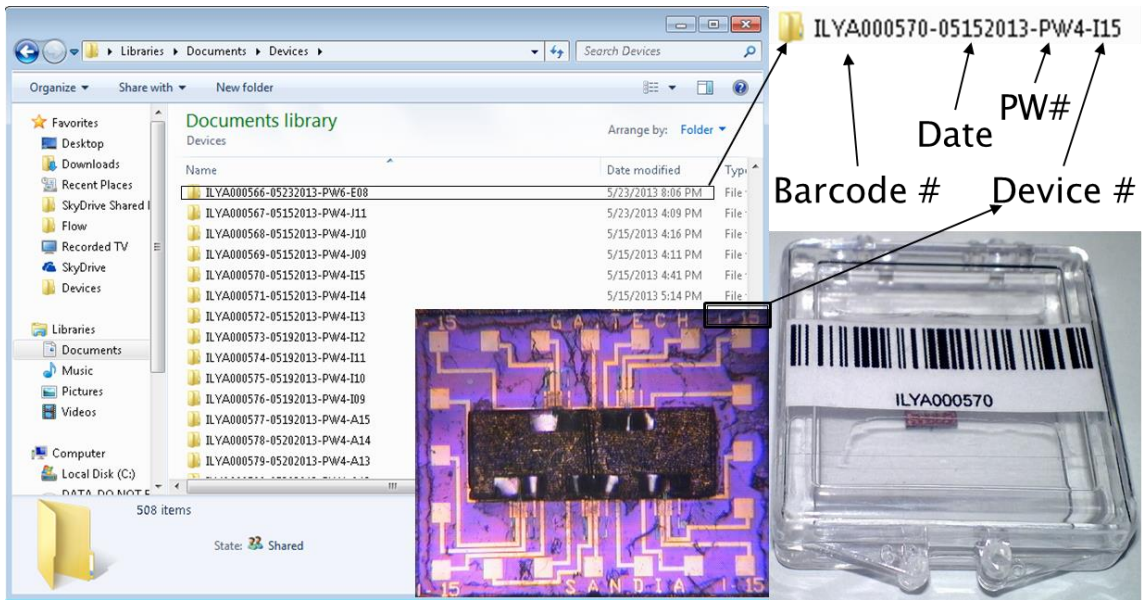


**Figure 4-10: Shows characterization process and serial number explanation. This storage system enabled tracking of each device to a particular location on a particular wafer.**

Inside the die folder, images of each cantilever were stored both before and after coating with selective layers. Frequency measurements were stored in the die folder, with peak measurement data. Any raw data collected for the device would be stored in each die's unique folder. Finally, die folder contained a specification sheet with all resistance measurements throughout the lifetime of the device. Thus, by accessing the unique die folder, it was possible to find all information for each specific die on each wafer.

All the devices on each wafer were subjected to initial probing and imaging. Dies that did not work at all were placed in a special box which contained all nonworking dies from a particular wafer. Upon completing initial probing for the entire wafer, a visual

representation of device yield was used to select dies for further characterization and testing (Figure 4-11). Two yield criteria were developed depending on the requirements of each experiment. For experiments requiring temperature compensation Figure 4-11.B was used to identify dies with complete bridges on the die. Some experiments did not require temperature compensation and therefore Figure 4-11.A could be used for selection. Figure 4-11.A would be used to find dies with two working resistors on the same cantilever, and two external resistors could be connected to complete the bridge for the experiment.

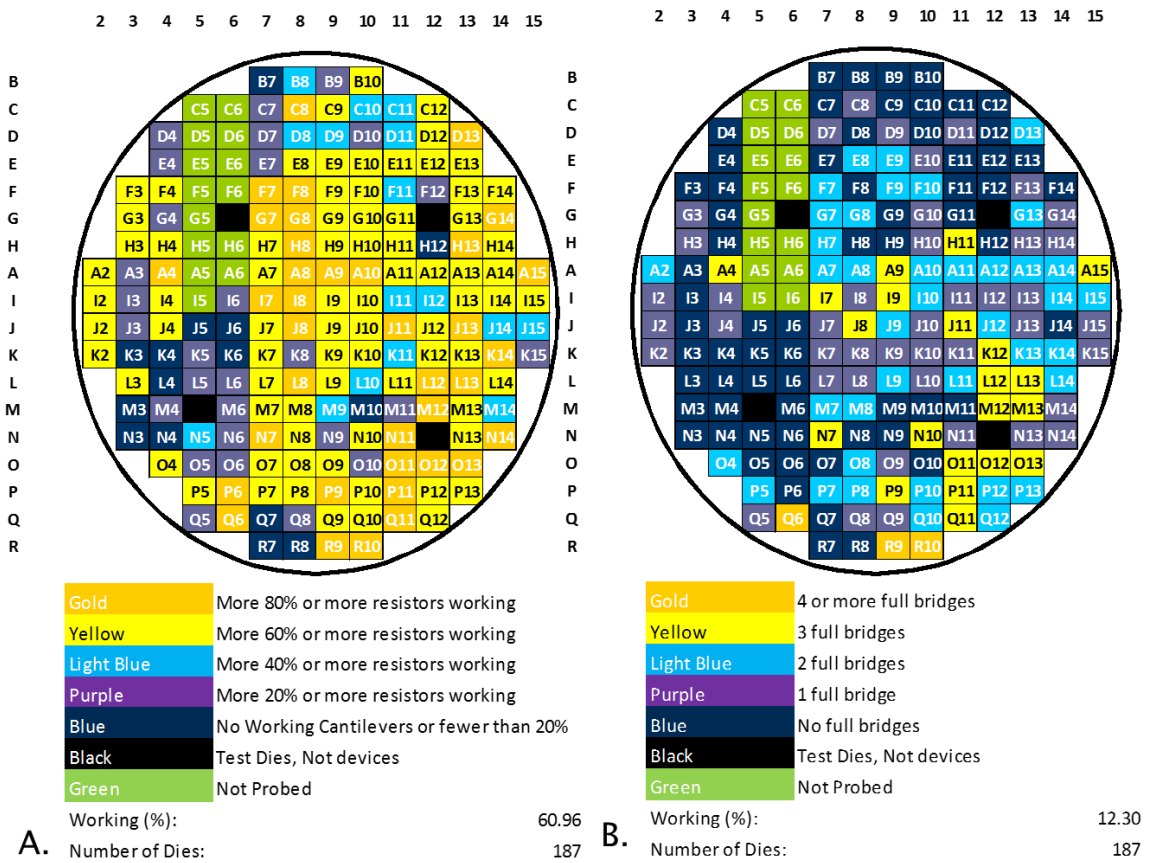


**Figure 4-11: Both images are for process wafer 2. (A) Shows how many working resistors are available on suspended structures. (B) Shows how many complete bridges there are per die.**

### 4.3.2 Metal Organic Frameworks Film Characterization

Upon selecting the target dies, devices were shipped to Sandia National Laboratories in California for MOF coating. Special packaging procedure was developed



### Contact Information

By: Ilya Ellern Package Reference #: ILYA000024 Date: 5/27/2013  
 Phone: 515-450-8235  
 E-mail: [ellern@gatech.edu](mailto:ellern@gatech.edu)

### Included Items

Item Description	Identification Number	Coatings	Comments
Dr. Lee Microcantilever Array	N1 01	1. 103nm of Si3N4 2. 15nm Ti 3. 50nm Au 4. 40 Cycles CuBTC	

### Resistance Charts\*

Cantilever Number	Pre-characterization	Post Nitride/Gold Deposition	Arrival At Sandia	Post MOF Deposition	Arrival at Georgia Tech	Post Testing
1	1920	-	1924	1383	1824	
2	20	-	18.8	19	20	
3	-	-	-	-	-	
4	1938	-	1941	1949	1957	1964
5	1944	-	-	-	-	-
6	1955	-	1963	1970	1976	24
7	1957	-	1961	1957	1961	1971
8	1945	-	1949	1955	1960	
9	1953	-	1957	1963	1968	
10	-	-	-	-	-	

\*Values in this chart are in Ohms.

\*Bent.

### Fundamental Frequency\*

Cantilever Number	Initial Characterization	Post MOF Deposition	Post Testing	Stiffness (k)	Mass Shift (ug)
1	#DIV/0!	#DIV/0!	#DIV/0!	#DIV/0!	#DIV/0!
2	#DIV/0!	#DIV/0!	#DIV/0!	#DIV/0!	#DIV/0!
3	#DIV/0!	#DIV/0!	#DIV/0!	#DIV/0!	#DIV/0!
4	28863.9	25091.0703	#DIV/0!	28.13	-5455453
5	#DIV/0!	25812.9198	#DIV/0!	#DIV/0!	#DIV/0!
6	27748.2	34336.8059	#DIV/0!	5.0053	483069
7	21741.7	31007.3949	#DIV/0!	7.4465	601477
8	21361.5	#DIV/0!	#DIV/0!	19.373	#DIV/0!
9	#DIV/0!	#DIV/0!	#DIV/0!	#DIV/0!	#DIV/0!
10	#DIV/0!	#DIV/0!	#DIV/0!	#DIV/0!	#DIV/0!

\*Values in this chart are in Hz.

### Comments:

**Figure 4-13: Sample characterization sheet maintained for each device throughout its lifetime.**

## CHAPTER 5

### RESPONSE OF METAL ORGANIC FRAMEWORKS ON OLD TYPE CANTILEVERS

#### 5.1 HKUST-1 (CuBTC) Response

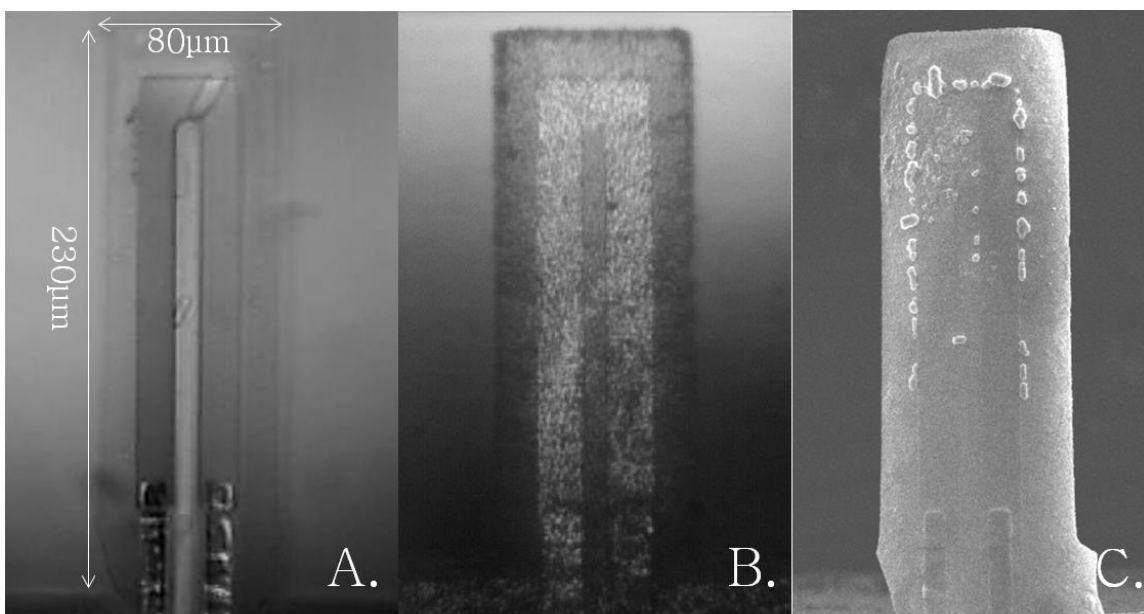
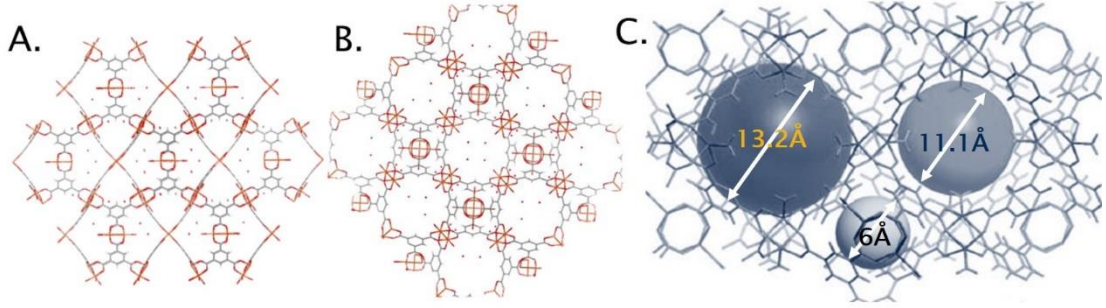


Figure 5-1: (A) Uncoated device (Optical). (B) HKUST-1 coated device (Optical). (C) HKUST-1 coated device (SEM).

##### 5.1.1 Introduction to HKUST-1

HKUST-1, also known as CuBTC, is a highly flexible and porous MOF. Its chemical formula is  $\text{Cu}_3(\text{BTC})_2(\text{H}_2\text{O})_x$ , (BTC = benzene-1,3,5-tricarboxylate), and it consists of a binuclear  $\text{Cu}_2$  paddlewheel unit connected into a 3D structure [27]. The framework contains two distinctive “cages” (13.2 and 11.1 Å in diameter) separated by 9 Å “windows” of square cross section and connected to secondary tetrahedral pockets of 6 Å by 4.6 Å triangular shaped windows (Figure 5-2). HKUST-1 was selected because of its ability to adsorb a number of species [28], high surface area and previously demonstrated suitability to strain based microcantilever sensor [14], [29]. HKUST-1 properties, especially pore size are dependent on synthesis methods and vary from one

laboratory to another [30]. Layer-by-layer growth methods of well controlled thickness and uniformity were developed by the Allendorf group at Sandia National Labs [12] (Figure 5-1).



**Figure 5-2: (A) Mercury model of CuBTC 13.2 Å cage. (B) Mercury model of 11.1 Å cage. (C) Volume of the two cages the smaller pocket [31].**

### 5.1.2 Conversion of Voltage to Resistance

Comparing differential voltage data from the LIA can be used to determine sensitivity of a given device to different analytes. Regrettably, differential voltage from two different devices cannot be compared, since the change in voltage caused by the analyte depends on the initial bridge balance and the settings of range selected on the LIA. Differential voltage data was therefore converted to change in resistance by assuming identical fractional change in resistance for both sensors cantilevers:

$$V_{a-b} = V_{in} \left( \frac{R_2}{R_2 + R_{S2}(1 + \Delta)} - \frac{R_{S1}}{R_1 + R_{S1}(1 + \Delta)} \right)$$

In above equation  $V_{in}$  is the voltage drop across the Wheatstone bridge (Figure 5-3).  $R_1$  and  $R_2$  are the external fixed resistors while  $R_{S1}$  and  $R_{S2}$  are initial resistance values of the microcantilever sensors with the MOF coatings. Both microcantilevers were exposed to the analyte simultaneously, so their fractional change ( $\Delta$ ) was assumed to be identical. Solving the expression for  $\Delta$ :

$$\Delta = \pm \frac{\sqrt{(R_1 R_R V_{a-b})^2 - 2R_1 R_2 R_{S2} R_{S1} (V_{a-b}^2 - 2V_{in}^2) + (R_2 R_{S1} V_{a-b})^2 - R_1 R_{S2} V_{a-b} - R_{S1} [R_2 V_{a-b} + 2R_{S2} (V_{a-b} + V_{in})]}}{2R_{S2} R_{S1} (V_{a-b} + V_{in})}$$

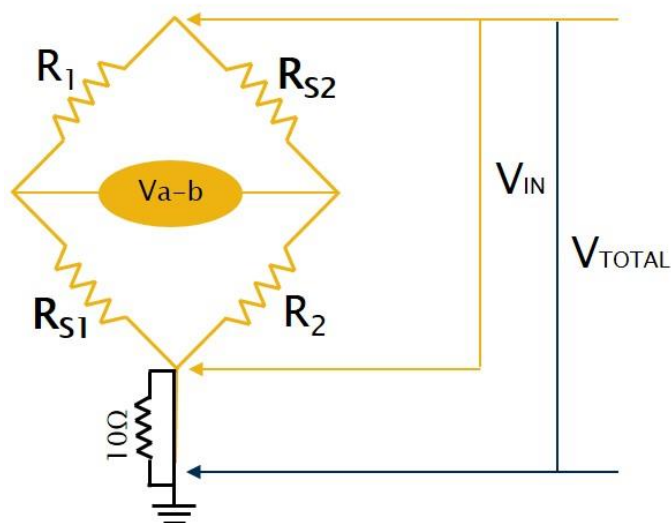


**Figure 5-3: Wheatstone bridge schematic.  $R_{S1}$  and  $R_{S2}$  are microcantilevers while  $R_1$  and  $R_2$  are fixed resistors.  $10\Omega$  resistor is used to measure current in the bridge and may be included or ignored for calculation.**

### 5.1.3 Sample Preparation Procedure

HKUST-1 is inherently hydrophilic [19], due to the polar nature of water it interacts strongly with the adsorption sites. In addition, water's small size relative to the pore limiting diameter ( $4.4 \text{ \AA}$ ) ensures easy entry of guest molecules into adsorption sites. As such, a rigorous dehydration procedure was necessary to ensure the film is free of water prior to exposure. It was shown that heating samples to a temperature of  $180^\circ\text{C}$  at atmospheric pressure in an oven, completely evacuated the pores of the MOF. Experiments conducted with water showed immediate adsorption of humidity into the film upon exposure to atmospheric conditions, it was therefore important to keep dehydrated samples from coming into contact with the humidity in air after dehydration step concluded.

#### 5.1.3.1 Mixed Setup Dehydration Procedure

Mixed setup (Section 2.5) was used for majority of HKUST-1 data published to date with old type devices. Coatings of two types were grown on the surface of old devices. First coating was seeded using SAM OH groups on gold and grown for 40

cycles resulting in a film thickness of 100nm. Second coating was seeded directly on the SiO<sub>2</sub> substrate and grown for 50 cycles for a final thickness of 150nm. During failure analysis of the devices it was determined that cantilever sensors irreversibly deteriorate when heated to 180°C, and that SAM coated devices decouple at roughly 55°C. For these reasons alternative dehydration techniques using the mixed setup were adopted. Further due to lack of sealing capabilities of the old type flow cell, devices could never be truly dehydrated for the experiment.

Devices were placed in the flow cell and heated to 45°C in 100SCCM flow of ultra-high purity nitrogen. With the nitrogen continuously flowing, temperature was turned off, and a flow of nitrogen without analyte exposure was maintained for 10,000 seconds (2.7 hours) until cell and sensor reached room temperature. Remainder of the experiment was conducted with constant flow of at least 100 SCCM of dry nitrogen to reduce likelihood of humidity adsorption.

## **5.2 Response of HKUST-1 to VOCs on Old Type Devices**

### **5.2.1 Measurement of Step Response**

Each analyte was run in two different modes to allow measurement of a number of parameters. First type of measurement entailed systematic increase of analyte concentration every 5,000 seconds (1.38 hours). No dehydration step was performed before changing the concentration, except before the first expose. This exposure resulted in step response (Figure 5-5). This type of experiment was used to acquire the response curves, or isotherms, for each analyte (Figure 5-4). Table 5-1 shows corresponding concentration values in parts per million (ppm).

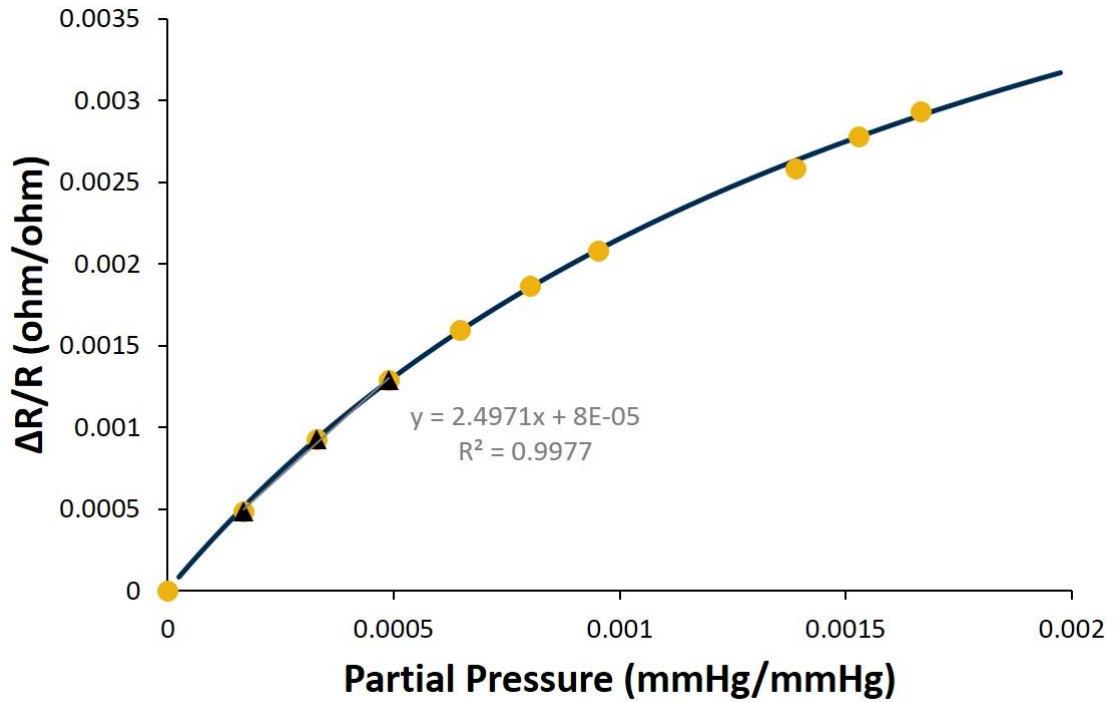


Figure 5-4: Sample isotherm for water response for 40 cycles of CuBTC on SAM.

Models were used to fit data with response parameters. Though many models are available in literature, Langmuir and Henry models were used as initial fit. Henry's model is the simpler of the two and assumes a linear relation for adsorption at a given temperature:

$$C = K_H P$$

Henry's model is generally a good approximation for a narrow range of concentrations when the film is just beginning to adsorb analyte.  $K_H$  is the Henry's constant which characterizes the rate of change of response with respect to increase in concentration. By comparing Henry's constants of different analytes, it is possible to quantify rates of adsorption. Determination of Henry's constant was achieved by fitting least squares fit to the data points in the linear region of the plot.

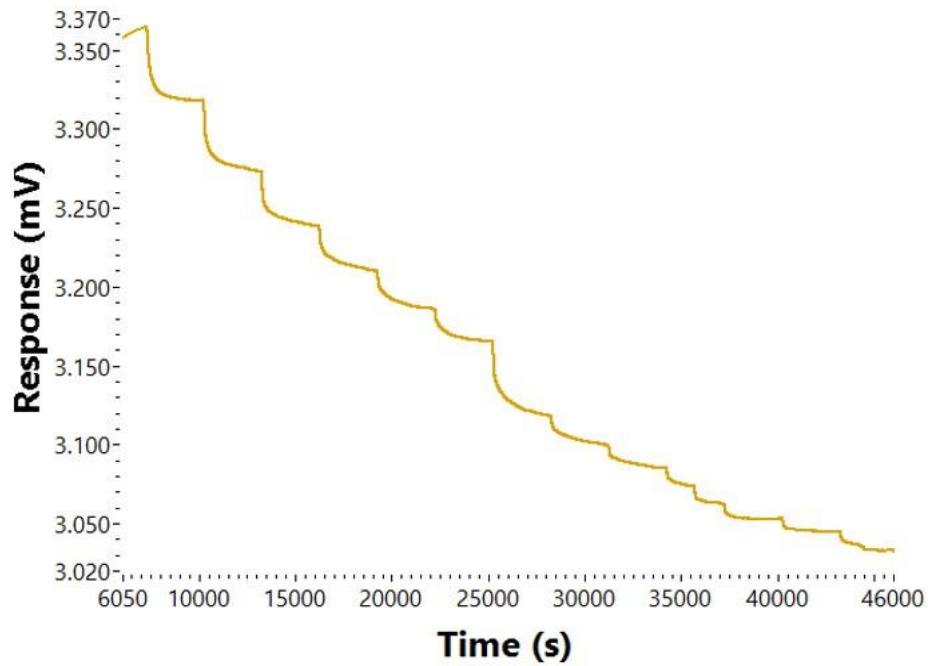


Figure 5-5: Raw data step response of 40 cycles CuBTC on SAM to water.

Table 5-1: Concentration to partial pressure conversion chart.

Concentration (ppm)	Partial Pressure (mmHg/mmHg)
165	0.000166482
330	0.0003297
490	0.000489749
645	0.000646719
800	0.0008007
950	0.000951776
1380	0.00138837
1520	0.001528609
1660	0.001666322

Langmuir model assumes equal adsorption sites and a homogeneous film.

Further, it assumes a single molecule adsorbed per site and no interaction of molecules with each other. No competitive adsorption of different species is accounted by the Langmuir model:

$$C = \frac{C_H \alpha P}{1 + \alpha P}$$

Langmuir model was applicable to acquired data due to single analyte exposure of the MOF in the experimental setup. Nitrogen, was used due to its inert properties with respect to the MOF, thus it did not pose threat of competitive adsorption with the analyte of interest. Numerical methods were used to identify parameters  $C_H$  (adsorption capacity of monolayer) and  $\alpha$  (Langmuir's adsorption constant). Initial guesses for  $C_H$  and  $\alpha$  were supplied, and a program varied the parameters until error<sup>2</sup> reached a predefined accuracy threshold (mean square error of  $4.25 \times 10^{-10} (\Delta R/R)^2$ ). Fit was plotted against data (Figure 5-4) and visually confirmed.

### 5.2.2 Measurement of Mixed Response

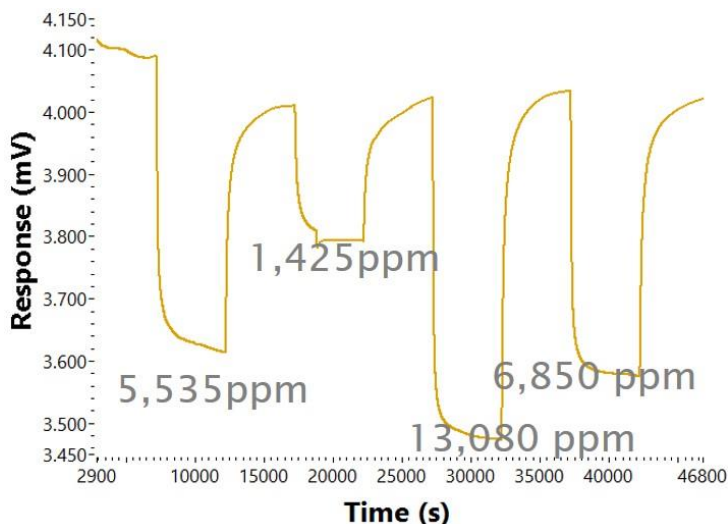


Figure 5-6: Mixed response of 40 cycles CuBTC on SAM to methanol vapor.

To determine reversibility of response as well as response time constants, a mixed response experiment was conducted. Dehydration step was performed as described in Section 5.1.3.1. MOF was subsequently exposed to varying concentrations of analyte for 10,000 seconds (2.7 hours), separated by a 10,000 second purge step (Figure 5-6).

**Table 5-2: Sample mixing flows and resulting concentrations for mixed water test.**

Hydrator Flow Rate (SCCM)	Purge Line Flow Rate (SCCM)	Concentration (PPM)
20	5	13395
20	50	4785
20	20	8370
20	40	5580
20	30	6700
20	10	11160
5	100	800
20	100	2790

Although mixing ratios for each experiment were the same, the resulting concentrations varied depending on the temperature of the analyte and the analyte's properties. In order to calculate the concentration, vapor pressure calculations were performed using three models (Table 5-3). Model was determined by analyte type as listed in reference [32] and the equation was used to calculate the vapor pressure at a given temperature. Atmospheric pressure was assumed to be 760 mmHg and the relative humidity was assumed to be 85% inside the humidifier.

**Table 5-3: Vapor pressure models [32].**

Eq.	Vapor-pressure equation
1	$\log p = A - \frac{B}{t + C}$
2	$\log p = A - \frac{B}{T}$
3	$\log p = A - \frac{B}{T} - C \log T$

Using above relations to determine the vapor pressure and molar fraction ( $x_i$ ) of analyte, concentration (C) can be calculated as follows:

$$C = x_i(10^6) \frac{v_{hydrator}}{v_{hydrator} + v_{purge}}$$

In above equation  $v_{hydrator}$  (SCCM) is the mass flow rate through hydrator and  $v_{purge}$  is the mass flow rate through the purge line (SCCM).

Adsorption time constant was calculated by waiting for saturation of response to a given concentration and calculating the time it took to reach 63.2% of response (Figure 5-6, Figure 5-8 and Figure 5-9).

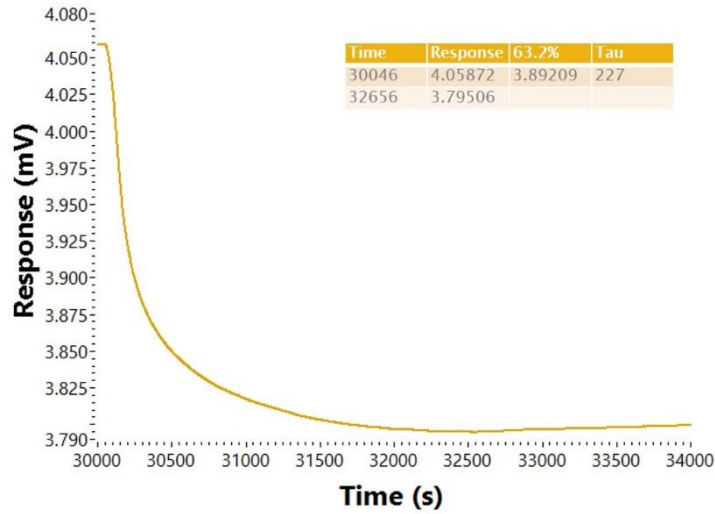


Figure 5-7: Sample time constant calculation using methanol response with CuBTC on SAM.

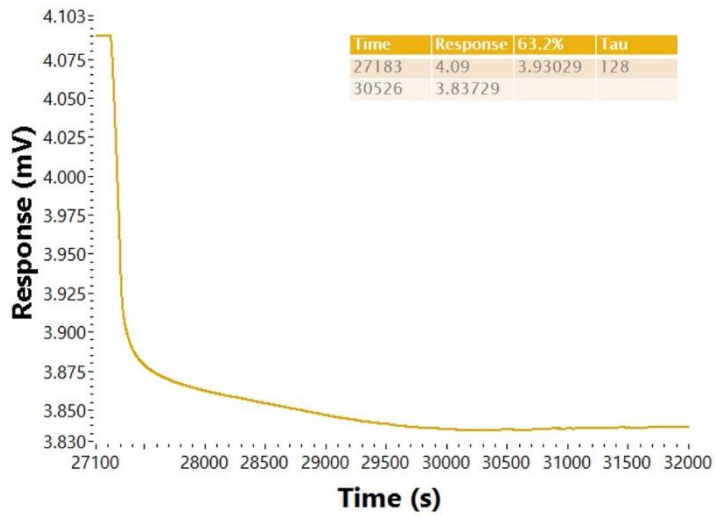
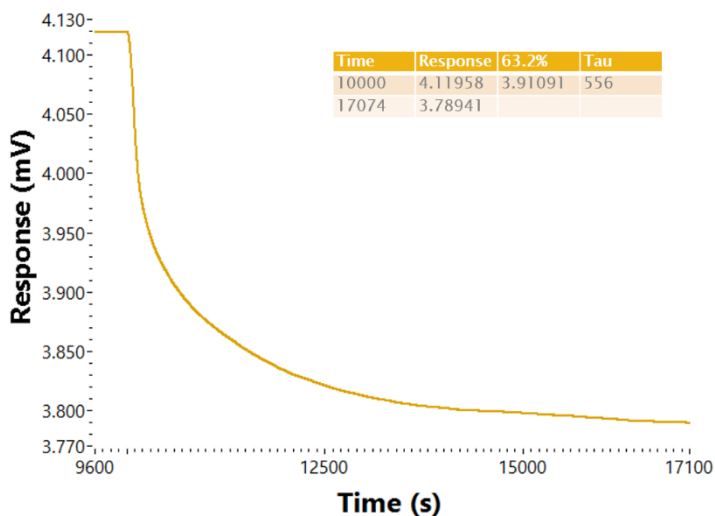


Figure 5-8: Sample time constant calculation using water response with CuBTC on SAM.



**Figure 5-9: Sample time constant calculation using ethanol response with CuBTC on SAM.**

### 5.3 Adsorption Results

Figures below will show and discuss the data for the nine analytes where response was observed (see APPENDIX C for plots side by side). Analytes without response are not represented since the response appears simply as equipment noise. Tests were repeated multiple times even on devices that did not show response to confirm results. At least five experiments with each of the twelve analytes were performed on different dates months apart. The best data sets were selected for figures below, however, thermally induced drift is present in some measurements.

## 5.4 Discussion

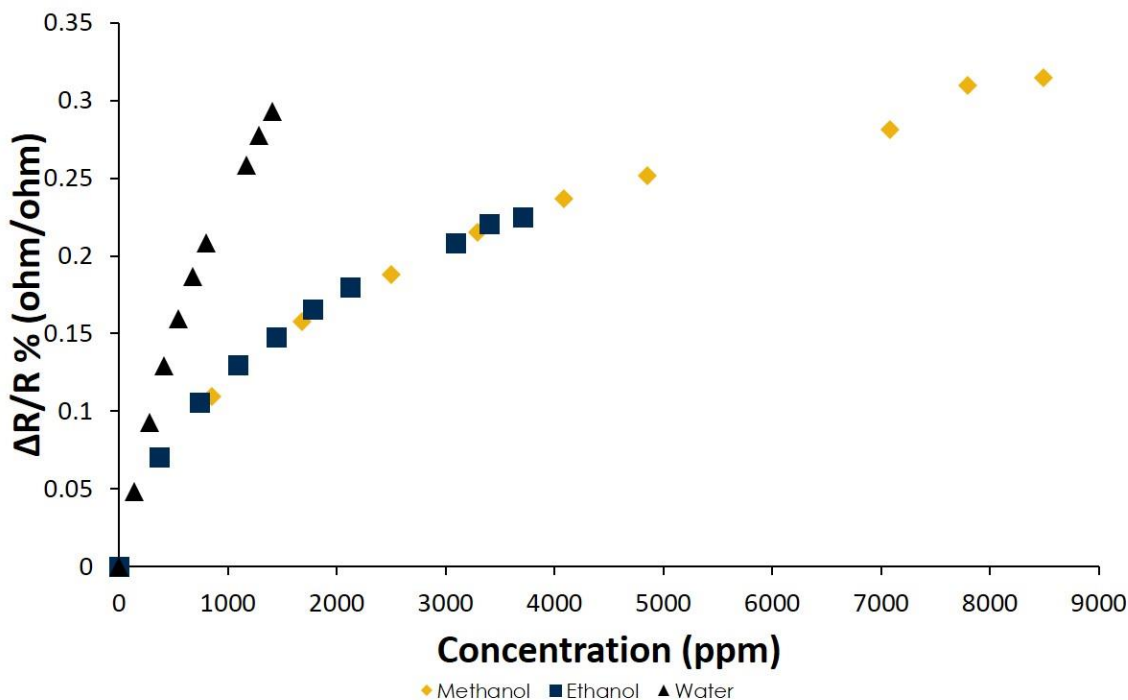
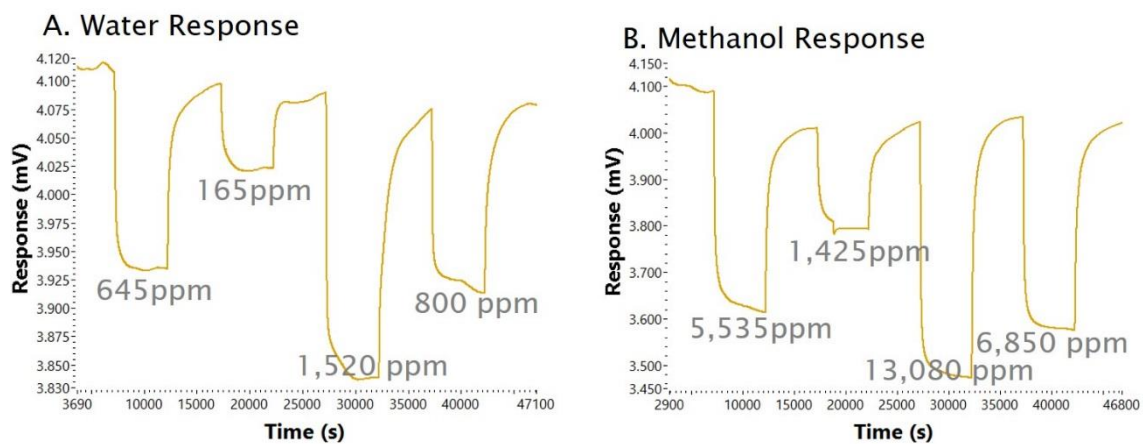


Figure 5-10: Response of alcohols and water on 40 cycles of CuBTC on SAM.

All twelve analytes in Table 5-8 were tested to determine their response properties. HKUST-1 exhibited strong response to water due to small size of the molecule compared to limiting pore diameter as well as large dipole moment of the molecule. Alcohols also induced large strains in the MOF causing significant response, though interaction was not as strong for a given concentration compared to water (Figure 5-10, Figure 5-13). Difference in response may be attributed to a reduced dipole moment as well as larger kinetic diameters of the alcohols, contributing to less interaction with the adsorption sites. It also may be caused by reduced packing efficiency of the larger molecules inside the pores. Relative strength of water vs. alcohols was independent of substrate and MOF thickness as can be observed by comparing relative strength for two different sensors in Figure 5-10 and Figure 5-13. Data which proved to be most reversible was for water and methanol (Figure 5-11).



**Figure 5-11: Response of 40 cycles of CuBTC on SAM. (A) Response to varying concentrations of water. (B) Response to varying concentrations of methanol. Response of these analytes had a good degree of reversibility.**

Acetone response was observed to be similar to isopropanol response (Figure 5-13). Possibly, due to similar kinetic diameters though dipole moment of acetone is two times the dipole moment of isopropanol. Isopropanol and ethanol did not exhibit high degree of reversibility observed with water and methanol (Figure 5-12).

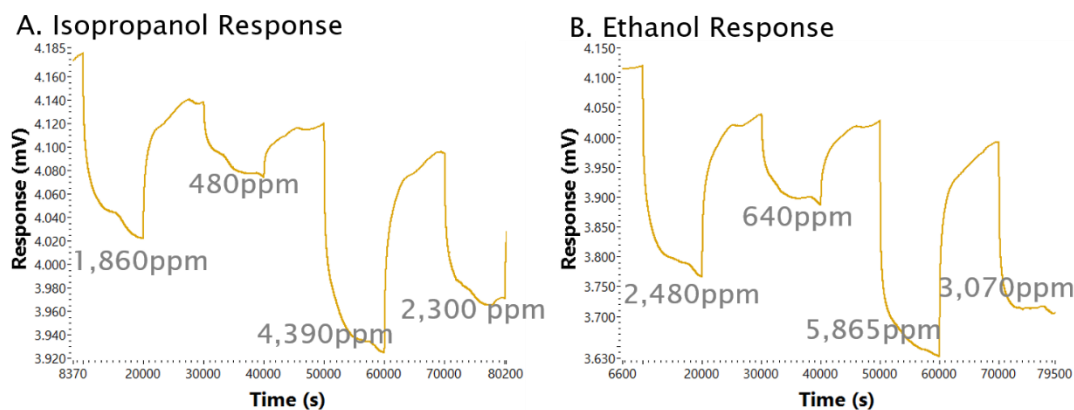


**Figure 5-12: Response of 40 cycles of CuBTC on SAM. (A) Response to varying concentrations of isopropanol. (B) Response to varying concentrations of ethanol.**

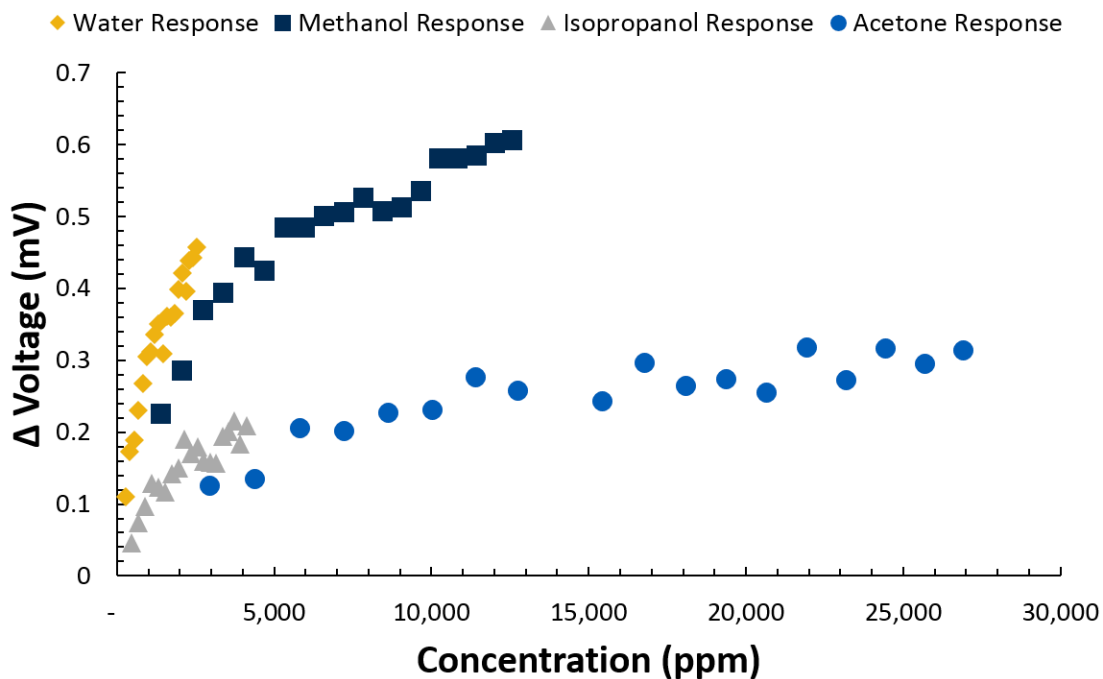


Figure 5-13: Response of 50 cycles CuBTC on SiO<sub>2</sub> for alcohols compared to water and acetone [25] isotherms from mixed response data in random order similar to Table 5-2.

Acetone and chloroform both show characteristic response shapes. Acetone exhibited very slow adsorption and desorption characteristics (Figure 5-14.A). Chloroform, on the other hand, was observed to respond rapidly to adsorption, however, slowly to desorption (Figure 5-14.B).

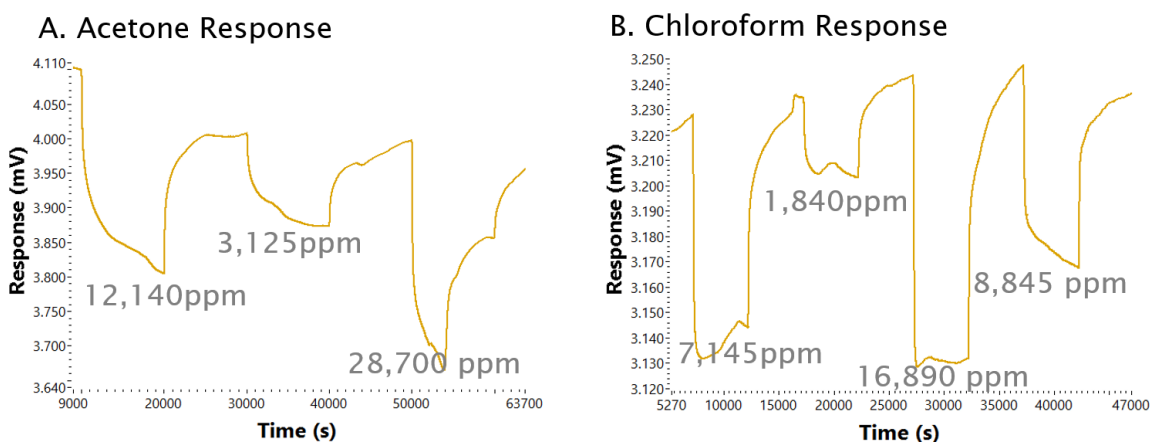
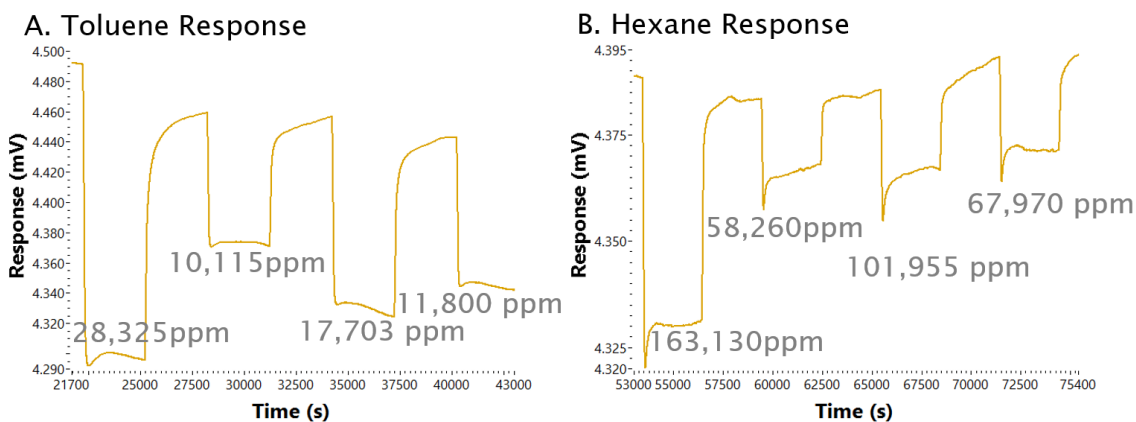
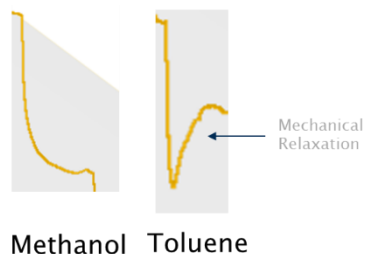


Figure 5-14: Data for 40 cycles of CuBTC on SAM. (A) Acetone was characterized by slow adsorption and desorption curves. (B) Chloroform was characterized by rapid adsorption but slow desorption.

Toluene and hexane exhibited a degree of mechanical relaxation. Despite mechanical relaxation, toluene response did not appear to saturate overtime, with stronger response peaks at later exposures continuing to generate more strain than weaker concentrations at earlier stages. Hexane's response, however, reduced in strength over time, suggesting saturation of response.



**Figure 5-15: Data for 40 cycles of CuBTC on SAM. (A) Mechanical relaxation in the case of toluene did not saturate response over time. (B) Hexane saturated over time.**



**Figure 5-16: Some analytes exhibited unique adsorption features making time constant calculations difficult.**

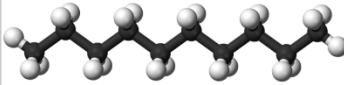
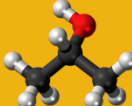
Time constants were calculated (Table 5-4) for analytes where response was smooth without unique features (Figure 5-16). Some analytes such as hexane and decane rapidly saturated and required heating for desorption, making acquisition of data for isotherms and time constants unreliable. These analytes typically had larger kinetic diameters, no dipole moments and physically were long chains (Table 5-5). Analytes that exhibited good reversibility without heat were typically smaller molecules with compact geometry.

**Table 5-4: Calculated time constants for HKUST-1 based on CuBTC on SAM response.**

Analyte	Adsorption $\tau$ (s)	Concentration (ppm)
Water	128	1540
Chloroform	162	1560
Methanol	227	1210
Ethanol	556	2110
Isopropanol	562	1580
Acetone	1242	2660

Adsorption is a complicated phenomenon which is not well understood, thus above generalizations are not rules. For example, toluene and isopropanol are not compact molecules, however, response to these analytes was observed and was reversible without heating, on par with smaller molecules. Similarly, carbon dioxide, is a small molecule which may easily fit through the pore, but no response was observed. Moreover, CO<sub>2</sub> adsorption into HKUST-1 is well documented [33], [34], [30], [35]. Table 5-5 groups response of analytes into four distinct categories based on mixed concentration exposure, summarizing results presented thus far.

**Table 5-5: Physical attributes of analytes grouped by quality of response data.**

	Hexamethyldisiloxane	1,2 Dichloroethane	Carbon Dioxide					
NO RESPONSE								
IRREVERSIBLE		Decane 		Hexane 				
POOR REVERSABILITY	Toluene 	Isopropanol 	Ethanol 	Acetone 	Chloroform 			
REVERSIBLE	Methanol 	Water 						

Lack of response to CO<sub>2</sub> may be explained by a number of hypothesis. Due to difficulty of achieving complete dehydration with the mixed cantilever setup, the sites that CO<sub>2</sub> binds to could be occupied with water molecules [35]. It is possible that with complete dehydration of the film, response to CO<sub>2</sub> will be observed. Likewise, adsorption and binding of CO<sub>2</sub> to pores may not generate very much surface strain in the film, resulting in no response. CO<sub>2</sub> and water, though of similar geometries, size and shapes have drastically different dipole moments. Perhaps the polarity of water helps induce strain during adsorption, while the lack of the dipole moment in CO<sub>2</sub> results in no strain despite adsorption.

In spite of failing to completely remove water from the pores, the dehydration procedure in section 5.1.3.1 was successful at desorbing all analytes and regenerating the film. At elevated temperatures the pores of the flexible MOF structure expand increasing the limiting pore diameter increasing diffusion out of the pore. To further aid desorption, constant nitrogen flow was maintained during cooling of the setup prior to subsequent experiments.

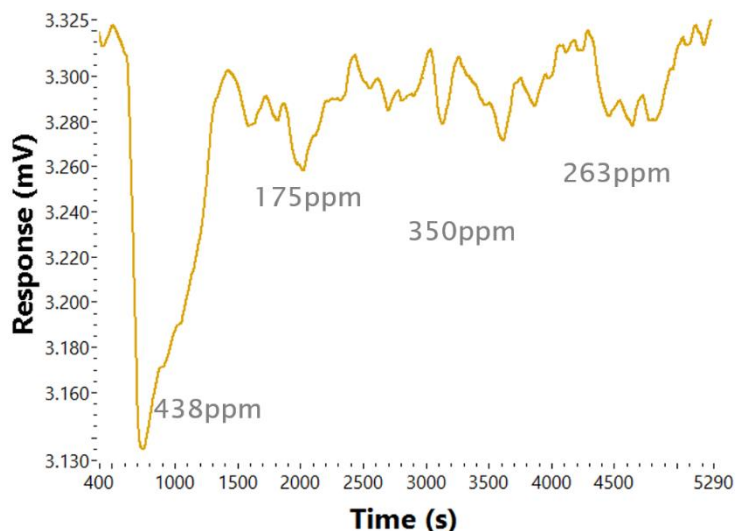


**Figure 5-17: Decane response of CuBTC on SAM.**

Decane response exhibited a unique characteristic (Figure 5-17). Only a single exposure of HKUST-1 was possible, since saturation would occur. The response resulted in a single peak followed by a rapid relaxation of strain back to the original baseline. Further exposures to higher concentrations did not exhibit any additional strain response. Toluene and chloroform showed a degree of mechanical relaxation which also complicated computation of time constants (Figure 5-16). Possible explanation may lie in sieving effects of the MOF structure.

Decane is a long hydrocarbon chain, similar in cross-sectional size to hexane (roughly 6Å kinetic diameter) but substantially longer. Steric effects may lodge these long chains at the pore limiting diameter upon exposure. Strain could be generated initially, as pore openings still remain in the film, however, upon all pore openings becoming clogged by the decane molecules, mechanical relaxation occurs returning the film to original condition. Subsequent exposures have no effect on the film due to all pore openings being occupied by decane. As temperature is increased, expansion of the MOF pore combined with increased vibration of decane molecules dislodge the analyte from the MOF. The previous statement is supported by the observation that upon

dehydration of the film using procedure in section 5.1.3.1, film would be returned to original condition.

Hexane, another hydrocarbon shorter than decane, saturated at a much slower rate, however, some degree of desorption was observed. Nevertheless, increasing concentration of analyte in subsequent exposures did not result in stronger, but weaker response. A similar hypothesis as discussed in the previous paragraph may explain this phenomena with the exception that not all sites become blocked by the analyte allowing some subsequent adsorption to occur.

### **5.5 Response of Mixtures of Analytes**

Analyte mixture testing is of interest since most environments contain mixtures of different gases. Experiments were conducted with water vapor since it is likely to be present in the environment for most applications. Two hydrators in the mixed experimental setup (section 2.5) were used. A water concentration was maintained with one hydrator, while the other hydrator cycled toluene pulses. Toluene response was detected despite water background, suggesting that detection of analytes in humid environments is possible without dehydration of the MOF prior to testing. Water response in a toluene background was also tested and yielded results.

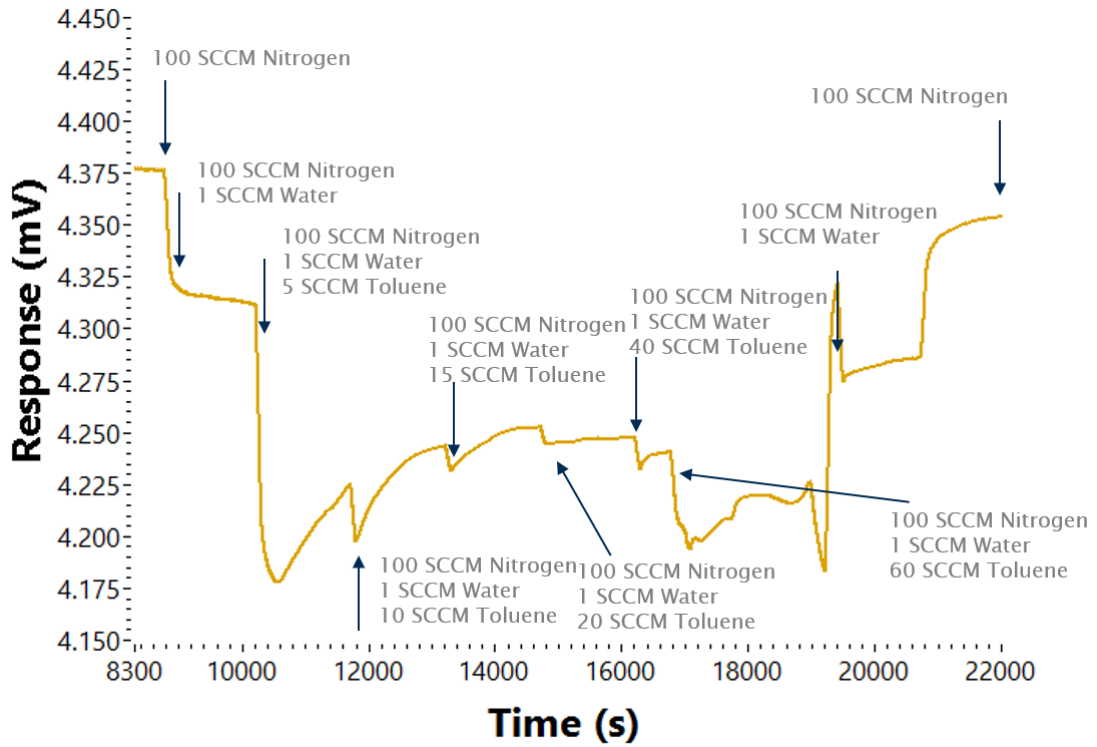


Figure 5-18: Toluene response in water background was demonstrated.

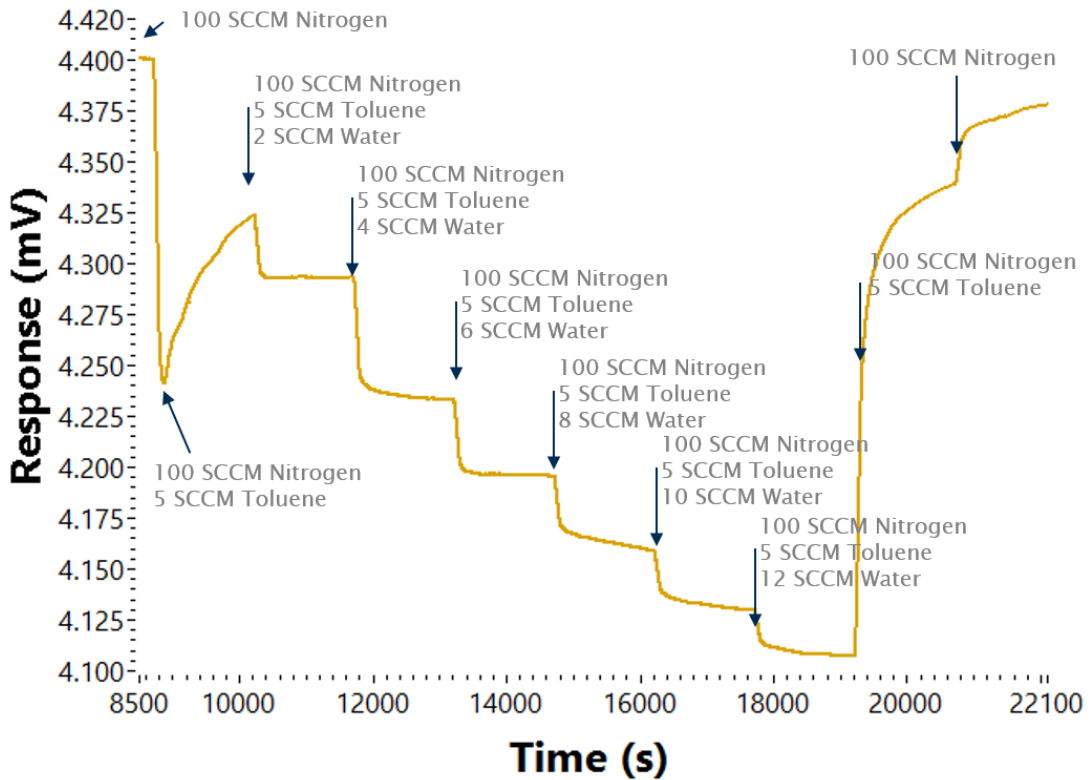


Figure 5-19: Water concentrations were detected in a toluene background.

## **5.6 Reliability and Stability of MOF Coated Microcantilevers**

A successful sensor must be selective, respond to a wide range of analytes, have excellent sensitivity, and be reliable over the long term. Previous sections of this chapter covered selectivity and wide range of response to different analytes. This section will discuss long term performance of the devices as well as limit of detection estimates.

### **5.6.1 Reliability and Precision**

The first successfully coated device was 40 cycles (100nm) of HKUST-1 with SAM on gold. Experiments have been carried out on the device for over 18 months. Device was subject to 170 different experiments involving 12 different analytes at temperatures ranging from 15°C to 45°C. Mass flow rates varied from 100 SCCM to 10,000 SCCM. Periodically, water exposure was performed on the device to ensure device functionality (Figure 5-20). Device performance was unaffected despite exposure to different analytes, suggesting both the piezoresistive cantilever and HKUST-1 MOF coating are reliable in the long term. Overlap of different data sets collected over a range of dates suggested precision of the device and its ability to provide reproducible results.

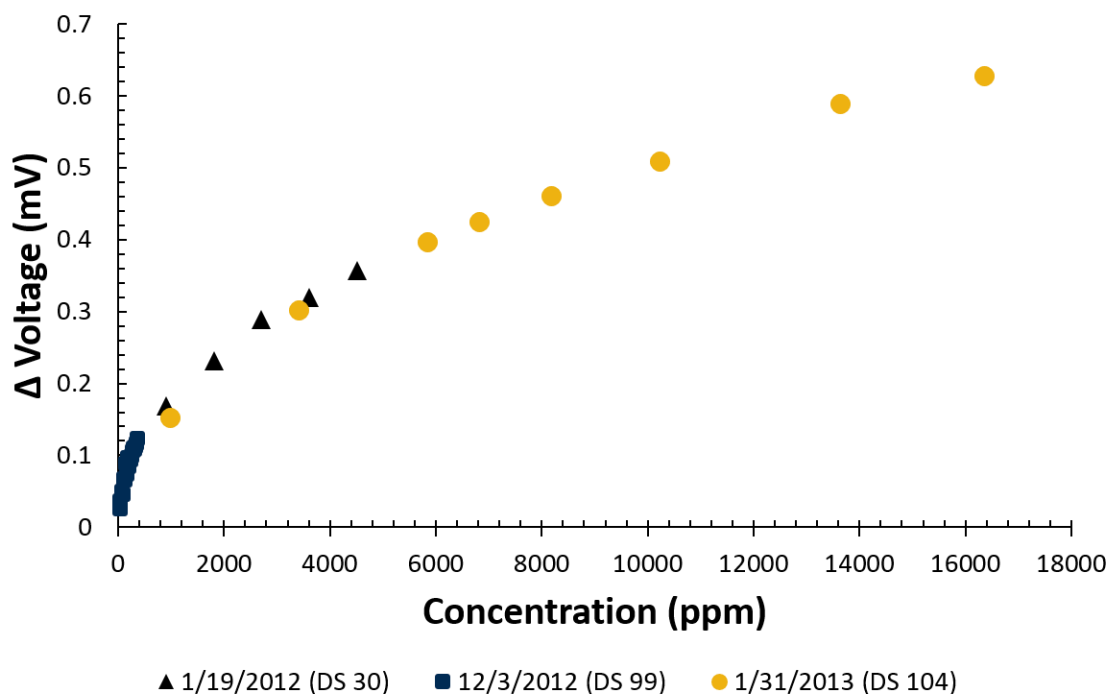


**Figure 5-20: Water response on CuBTC coated device over 12 months of testing.**

Response of the cantilever device was compared with a commercial capacitance based sensor (Measurement Specialties HM1500) at high concentrations of water (Figure 5-21). Both devices responded to changing humidity levels. Concentrations varied from 1735ppm – 5780ppm. Humidity detector readings ranged from 2100ppm - 6330ppm. The response rate of both devices was comparable, however, the capacitance based sensor could not be exposed to volatile organic compounds as per manufacturer specification sheet. Figure 5-21.B data suggest the relative humidity during evacuation of the cell is not zero. Despite the possibility that the cell was not hermetic and allowed some humidity to penetrate the flow, the 2% relative humidity read by the humidity sensor was most likely device error. According to manufacturer specification sheet the accuracy of the device was +/- 3%RH. Figure 5-21 suggests both operational integrity of the experimental setup and the operational reliability of the MOF coated cantilever as a humidity sensor. HM1500's PPM readings were within margin of error with the vapor pressure calculated values.

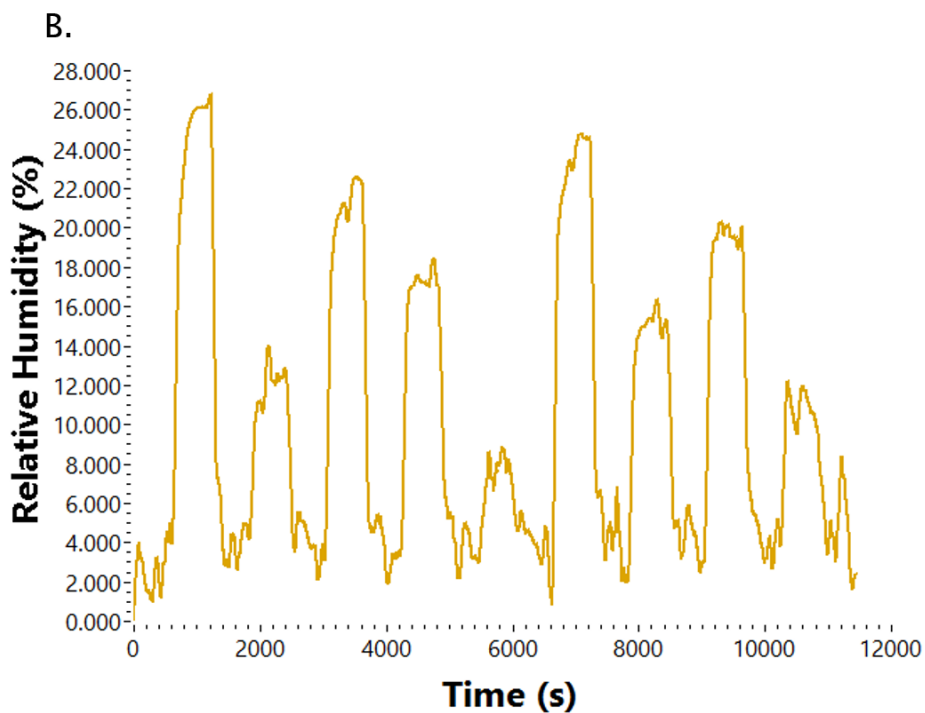
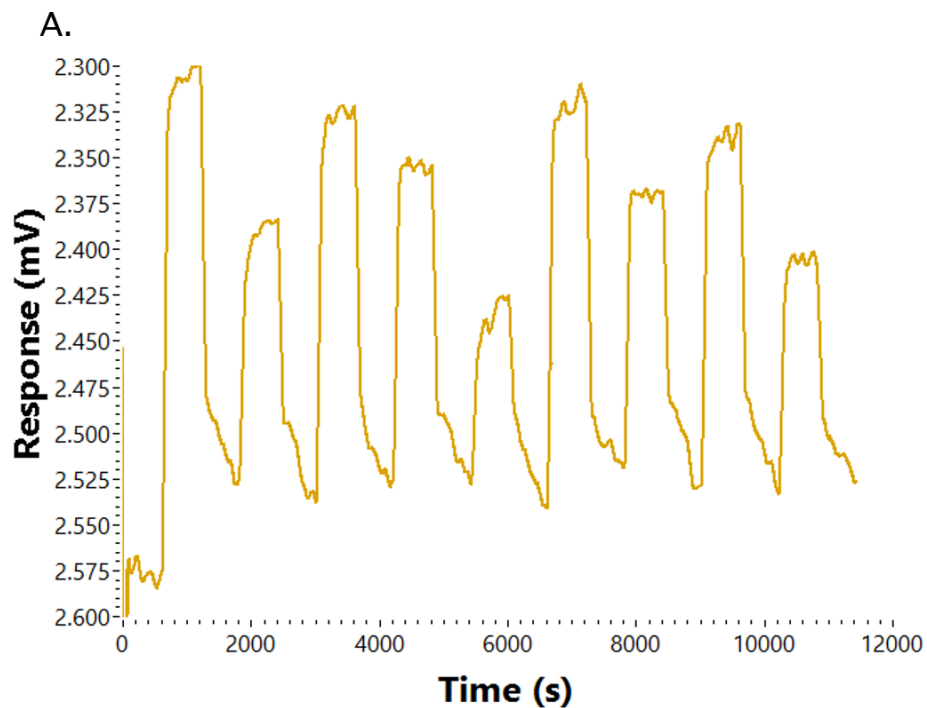


**Figure 5-21: (A) Response of HKUST-1 coated microcantilever with 40 cycles on SAM @ 22°C. (B) Response of HM1500 humidity sensor by Measurements Specialties Inc. Concentrations varied from 1735ppm – 5780ppm. Humidity detector readings ranged from 2100ppm - 6330ppm.**

## 5.7 Sensitivity and Limits of Detection

Sensitivity of the device depends on the analyte, layer composition of the cantilever as well as the MOF coating thickness. Langmuir isotherm fit was used to quantify relative sensitivity of the device to different analytes via the  $C_H$  and  $\alpha$  constants (Table 5-6). High  $C_H$  values suggest a higher adsorption capacity for the analyte. Moreover, a large Henry's constant suggested more rapid affinity for adsorption in response to a given concentration of analyte. Thus from Table 5-6 it may be concluded that many adsorption sites were still available for the water, and the MOF was not filled to capacity. Similarly, it may be concluded that ethanol filled more adsorption sites than both methanol and water. Based on the Henry's constant, best sensitivity was achieved for water vapor, followed by methanol and closely trailed by ethanol. These observations can be visually confirmed by referring to Figure 5-10.

**Table 5-6:  $C_H$  and  $\alpha$  values of alcohols compared to water.**

Analyte	$\alpha$	$C_H$	Henry's Constant
Water	.006	540	2.50
Methanol	.004	223	.89
Ethanol	.003	99	.79

Limits of detection were estimated by applying Henry's model to a few points in the linear region of the response curve, and multiplying the Henry's constant by the noise of the equipment. Although this method proved useful in predicting future benchmarks for concentration reduction, it was too conservative. Initial estimates for water suggested a limit of detection of 167 ppm, however, upon lowering the concentration of the analyte experimentally a measured value of 6 ppm was acquired. This trend can be observed in Table 5-7, where new estimates were calculated based on data from different concentration ranges. Based on latest measurements the limit of detection for water was estimated as 3 ppm. It is possible that actual limit of detection is in the high ppb range. Conservative limits of detection for ethanol and methanol are in the 10's of ppm.

Sensitivity to water was better than for any other analyte. High  $C_H$  values suggest that many sites remain unoccupied by the analyte, allowing for detection of higher concentration of water. Compared to the commercial capacitive humidity sensor, MOF coated microcantilevers provide a large dynamic range of response with capability to measure a few ppm to tens of thousands of ppm with high resolution. Sensitivity decreases at higher concentrations and is highest at lower concentrations.

**Table 5-7: Measured data in certain PPM ranges can be used to estimate limits of detection. Such estimates were not very reliable.**

Concentration Range (PPM)	LOD Estimate Conservative (10 $\mu$ V noise assumed)	LOD Estimate Optimistic (2 $\mu$ V noise assumed)
6815–16,355	167 ppm	33 ppm
902–4,511	100 ppm	20 ppm
40–370	16 ppm	3 ppm

### 5.8 Low Power Operation

A key benefit of piezoresistive microcantilevers is simple instrumentation for measurement of response, paving the road to highly portable, low power sensors. All experiments were run with 200mV of supplied potential at 3000Hz. Low power was delivered to the circuit to ensure the piezoresistors do not heat up during operation. An additional reason for using low power, was to demonstrate viability of operating the device with small batteries. Current in the circuit was measured to be 60 $\mu$ A, corresponding to a power input of 12 $\mu$ W per Wheatstone bridge. By selecting low power lock-in amplifier chips and multiplexer chips it is viable to create a battery powered gas detection system.

### 5.9 Summary of Results

Twelve analytes were selected, with a wide range of kinetic diameters, properties and shapes (Table 5-8). Samples were degased using procedure outlined in Section

5.1.3.1. Regular analytes were used, some with inherent water content (ethanol is hydrophilic). Experimental setup was as described in Section 2.5.

**Table 5-8: Summary of analyte properties and response.**

Analyte	Response	Reversibility Without Heat	Reversibility With Heat	Kinetic Diameter (Å)	Dipole Moment (D)	Molar Mass (g/mol)
Water	Yes	Good	Yes	2.65	1.85	18
Ethanol	Yes	Poor	Yes	4.5	1.7	46.07
Methanol	Yes	Good	Yes	3.8	1.7	32.04
Isopropanol	Yes	Poor	Yes	4.7	1.7	60.1
Toluene	Yes	Poor	Yes	5.8	0.36	92.14
Acetone	Yes	Poor	Yes	4.7	2.9	58.08
Chloroform	Yes	Poor	Yes	4	1	119.38
Hexane	Yes	No	Yes	6	0	86.18
Decane	Yes	No	Yes	-	0	142.28
Carbon Dioxide	No	N/A	N/A	3	0	44
1,2 Dichloroethane	No	N/A	N/A	-	1.8	98.96
Hexamethyldisiloxane	No	N/A	N/A	-	1.1	162.38

# CHAPTER 6 RESPONSE OF METAL ORGANIC FRAMEWORKS ON NEW TYPE DEVICES

Microcantilever sensors were fabricated as described in section 3.2. Modeling results suggested wider designs will deliver lower limits of detection and improved response [21]. Devices were characterized as described in section 4.3. Experiments were performed to investigate response strength, noise of device and compare results to old type microcantilevers.

## 6.1 Comparison of Noise Levels

Four identical  $\frac{1}{4}$  watt fixed resistors arranged in a Wheatstone bridge were connected to the experimental equipment (section 2.2.2). 200mV at 3000Hz were delivered to the circuit and the differential voltage across nodes A and B was measured for 10 minutes. Experiment was conducted at room temperature of 23.6°C and atmospheric pressure (Figure 6-1). Magnitude of measured noise oscillations was roughly 1.3 $\mu$ V peak to peak.

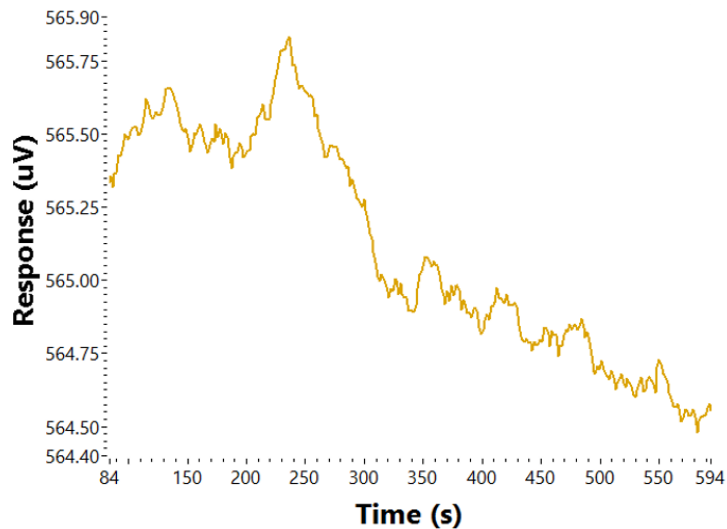
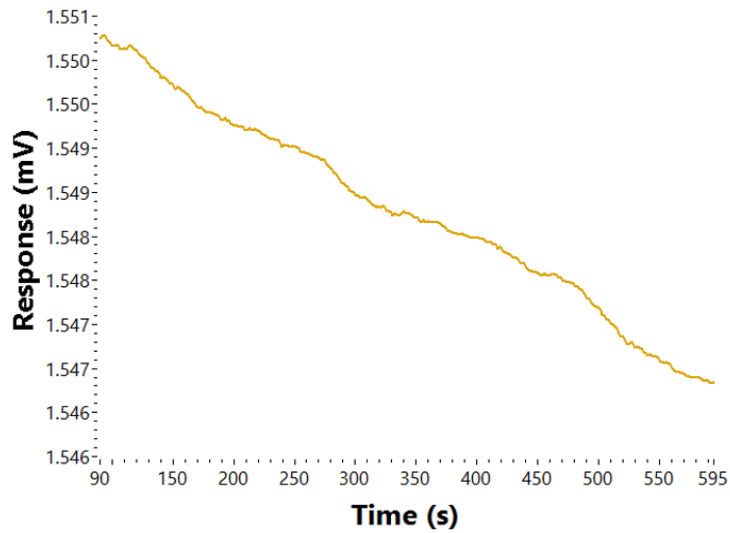


Figure 6-1: Ambient noise of four identical fixed resistors.

Experiment was repeated by replacing one of the fixed resistors with the old type microcantilever with no film coating (Figure 6-2). Magnitude of measured noise

increased to  $3.9\mu\text{V}$ . The steady decline of differential voltage suggests temperature is affecting measurement since a single microcantilever sensor connected in a Wheatstone bridge is not temperature compensated. Likewise, new cantilever sensor substituted in place of old type microcantilever sensor resulted in further increased noise level and downward differential voltage trend (Figure 6-3). New device noise level was  $7.5\mu\text{V}$ , suggesting increased sensitivity to thermal effects. This observation is consistent with temperature calibrations performed on the two device types (section 4.1).



**Figure 6-2: Wheatstone bridge with one old type cantilever connected in place of a fixed resistor.**

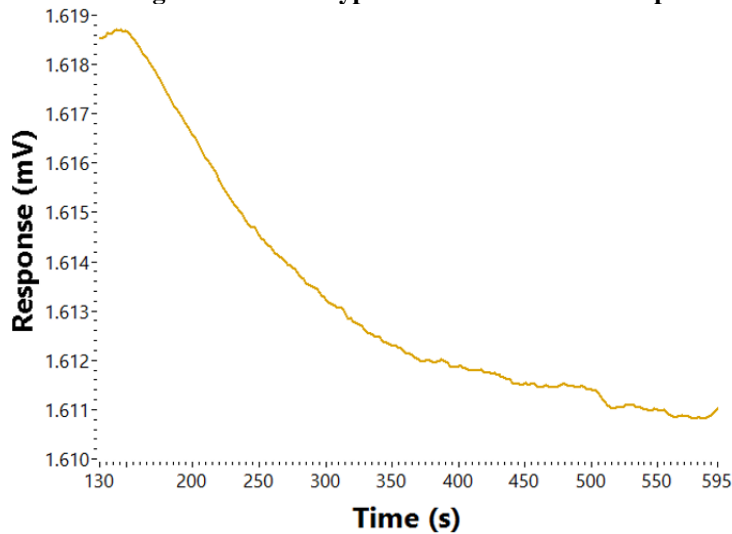


**Figure 6-3: Wheatstone bridge with one new type cantilever connected in place of a fixed resistor.**

Temperature effects in new cantilevers are reduced by design when a full Wheatstone bridge is used with no external resistors present. In addition, due to increased thermal mass of the new flow cell, the temperature of the analyte and device was better controlled (Figure 6-4).

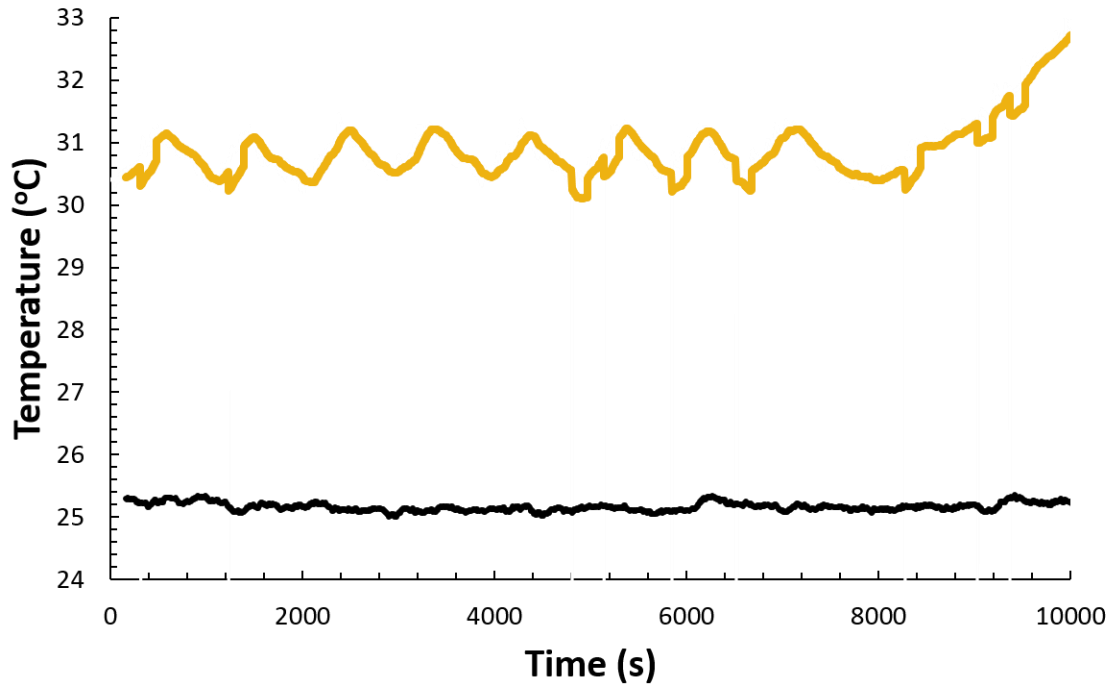


**Figure 6-4: New cantilever setup with active heating set to 25°C was more stable than old cantilever setup with set point of 30°C due to increased thermal mass.**

## 6.2 External Heating Methods

Though piezoresistive heating elements were embedded in some new devices, the optimized design modeled by Dr. Venkatasubramanian did not have external heating capabilities [21]. Previous generation microcantilevers were heated by increasing the temperature of the flow cell. Due to increased thermal mass of the new test cell, desorption by heating the whole flow cell required excessive heating and cooling times. In addition, built in hydrators would undergo identical temperature changes, increasing diffusion rates through the tubing, potentially exposing the cantilevers to the analyte during desorption steps.

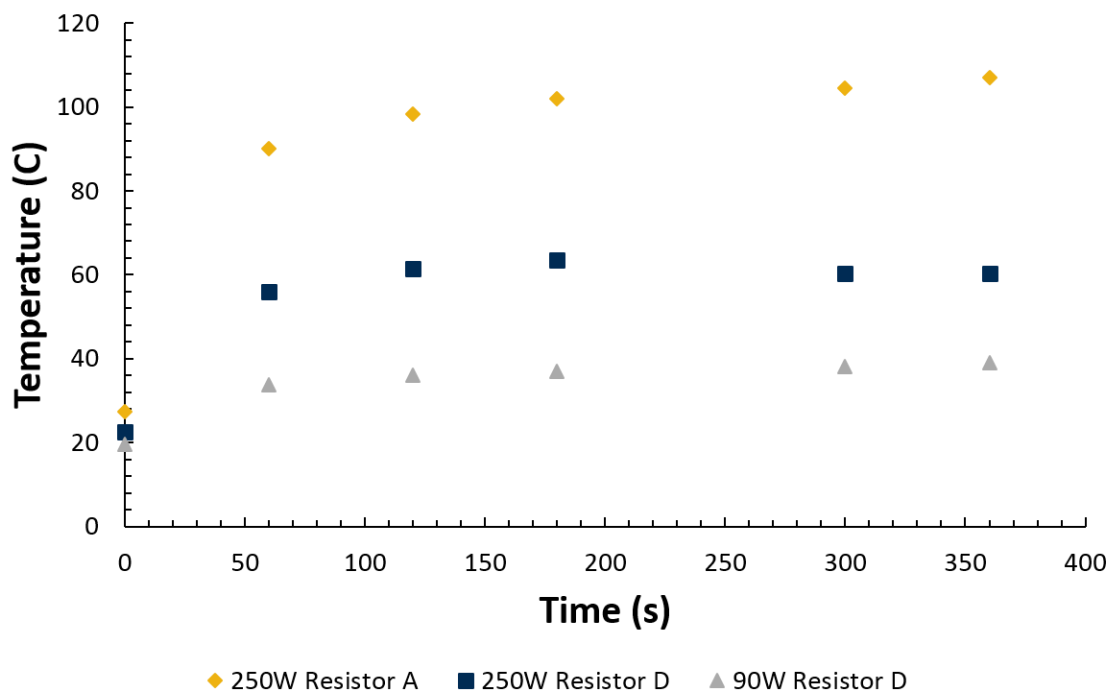


**Figure 6-5: Heating of cantilever device by halogen lamp exposure.**

To overcome desorption challenges, a 250Watt halogen bulb was purchased and fitted above the new flow cell. A temperature calibrated cantilever sensor was used as a temperature gauge to measure the temperature of the device. The halogen light successfully heated the cantilever portion (piezoresistor A) of the device to over 100°C, temperature sufficient to desorb analytes such as decane, hexane and acetone mid experiment (Figure 6-5). Interestingly, piezoresistor D (Figure 6-6) only heated up to 60°C, this may be due to increased conductive heat transfer due to the substrate acting as a heat sink. Temperature of the flow cell only increased to 36°C from initial temperature of 24°C in the same amount of time, suggesting predominantly localized heating of the cantilevers.

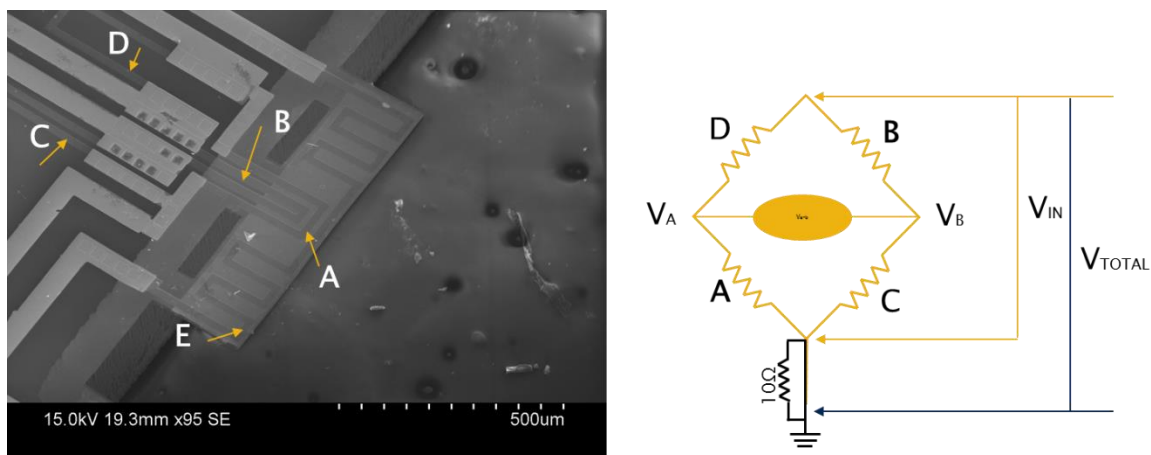


**Figure 6-6: Wheatstone bridge as it is laid out on the microcantilevers. Conductor E can be used as a temperature sensor or heating element.**

### 6.3 HKUST-1 Response on New Design with Heaters

#### 6.3.1 New Setup Dehydration Procedure

New device coatings were grown directly on  $\text{SiO}_2$  substrate due to temperature limitations in SAM based coatings as well as modeling results suggesting improved response of HKUST-1 on  $\text{SiO}_2$  [21] (Figure 3-3). This is likely due to increased stiffness of the microcantilever with introduction of materials with larger Young's moduli.

The new flow cell was designed with sealing capabilities (Section 2.4), allowing for isolation of device from surroundings post dehydration. There were two separate procedures developed to dehydrate and prepare the film for testing, one of which was outlined in Section 2.4.2. The second procedure involved the following steps, and generally required less preparation time but was more susceptible to sample contamination prior to exposure:

1. Place a device into the test cell.
2. Load an empty vial into hydrator port.
3. Close the lid and tighten bolts
4. Close all inlets, open outlet.
5. Heat cell to  $50^\circ\text{C}$ .

6. Connect outlet to pump and degas for 1 minute.
7. Close outlet port, then turn off and disconnect the pump.
8. Connect a transparent 1/4" tube section to the hydrator inlet valve.
9. Use a syringe to fill the tube with 1mL of analyte, mark the meniscus.
10. Add 2 more mL to a total of 3mL.
11. Slowly open the valve until the liquid level begins to drop slowly at a rate of about 1/10mL per second.
12. When the 1mL mark is reached, close the valve and remove the tube.
13. Use nitrogen/air gun to dry the valve and connect the MFC gas supply tubing to the hydrator line.
14. Carry on experiments in regular fashion.

Above procedure was shown to fill the bubbler without allowing any atmospheric air from contaminating the chamber, however, it presents analyte contamination issues due to the necessity of the analyte to flow through tubing. The tubing has to be decontaminated to reduce likelihood of cross contamination from different analytes between runs.

Both procedures work by reducing the pressure of the MOF surroundings, effectively lowering the boiling point of water. By ensuring the temperature is slightly elevated (50°C) and pressure is below 7kPa (resulting in boiling point of roughly 40°C) the film was degased without damage to device or film.

### **6.3.2 Experimental Results and Discussion**

60 cycles (200nm) of HKUST-1 was grown on SiO<sub>2</sub> substrate (Figure 6-9). The device used for testing was a wide cantilever with embedded heating elements and cutouts. Dehydration procedure was performed on the device, no heat was applied to the test cell during experiment. Temperature of the room was 23.7°C. Step response to water was measured using a temperature compensated Wheatstone bridge (Figure 6-8).

Comparing the response of the new type cantilever to the old type cantilever it is evident that response is weaker despite increased thickness of MOF and optimized layers (Figure 6-7). This may be explained by a number of factors. First and foremost, as can be seen in Figure 6-7, the device coating appears to be non-uniform, with approximately half the cantilever uncoated. In addition, the heating element introduces substantial structural rigidity. Modeling showed placing resistors away from the axis of symmetry resulted in reduced response [21]. In addition, both top and bottom of the new cantilever are SiO<sub>2</sub> substrates, therefore, some of the response may be canceled due to adsorption on the bottom. Modeling showed coating MOF on both top and bottom halved the response.

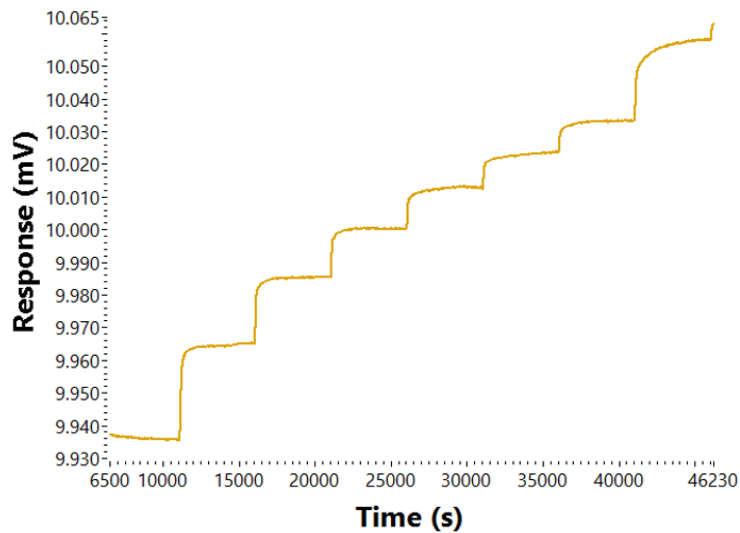


**Figure 6-8: Step response of wide microcantilever of new type to water. 60 cycles CuBTC on SiO<sub>2</sub>.**

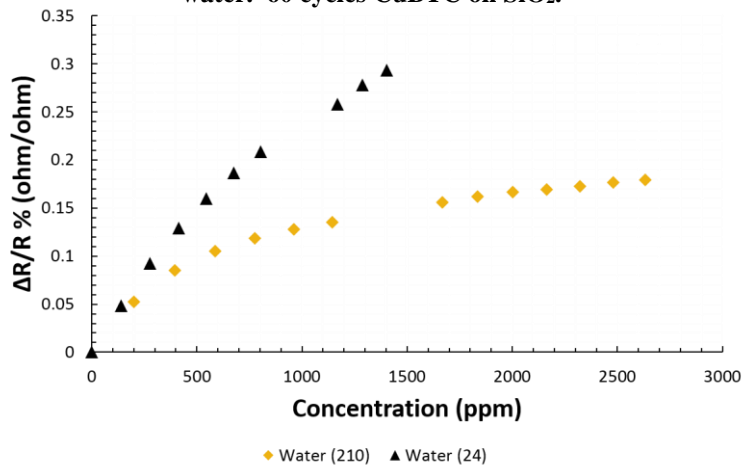


**Figure 6-7: Response of new type device (210) with 60 cycles of CuBTC vs. response of old type device with 40 CuBTC on SAM (24).**

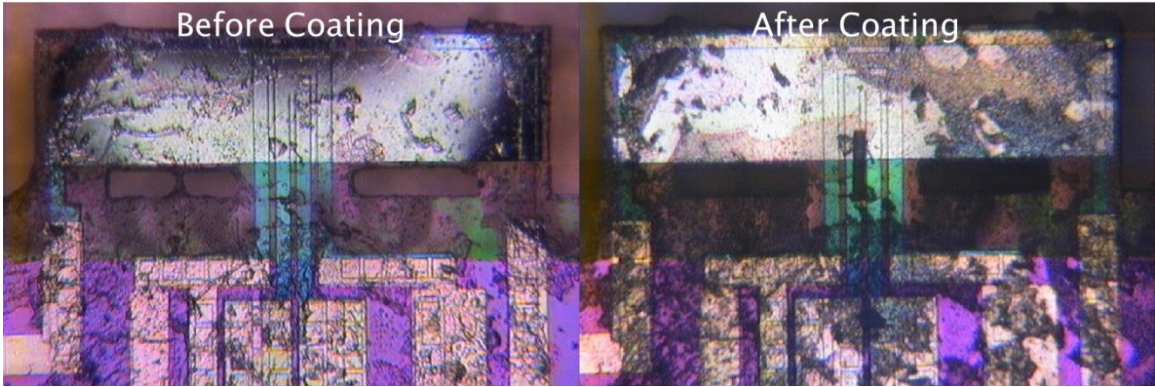


**Figure 6-9: 60 cycles of CuBTC on SiO<sub>2</sub>. MOF appears to have grown less uniformly than on old type cantilevers.**

Old type cantilevers had oxide tops and nitride bottoms, with preferential growth occurring on the top of the cantilever. Improved response can be achieved by using cantilevers of wide design without heaters, and using a PECVD deposited nitride layer on the bottom of future cantilevers. It was demonstrated that flipping a new cantilever die face down, results in no damage to the cantilever or piezoresistors.

## CHAPTER 7 CONCLUSION AND FUTURE WORK

### 7.1 Concluding Remarks

Improved gas sensing solutions are necessary to provide accurate results in a diverse set of environments. Devices must deliver stable, reliable readings packaged in a low cost, ultra-portable, low power solution for detection of multiple analytes in complex mixtures. Though many products are currently available, none manage to combine all the desirable attributes of a complete solution.

Microcantilevers have been adapted as transduction mechanisms for sensing applications. Taking advantage of often simple physical relations, cantilevers are used in many different configurations ranging from optical/frequency mass uptake detectors to piezoresistive strain detectors. Piezoresistive cantilevers have a number of strengths including simple fabrication, good sensitivity, low cost, low power and compact size. The simple instrumentation required to acquire measurements with Wheatstone bridge make these devices highly portable.

Piezoresistive microcantilever sensors on their own are not capable of detecting analytes, such as VOC's. Detection is accomplished via a selective layer deposited on the surface of the device. Strain in the selective layer, causes the electrical signal generated by the piezoresistive effect. Many selective layers are being studied ranging from metal coatings to various polymer chains. A relatively new class of highly porous materials with large internal surface areas has recently emerged. MOFs provide the advantages of variable pore sizes, large selection of structures, flexible framework, thermal stability and solvent stability. Analyte uptake in MOFs is not well understood but is generally governed by steric effects and adsorbate-adsorbant interactions resulting in a sieving effect. Thousands of MOFs are available with some exhibiting added beneficial properties such as expansion upon adsorption of analyte.

Leveraging low cost and versatility of microcantilevers and combining them with the vastly diverse group of flexible, selective MOFs was shown to result in a device which successfully measured response to nine different analytes. It was demonstrated that HKUST-1 (CuBTC) can be used as a reversible, stable selective layer and that the piezoresistive microcantilever provides a reliable transduction mechanism for quantifying the response to VOCs.

In order to characterize response in a well-controlled environment, a custom built experimental setup was used. Original setup was capable of introducing VOCs to a metal test cell via a network of mass flow controllers and tubes with the aid of a humidifier, however, it lacked temperature control and a hermetically sealed environment. To improve data quality, the system was redesigned with the goal of integrating all vital components in a single, hermetically sealed, temperature controlled test cell. The miniaturized flow setup was fabricated out of aluminum and was shown to improve temperature stability, reduce analyte waste, aid in dehydration of MOF films while reducing costs of operation. LabView was interfaced with the instrumentation resulting in an autonomous data acquisition system capable of measuring up to two bridges at one time.

New generation of microcantilever sensors was designed specifically for use with MOF selective layers. Optimization study using COMSOL showed improved response with wider microcantilevers. The die was redesigned to include up to five complete Wheatstone bridges with two resistors on the surface of the microcantilever. This arrangement doubled response due to strain while providing temperature compensation. Number of dies was increased by five times, while number of Wheatstone bridges per wafer increased by over four times. Nine different designs were fabricated on each wafer including membranes and devices with different heating piezoresistive heating elements. Six wafers were processed, four with over 95% structure release rate. Three wafers were

released with moderate-high device yield resulting in hundreds of working microcantilever sensors.

Rigorous characterization protocol was followed to select and prepare devices for testing. Nearly 10,000 electrical contacts were measured to identify working resistors. Images of all cantilevers on each working die were acquired and stored in a unique folder with a serial number corresponding to an individual storage box for each device. Resistance measurements and images were taken throughout coating procedure and prior to testing. Devices were wirebonded to a package and prepared for testing.

HKUST-1 was selected due to its high internal surface area, and flexible framework. The film was grown at Sandia National Laboratories using layer-by-layer deposition techniques, resulting in uniform, highly ordered films with well controlled thickness.

Devices were subjected to strenuous testing with twelve analytes. In one case, a single device was used in 170 different experiments over a period of 18 months with no adverse effect to the selective coating or to the piezoresistive elements. A few devices without MOF coatings were used for temperature calibration experiments to study effects of temperature gradients on response and were exposed to temperatures as high as 120°C.

Two types of experiments were conducted on 100nm HKUST-1 coated device (40 cycles CuBTC on SAM). Mixed exposure experiment was used to study degree of reversibility of the response to the twelve different analytes. Data from mixed exposure experiments was also used to calculate adsorption time constant values to determine rates of response to the different analytes. Step exposure experiments were used to characterize response curves for different analytes. These curves were fit with models, such as Langmuir and Henry's to determine adsorption properties of HKUST-1 for different analytes.

Analytes were sorted into four groups based on their response characteristics. Carbon dioxide, hexamethyldisiloxane and 1,2 dichloroethane did not result in any strain

response. Decane and hexane displayed irreversible characteristics due to saturation of the film over time. Poor reversibility was observed for toluene, isopropanol, ethanol, acetone and chloroform. Good reversibility was observed for methanol and water.

Water response was tested against a commercial capacitance based sensor and resulted in good agreement between the devices reinforcing validity of the experimental setup. Unique characteristics were observed for some analytes, allowing to segregate analytes based on response times, shapes of response, strength of response as well as reversibility properties.

Sensitivity of devices was quantified by measuring response at low concentrations and estimating limits of detection by linearizing response while factoring in setup noise. Lowest measured value for water was 6 ppm with an estimated LOD of 3 ppm.

Experimental results reinforced viability of MOF coated piezoresistive microcantilever sensors for applications in gas sensing. Devices proved to be durable, reliable and low power ( $13\mu\text{W}$ /Wheatstone bridge). Fabrication process showed promise of high yield on a commercial scale. HKUST-1 was shown to be selective and versatile film with excellent thermal and solvent stability. Completely reversible response was achieved for all analytes after application of heat.

Many desirable traits for a multipurpose gas sensing solution were demonstrated in this thesis. With further investigation, piezoresistive microcantilevers with selective MOF coatings may provide a versatile platform for gas sensing solutions in the 21<sup>st</sup> century.

## 7.2 Future Work

As was mentioned in section 1.4, three other MOFs were successfully coated on old type microcantilever sensors and tested in the mixed experimental setup. Detection of multiple analytes can be accomplished by an array of microcantilevers with different coatings. MOFs that work well together may be used to single out target analytes by working together on a single device. NOTT-100, NOTT-101 and ZIF-8 showed promising potential as secondary selective layers to complement CuBTC. Results were withheld from this thesis due to incomplete sets of data for these MOFs. Furthermore, these MOFs were grown on different substrates with different layer configurations, making direct comparisons in response impractical. Characterizing response of these MOFs on new type microcantilevers will provide insight into potential combinations that may work to detect concentrations of analyte mixtures.

Nine different types of devices were fabricated on the new wafers. A study to determine strengths and weaknesses of each design should be conducted to identify most sensitive solution. A COMSOL model should be implemented to gather a physical understanding of each of the designs. Identical selective layers may be grown, and identical exposure conditions can be used to experimentally confirm modeling results. Further, upper and lower limits of detection for water should be studied on each design and for various thicknesses of MOF to find optimal geometry and selective layer thickness.

New experimental flow cell was designed for acquisition of up to five bridges at one time. Another multiplexer can be integrated into the current experimental setup to accomplish this task. Gathering data on five devices simultaneously may provide insight into response uniformity across different bridges with identical MOF growth conditions.

Appropriate dehydration procedures, made possible by the new test cell, should be conducted for HKUST-1 on an optimized new cantilever. Response to each analyte may be different when residual water vapor is removed from the MOF. As was

previously mentioned, HKUST-1 response to carbon dioxide is well documented, however, no response was seen on the old type microcantilevers without dehydration. It was hypothesized that lack of response was due to residual water within HKUST-1 because of insufficient dehydration procedure.

Finally, experiments should be conducted to verify possibility of desorption of analytes while acquiring data with aid of heating elements or an external halogen lamp. It was hypothesized that short exposure of the MOF to high temperatures would aid in the desorption process of analyte in a timely fashion. It should be demonstrated that desorption of decane and hexane can be achieved by using such methods.

## **APPENDIX A: FABRICATION PROCESS OUTLINE**

This section outlines details of the fabrication process. The process was developed with Dr. Hesketh and Dr. Venkatasubramanian based on prior work by Dr. Lee [14] and Dr. Choudhury [18]. Slides below are included to show all processing steps and equipment.



# **Microcantilever Fabrication Process**

**Process Developed By:**  
Ilya Ellern,  
Anandram Venkatasubramanian  
Peter J. Hesketh  
May 18 2013



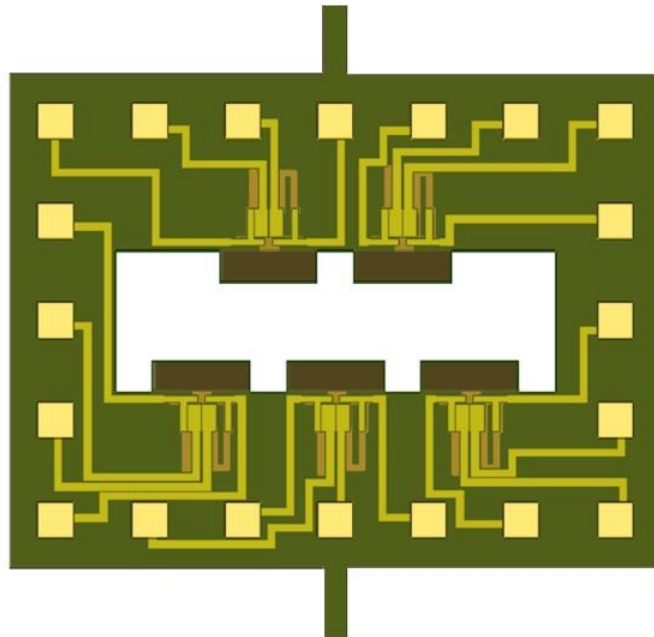
## Cantilever Fabrication Process

1. Doping of silicon
2. Anneal the wafer to activate the dopant
3. Pattern the strain gauges
4. Grow silicon dioxide of almost equal thickness of Bottom Oxide layer
5. Deposit and pattern metal for mirroring the cantilever
6. Open contacts to metallization and the Cantilever edge definition
7. Pattern and deposit metal for contacts
8. Post Annealing step for gold – resistor bonding
9. Deposit and pattern the passivation layer and the Cantilever edge definition
10. Pattern and etch poly silicon



2

### Die design



3

# Masks

- ▶ Mask 1 – Piezoresistor Definition
- ▶ Mask 2 – Depositing Al mirrors on the cantilever.
- ▶ Mask 3 – Opening contact windows for metal deposition and cantilever edge definition
- ▶ Mask 4 - Metallization of contacts
- ▶ Mask 5 – Opening contact pads for wire bonding
- ▶ Mask 6 – Back Side Etch



## PreStep: SoiTec SOI Wafer

Item	Quantity	Description	Unit Price	Total Price
1	20	4" UNI BOND SOI Wafers	(Part ID # 40000P G4P-005-01)	\$ 350.00
\$7,000.00				

Smart Cut Process:  
Si thickness 340nm  
BOX thickness 400nm  
(Prime Quality)

**Starting Material**  
Active wafer: p -type, FZ, <1 00>, 14 - 22 ohm -cm  
Handle wafer: p -type, CZ, <100>, 14 - 22 ohm -cm, 525 um thick

Item	Quantity	Description	Unit Price	Total Price
2	20	4" UNIBOND SOI Wafers	(Part ID # 40000P G4P-005-01)	\$325.00
\$8,450.00				

Smart Cut Process:  
Si thickness 340nm  
BOX thickness 400nm  
(Prime Quality)

**Starting Material**  
Active wafer: p -type, FZ, <1 00>, 14 - 22 ohm -cm  
Handle wafer: p -type, CZ, <100>, 14 - 22 ohm -cm, 525 um thick

- Notes:**
- 1.) Important: For shipping purposes, please include Federal Express Acct. # as well as Federal Tax I.D. # (same as E I N #) to expedite shipment through customs.
  - 2.) Wafers as quoted are presently in -stock, but are subject to prior sale.

Quote Validity: 30 days  
F.O.B.: Factory, Bermin, France  
Delivery: 2 - 3 weeks a. r. o.  
Payment Terms: Net 30 days at invoice date



Emily Elie [eeilie@soitecusa.com](mailto:eeilie@soitecusa.com)  
Sales Administrator/SOITEC/USA  
2 Centennial Dr.  
Peabody, MA 01960  
Tel (978) 531-2222 Fax (978) 531-2758  
[soi@soitecusa.com](mailto:soi@soitecusa.com)



## FabStep 1: Inspection Under Nanospec

		<table border="1"> <tr><td>SCS</td></tr> <tr><td>Bottom SiO<sub>2</sub></td></tr> <tr><td>Polycrystalline Silicon</td></tr> </table>	SCS	Bottom SiO <sub>2</sub>	Polycrystalline Silicon
SCS					
Bottom SiO <sub>2</sub>					
Polycrystalline Silicon					
<b>Process</b>	<b>Inspection Under Nanospec</b>				
<b>Machine/Vendor</b>	Nanospec Refractometer (Marcus Inorganic)				
<b>Process Specs</b>	Use SOI 400nm recipe to verify wafer specs				
<b>Time</b>	5				
<b>Comments</b>	Expect: 340 nm of SCS and 400 nm of SiO <sub>2</sub>				



## FabStep 2: Doping

**CORE**  
The Leader in Fab Services

1050 Kifer Road TEL: (408) 328-1340  
Sunnyvale, CA 94086 FAX: (408) 328-1346

A division of  
**IMPLANT  
SCIENCES  
CORPORATION**

Quotation Number : 13075

Date: Wednesday, April 26, 2006

Customer: Georgia Tech - Woodruff School of ME

Phone: 404-385-2014

Attention: Arnab Choudhury

FAX: gtg301c@prism.gatech.edu

FOB:  
Sunnyvale

Terms:  
Net 30 Days

Ship Via:

RFQ Number:

Item	Qty	Specie / Description	Unit Cost	Extended
1	1	P / 4 in / 1 Batch / 20 Wafers / 7.00E+14 / 120 KeV / 7° Tilt	\$117.89	\$117.89
2	1	Setup charge P /	\$250.00	\$250.00
<b>Total</b>			<b>\$367.89</b>	<b>\$367.89</b>

- ▶ Contact person: Chuck Hudak [chudak@coresystems.com](mailto:chudak@coresystems.com)
- ▶ Lead time 4~5 days



## FabStep 3: Piranha Clean

		
<b>Process</b>	<b>Piranha Clean</b>	
<b>Machine/Vendor</b>	CMOS Cleaning Station (Marcus Inorganic or Petit)	
<b>Process Specs</b>	Piranha: 7:3 (Peroxide:Sulfuric Acid), 10 minutes	
<b>Time</b>	~ 10 mins at 120C	
<b>Comments</b>	Rinse (10 minutes), Dry (2 minutes)	



 PECVD Oxide	 Thermal Oxide	 SCS N-Doped	<b>Georgia Tech</b> 
 Poly Silicon	 Nitride	 Aluminum	
		 Photoresist	

8

## FabStep 4: Dopant Reactivation

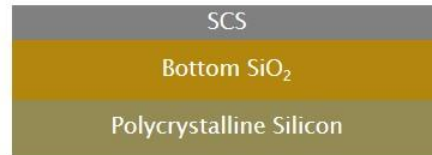
		
<b>Process</b>	<b>Dopant Reactivation</b>	
<b>Machine/Vendor</b>	Tystar Poly Furnace 1 (Annealing Tube) – Petit	
<b>Process Specs</b>	High Temp (~1050 ° C)	
<b>Time</b>	Dwell for 50 minutes.	
<b>Comments</b>	Wafers look pinkish after anneal; May process up to 8 wafers each time	



 PECVD Oxide	 Thermal Oxide	 SCS N-Doped	<b>Georgia Tech</b> 
 Poly Silicon	 Nitride	 Aluminum	
		 Photoresist	

9

## FabStep 5: Check Resistivity in Four Point Probe



<b>Process</b>	<b>Check Wafer Resistivity</b>
<b>Machine/Vendor</b>	Signatone Probe
<b>Process Specs</b>	Expected resistivity: TBD
<b>Time</b>	10 minutes
<b>Comments</b>	One wafer takes five minutes to run

PECVD Oxide	Thermal Oxide	SCS N-Doped	<b>Georgia Tech</b> 
Poly Silicon	Nitride	Aluminum	
		Photoresist	

10

## FabStep 6: Piranha Clean



<b>Process</b>	<b>Piranha Clean</b>
<b>Machine/Vendor</b>	CMOS Cleaning Station (Marcus Inorganic or Petit)
<b>Process Specs</b>	Piranha: 7:3 (Peroxide:Sulfuric Acid), 10 minutes
<b>Time</b>	~ 10 mins at 120C
<b>Comments</b>	Rinse (10 minutes), Dry (2 minutes)

PECVD Oxide	Thermal Oxide	SCS N-Doped	<b>Georgia Tech</b> 
Poly Silicon	Nitride	Aluminum	
		Photoresist	

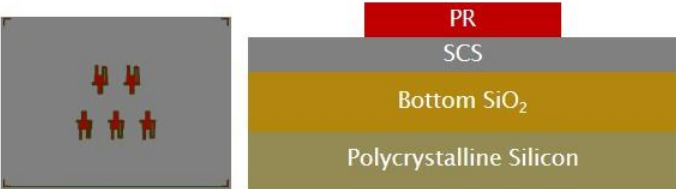
11

## FabStep 7: Dehydration Bake

	
<b>Process</b>	<b>Dehydration Bake</b>
<b>Machine/Vendor</b>	Dehydration Oven (Marcus Inorganic or Petit)
<b>Process Specs</b>	120°C
<b>Time</b>	30 minutes
<b>Comments</b>	Use any of the general use ovens in either cleanroom.

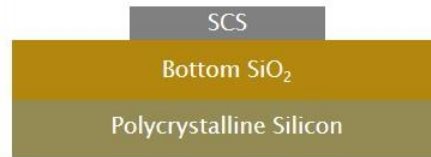
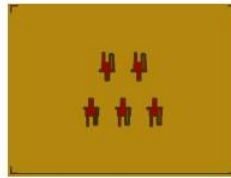
	PECVD Oxide		Thermal Oxide		SCS N-Doped	<b>Georgia Tech</b> 
	Poly Silicon		Nitride		Aluminum	
					Photoresist	
					12	

## FabStep 8: Photo Lithography Resistor Patterning

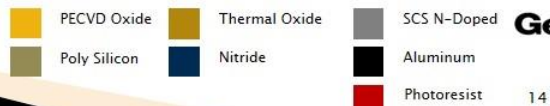
	
<b>Process</b>	<b>Spin Photo Resist</b>
<b>Machine/Vendor</b>	SCS GP38 Spinner (Marcus Inorganic)
<b>Process Specs</b>	Resist Type: Positive (Shibley 1813)      Ramp Up Rate: 500RPM/s (takes 6 seconds) Spin Parameters: 3000RPM for 50 seconds
<b>Time</b>	5 minutes per wafer
<b>Comments</b>	Pre-bake in oven at 110°C for 3 minutes
<b>Process</b>	<b>Pattern Photo Resist</b>
<b>Machine/Vendor</b>	Karl Suss MA-6 TSA Mask Aligner (Marcus Inorganic)
<b>Process Specs</b>	Channel: 2 (405nm Wavelength)      Contact Type: Hard      MASK #1 (Clear Field) Alignment Gap: 20µm      Dosage: 150 mJ/cm <sup>2</sup>
<b>Time</b>	Measure lamp power. (Sample Power: 15.4 mW/cm <sup>2</sup> then 150/(15.4-1) = <b>10.4s exposure</b> )
<b>Comments</b>	1. Post-exposure bake in oven at 110°C for 3 minutes 2. Develop in 500mL of MF-319 for 3 minutes one wafer at a time. Change every 3 wafers. 3. Hard Bake at 110°C for 3 minutes

	PECVD Oxide		Thermal Oxide		SCS N-Doped	<b>Georgia Tech</b> 
	Poly Silicon		Nitride		Aluminum	
					Photoresist	
					13	

## FabStep 9: ICP Etch of Single Crystal Silicon



<b>Process</b>	<b>Inductively Coupled Plasma Etching of Single Crystal Silicon Defining Piezoresistive Elements</b>
<b>Machine/Vendor</b>	Plasma-Therm ICP (Petit)
<b>Process Specs</b>	Use recipe with a Low Pressure O2 plasma descumming which will then etch SCS. (This recipe will take care of descumming followed by Si Etch)
<b>Time</b>	10 minutes, Si etch rate 0.3 micron/cycle. 5 cycles (rates subject to change)
<b>Comments</b>	Use Nanospec Refractometer to make sure SCS has been etched all the way through. Inspect all regions of the wafer. Extend etch if SCS remains.

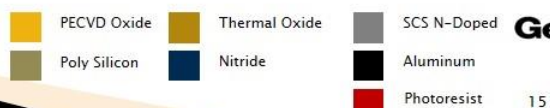


14

## FabStep 10: Resist Removal



<b>Process</b>	<b>Acetone, Methanol, Isopropanol Wash</b>
<b>Machine/Vendor</b>	Wet Bench (Marcus Inorganic)
<b>Process Specs</b>	1. Pour Acetone on the wafer and wash off all the photoresist. 2. Wash both sides of the wafer with Methanol. 3. Wash both sides of the wafer with Isopropanol.
<b>Time</b>	3 minutes or until all resist has been removed.
<b>Comments</b>	If resist is not coming off, soak in Acetone overnight and repeat the wash steps in 24 hours. Consider reducing the hard bake time if this occurs.



15

## FabStep 10: Wafer Inspection



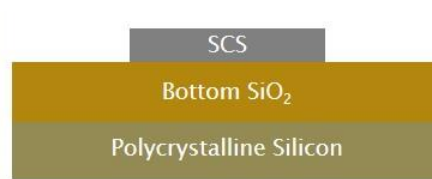
Process	Measure Step
Machine/Vendor	Dektak 150 Profilometer (Marcus Inorganic)
Process Specs	Measure the thickness of the SCS. (Should be approximately 340nm)
Time	10 minutes per wafer
Comments	Make sure to check center and at least four points on the perimeter.

Process	Measure Oxide Thickness
Machine/Vendor	Nanospec Refractometer (Marcus Inorganic)
Process Specs	Use Oxide on Silicon recipe to check thickness of the bottom SiO <sub>2</sub> layer. (Should be 400nm)
Time	1 minute
Comments	Make sure to perform calibration of device before measurement.

- PECVD Oxide
- Thermal Oxide
- SCS N-Doped
- Poly Silicon
- Nitride
- Aluminum
- Photoresist

16

## FabStep 11: Piranha Clean



Process	Piranha Clean
Machine/Vendor	CMOS Cleaning Station (Marcus Inorganic or Petit)
Process Specs	Piranha: 7:3 (Peroxide:Sulfuric Acid), 10 minutes
Time	~ 10 mins at 120C
Comments	Rinse (10 minutes), Dry (2 minutes)

- PECVD Oxide
- Thermal Oxide
- SCS N-Doped
- Poly Silicon
- Nitride
- Aluminum
- Photoresist

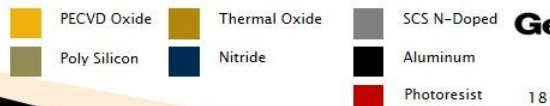
17

## FabStep 12: Grow Thermal Oxide



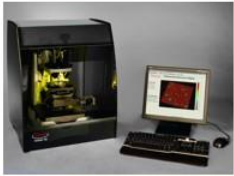


Process	Encapsulation of SCS in Thermal Oxide
Machine/Vendor	Tystar Poly Furnace (Petit)
Process Specs	1. Use oxidation Tube 2 2. 7 Hours and 30 Minutes @ 1100C 3. Use Dry Oxidation conditions
Time	13.5 Hours
Comments	May process up to 8 wafers each time. Insert a blank Si test wafer to measure the thickness to confirm process parameter.



18

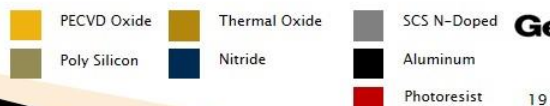
## FabStep 13: Wafer Inspection





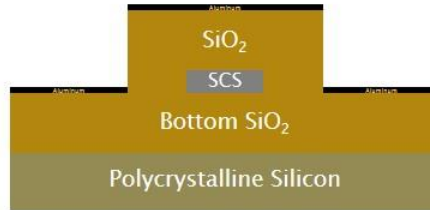
Process	Measure Step
Machine/Vendor	Dektak 150 Profilometer (Marcus Inorganic)
Process Specs	Measure the thickness of the SCS + top SiO <sub>2</sub> . (Should be approximately 440nm)
Time	10 minutes per wafer
Comments	Make sure to check center and at least four points on the perimeter.

Process	Measure Oxide Thickness
Machine/Vendor	Nanospec Refractometer (Marcus Inorganic)
Process Specs	Use Oxide on Silicon recipe to check thickness of the bottom SiO <sub>2</sub> layer. (Should be 400nm)
Time	1 minute
Comments	Make sure to perform calibration of device before measurement.



19

## FabStep 14: Metallization of Aluminum



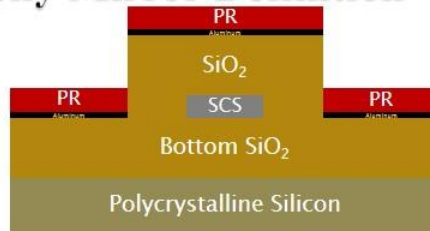
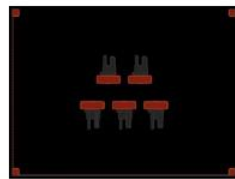
<b>Process</b>	<b>Evaporate Aluminum Mirrors</b>
<b>Machine/Vendor</b>	Denton Explorer (Marcus)
<b>Process Specs</b>	<ol style="list-style-type: none"> <li>40 nm thick metal layer</li> <li>1A/s Deposition Rate</li> <li>Wait for pressure to go below <math>9 \times 10^{-7}</math> Torr</li> </ol>
<b>Time</b>	2 Hours
<b>Comments</b>	May process up to 3 wafers each time. Insert a glass slide on the side, use tape to hold it in place. You can use the glass slide to measure deposited thickness using Dektak 150 Profilometer.

PECVD Oxide	Thermal Oxide	SCS N-Doped
Poly Silicon	Nitride	Aluminum
		Photoresist



20

## FabStep 15: Photo Lithography Mirror Definition



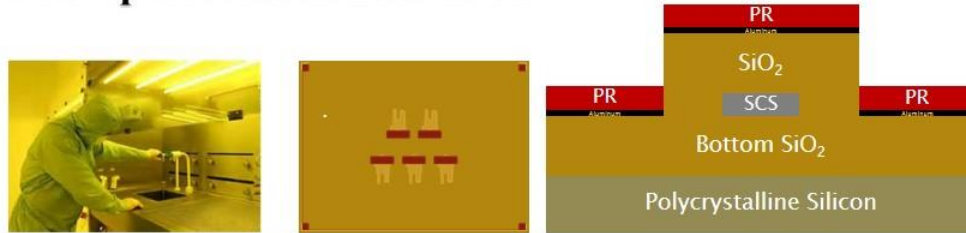
<b>Process</b>	<b>Spin Photo Resist</b>						
<b>Machine/Vendor</b>	SCS GP38 Spinner (Marcus Inorganic)						
<b>Process Specs</b>	<table border="0"> <tr> <td>Resist Type: Positive (ShIPLEY 1813)</td> <td>Ramp Up Rate: 500RPM/s (takes 6 seconds)</td> </tr> <tr> <td>Spin Parameters: 3000RPM for 50 seconds</td> <td></td> </tr> </table>	Resist Type: Positive (ShIPLEY 1813)	Ramp Up Rate: 500RPM/s (takes 6 seconds)	Spin Parameters: 3000RPM for 50 seconds			
Resist Type: Positive (ShIPLEY 1813)	Ramp Up Rate: 500RPM/s (takes 6 seconds)						
Spin Parameters: 3000RPM for 50 seconds							
<b>Time</b>	5 minutes per wafer						
<b>Comments</b>	Pre-bake in oven at 110°C for 3 minutes						
<b>Process</b>	<b>Pattern Photo Resist</b>						
<b>Machine/Vendor</b>	Karl Suss MA-6 TSA Mask Aligner (Marcus Inorganic)						
<b>Process Specs</b>	<table border="0"> <tr> <td>Channel: 2 (405nm Wavelength)</td> <td>Contact Type: Hard</td> <td>MASK #2 (Clear Field)</td> </tr> <tr> <td>Alignment Gap: 20µm</td> <td>Dosage: 150 mJ/cm<sup>2</sup></td> <td></td> </tr> </table>	Channel: 2 (405nm Wavelength)	Contact Type: Hard	MASK #2 (Clear Field)	Alignment Gap: 20µm	Dosage: 150 mJ/cm <sup>2</sup>	
Channel: 2 (405nm Wavelength)	Contact Type: Hard	MASK #2 (Clear Field)					
Alignment Gap: 20µm	Dosage: 150 mJ/cm <sup>2</sup>						
<b>Time</b>	Measure lamp power. (Sample Power: 15.4 mW/cm <sup>2</sup> then $150 / (15.4 - 1) = 10.4s$ exposure						
<b>Comments</b>	<ol style="list-style-type: none"> <li>Post-exposure bake in oven at 110°C for 3 minutes</li> <li>Develop in 500mL of MF-319 for 3 minutes one wafer at a time. Change every 3 wafers.</li> <li>Hard Bake at 110°C for 3 minutes</li> </ol>						

PECVD Oxide	Thermal Oxide	SCS N-Doped
Poly Silicon	Nitride	Aluminum
		Photoresist



21

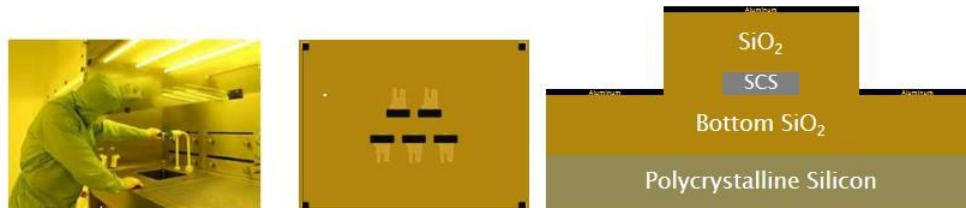
## FabStep 16: Aluminum Etch



<b>Process</b>	<b>Aluminum Etchant</b>
<b>Machine/Vendor</b>	Wet Bench (Marcus Inorganic)
<b>Process Specs</b>	<ol style="list-style-type: none"> <li>1. Submerge in 500mL of Aluminum Etchant for 5 minutes</li> <li>2. Rinse with deionized water</li> <li>3. Dry with Nitrogen gun</li> <li>4. Inspect to make sure all Aluminum is gone.</li> </ol>
<b>Time</b>	10 minutes or until all resist has been removed.
<b>Comments</b>	Process up to 3 wafers in the same bath. Check under microscope to make sure all aluminum came off. Repeat step if necessary. Dispose of etchant in a separate waste container, DO NOT POUR DOWN THE DRAIN. Wear Acid gloves.



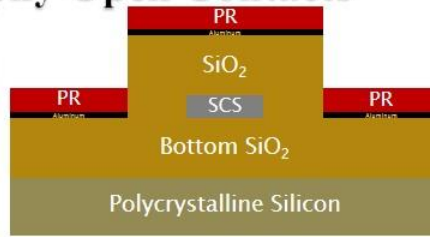
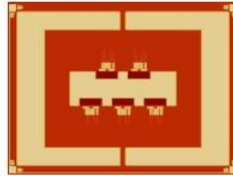
## FabStep 17: Resist Removal



<b>Process</b>	<b>Acetone, Methanol, Isopropanol Wash</b>
<b>Machine/Vendor</b>	Wet Bench (Marcus Inorganic)
<b>Process Specs</b>	<ol style="list-style-type: none"> <li>1. Pour Acetone on the wafer and wash off all the photoresist.</li> <li>2. Wash both sides of the wafer with Methanol.</li> <li>3. Wash both sides of the wafer with Isopropanol.</li> </ol>
<b>Time</b>	3 minutes or until all resist has been removed.
<b>Comments</b>	If resist is not coming off, soak in Acetone overnight and repeat the wash steps in 24 hours. Consider reducing the hard bake time if this occurs.



## FabStep 18: Photo Lithography Open Contacts



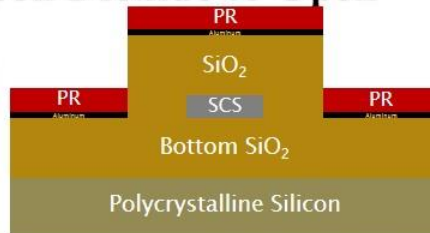
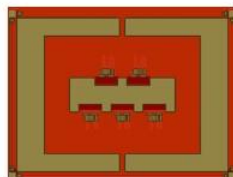
<b>Process</b>	<b>Spin Photo Resist</b>		
<b>Machine/Vendor</b>	SCS GP38 Spinner (Marcus Inorganic)		
<b>Process Specs</b>	Resist Type: Positive (Shipley 1813) Spin Parameters: 3000RPM for 50 seconds	Ramp Up Rate: 500RPM/s (takes 6 seconds)	
<b>Time</b>	5 minutes per wafer		
<b>Comments</b>	Pre-bake in oven at 110°C for 3 minutes		
<b>Process</b>	<b>Pattern Photo Resist</b>		
<b>Machine/Vendor</b>	Karl Suss MA-6 TSA Mask Aligner (Marcus Inorganic)		
<b>Process Specs</b>	Channel: 2 (405nm Wavelength) Alignment Gap: 20µm	Contact Type: Hard Dosage: 150 mJ/cm <sup>2</sup>	MASK #3 (Dark Field FeO <sub>2</sub> )
<b>Time</b>	Measure lamp power. (Sample Power: 15.4 mW/cm <sup>2</sup> then 150/(15.4-1) = <b>10.4s exposure</b> )		
<b>Comments</b>	<ol style="list-style-type: none"> <li>1. Post-exposure bake in oven at 110°C for 3 minutes</li> <li>2. Develop in 500mL of MF-319 for 3 minutes one wafer at a time. Change every 3 wafers.</li> <li>3. Hard Bake at 110°C for 3 minutes</li> </ol>		

PECVD Oxide	Thermal Oxide	SCS N-Doped
Poly Silicon	Nitride	Aluminum
		Photoresist



24

## FabStep 19: ICP Etch of Silicon Dioxide to Open Contacts



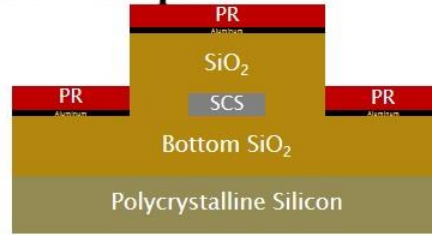
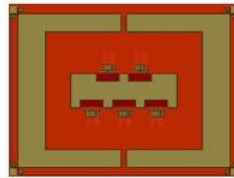
<b>Process</b>	<b>Inductively Coupled Plasma Etching of Silicon Dioxide to Open Contacts to SCS for Metallization. Also Defines the Cantilever and Die Outline.</b>		
<b>Machine/Vendor</b>	Plasma-Therm ICP (Petit)		
<b>Process Specs</b>	Use Std OX recipe to etch through all the SiO <sub>2</sub> on the contacts.		
<b>Time</b>	2 minutes 2000A/minute etch rate (rates subject to change)		
<b>Comments</b>	If SiO <sub>2</sub> was completely removed from the contacts but there still over 100nm left elsewhere, stop etching anyway to avoid damage to SCS layer. Resist can be removed at a later step.		

PECVD Oxide	Thermal Oxide	SCS N-Doped
Poly Silicon	Nitride	Aluminum
		Photoresist

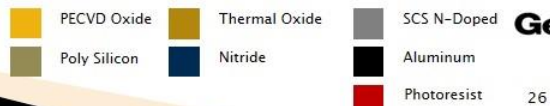


25

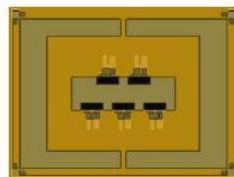
## FabStep 20: Inspection Under Nanospec



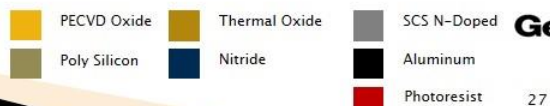
<b>Process</b>	Inspection Under Nanospec
<b>Machine/Vendor</b>	Nanospec Refractometer (Marcus Inorganic)
<b>Process Specs</b>	<ol style="list-style-type: none"> <li>1. Use SOI 400nm recipe to verify SCS thickness (130nm expected)</li> <li>2. Use Oxide on Silicon recipe to check how much SiO2 is left elsewhere.</li> </ol>
<b>Time</b>	5 minutes
<b>Comments</b>	Remember to calibrate before every use.



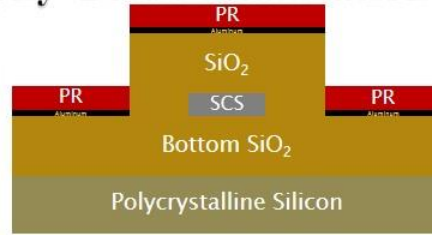
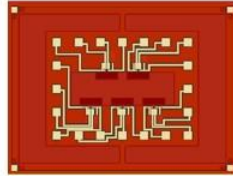
## FabStep 21: Resist Removal



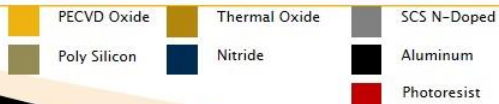
<b>Process</b>	Acetone, Methanol, Isopropanol Wash
<b>Machine/Vendor</b>	Wet Bench (Marcus Inorganic)
<b>Process Specs</b>	<ol style="list-style-type: none"> <li>1. Pour Acetone on the wafer and wash off all the photoresist.</li> <li>2. Wash both sides of the wafer with Methanol.</li> <li>3. Wash both sides of the wafer with Isopropanol.</li> </ol>
<b>Time</b>	3 minutes or until all resist has been removed.
<b>Comments</b>	If resist is not coming off, soak in Acetone overnight and repeat the wash steps in 24 hours. Consider reducing the hard bake time if this occurs.



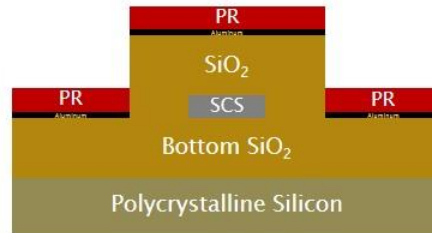
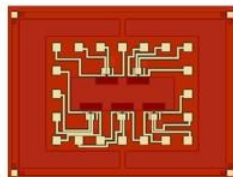
## FabStep 22: Photo Lithography Gold Metallization



Process		Spin Photo Resist	
Machine/Vendor	SCS GP38 Spinner (Marcus Inorganic)		
Process Specs	Resist Type: Negative (NR71-3000P) Spin Parameters: 3000RPM for 50 seconds	Ramp Up Rate: 500RPM/s (takes 6 seconds)	
Time	5 minutes per wafer		
Comments	Pre-bake in oven at 110°C for 3 minutes		
Process		Pattern Photo Resist	
Machine/Vendor	Karl Suss MA-6 TSA Mask Aligner (Marcus Inorganic)		
Process Specs	Channel: 1 (365nm Wavelength) Alignment Gap: 20µm	Contact Type: Hard Dosage: 66 mJ/cm²	MASK #4 (Clear Field)
Time	Measure lamp power. (Sample Power: 12.94 mW/cm² then 66/(12.9-1) = 5.5s exposure		
Comments	<ol style="list-style-type: none"> <li>1. Post-exposure bake in oven at 110°C for 3 minutes</li> <li>2. Develop in 500mL of RD-6 for 1 minutes one wafer at a time. Change every 3 wafers.</li> <li>3. DO NOT HARD BAKE</li> </ol>		



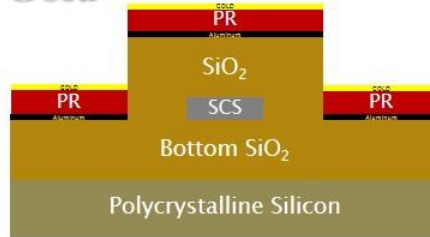
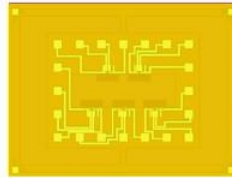
## FabStep 23: Descum



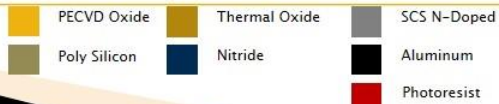
Process		Descum in Reactive Ion Etch	
Machine/Vendor	Vision RIE 2 (Marcus Inorganic)		
Process Specs	1. Use the standard descum recipe for 15 to 20 seconds		
Time	3 minute		
Comments	This is to clean the open areas of any resist that may be remaining on the surface to ensure gold metallization is successful.		



## FabStep 24: Metallization of Gold

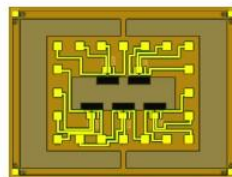


<b>Process</b>	Evaporate Aluminum Mirrors
<b>Machine/Vendor</b>	Denton Explorer (Marcus)
<b>Process Specs</b>	<ol style="list-style-type: none"> <li>1. 100 nm thick Platinum Barrier</li> <li>2. 50 nm thick Titanium Adhesion Layer</li> <li>3. 350 nm thick Gold Layer</li> <li>4. 1A/s Deposition Rate</li> <li>5. Wait for pressure to go below <math>9 \times 10^{-7}</math> Torr</li> </ol>
<b>Time</b>	2 Hours
<b>Comments</b>	May process up to 3 wafers each time. Insert a glass slide on the side, use tape to hold it in place. You can use the glass slide to measure deposited thickness using Dektak 150 Profilometer.



30

## FabStep 25: Resist Removal

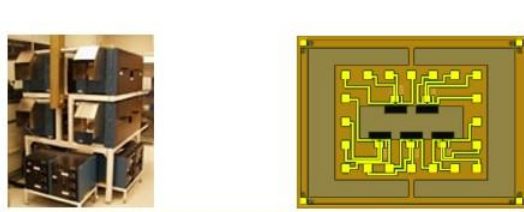
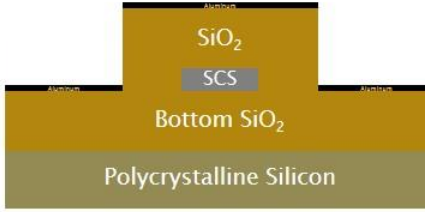


<b>Process</b>	Acetone, Methanol, Isopropanol Wash
<b>Machine/Vendor</b>	Wet Bench (Marcus Inorganic)
<b>Process Specs</b>	<ol style="list-style-type: none"> <li>1. Pour Acetone on the wafer and wash off all the photoresist.</li> <li>2. Wash both sides of the wafer with Methanol.</li> <li>3. Wash both sides of the wafer with Isopropanol.</li> </ol>
<b>Time</b>	3 minutes or until all resist has been removed.
<b>Comments</b>	If resist is not coming off, soak in Acetone overnight and repeat the wash steps in 24 hours. Consider reducing the hard bake time if this occurs.



31

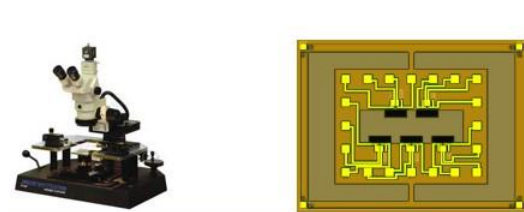
## FabStep 26: Annealing for Enhancing Gold Bonding

<b>Process</b>	<b>Annealing to Improve Bonding Between Gold and Piezoelements</b>
<b>Machine/Vendor</b>	Lindberg Furnace (Petit)
<b>Process Specs</b>	1. At 330C for 2 Hours
<b>Time</b>	Cool down to room temperature overnight (12-13 hours)
<b>Comments</b>	



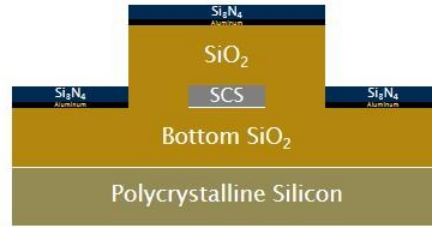
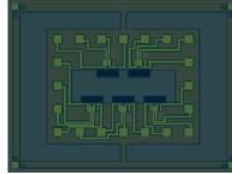
## FabStep 27: Inspection




<b>Process</b>	<b>Check Resistance Values to Verify Contacts</b>
<b>Machine/Vendor</b>	Singatone Probe Station (Marcus Inorganic)
<b>Process Specs</b>	1. Test dies B8,F3,I2,N3,R7,A8,E8,M8,I15,F14,N14 record resistance values for each. 2. Inspect each die for quality of gold adhesion.
<b>Time</b>	1 Hour
<b>Comments</b>	Decide whether further annealing is necessary.

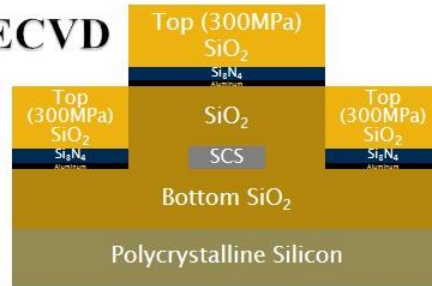
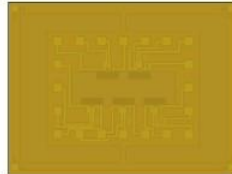


## FabStep 28: Deposition of PECVD Nitride Passivation Layer



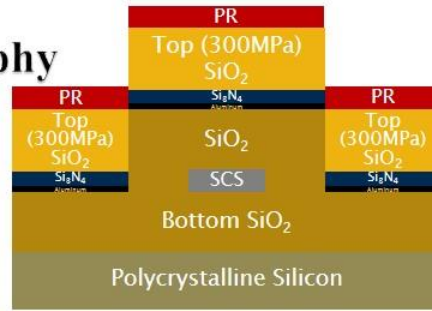
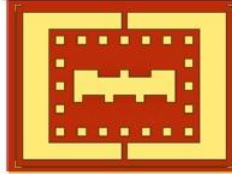
<b>Process</b>	<b>Deposit PECVD Nitride to Insulate Gold Wires</b>
<b>Machine/Vendor</b>	Oxford ICP PECVD (Marcus Inorganic)
<b>Process Specs</b>	1. Standard Recipe at room temperature. 2. Deposit a thickness of 100nm
<b>Time</b>	1 Hour
<b>Comments</b>	May use other PECVD systems for this step as long as temperatures are kept lower than 300C.

## FabStep 29: Deposition of PECVD Stress Compensated Oxide

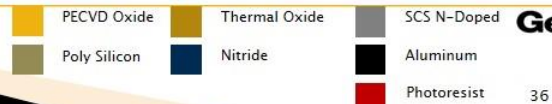


<b>Process</b>	<b>Deposit PECVD Oxide With -300MPa (Compressive Stress)</b>
<b>Machine/Vendor</b>	STS PECVD 2 (Petit)
<b>Process Specs</b>	1. Use iestdiox if it is still available. 2. Ratio of N <sub>2</sub> O/SiH <sub>4</sub> should be: 157 with 450 SCCM/2.8 SCCM. 3. Deposition Rate: 6.78 A/sec (9 minutes 48 seconds for 4000A)
<b>Time</b>	1 Hour
<b>Comments</b>	MUST USE THIS TOOL TO GENERATE -300MPa Stressed Oxide.

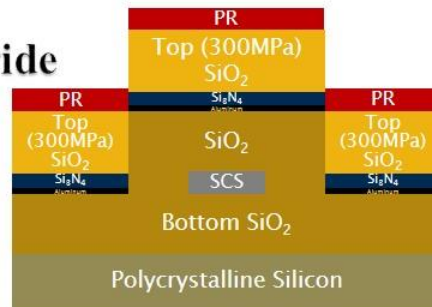
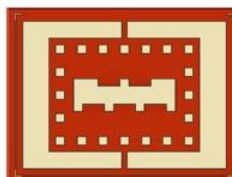
## FabStep 30: Photo Lithography Contact Opening



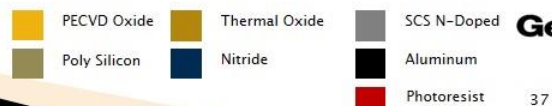
<b>Process</b>	<b>Spin Photo Resist</b>		
<b>Machine/Vendor</b>	SCS GP38 Spinner (Marcus Inorganic)		
<b>Process Specs</b>	Resist Type: Negative (NR71-300P) Spin Parameters: 3000RPM for 50 seconds	Ramp Up Rate: 500RPM/s (takes 6 seconds)	
<b>Time</b>	5 minutes per wafer		
<b>Comments</b>	Pre-bake in oven at 110°C for 3 minutes		
<b>Process</b>	<b>Pattern Photo Resist</b>		
<b>Machine/Vendor</b>	Karl Suss MA-6 TSA Mask Aligner (Marcus Inorganic)		
<b>Process Specs</b>	Channel: 1 (365nm Wavelength) Alignment Gap: 20µm	Contact Type: Hard Dosage: 66 mJ/cm²	MASK #5 (Clear Field)
<b>Time</b>	Measure lamp power. (Sample Power: 12.94 mW/cm2 then 66/(12.9-1) = 5.5s exposure		
<b>Comments</b>	<ol style="list-style-type: none"> <li>1. Post-exposure bake in oven at 110°C for 3 minutes</li> <li>2. Develop in 500mL of RD-6 for 1 minutes one wafer at a time. Change every 3 wafers.</li> <li>3. DO NOT HARD BAKE</li> </ol>		



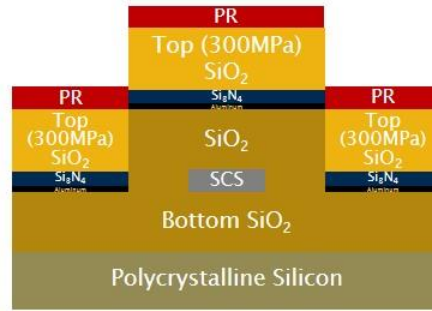
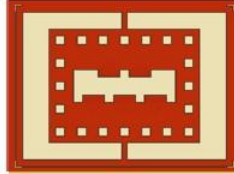
## FabStep 31: Etch Oxide/Nitride



<b>Process</b>	<b>Remove Oxide and Nitride from Contact Pads and Define Die/Cantilever Shapes</b>		
<b>Machine/Vendor</b>	Vision RIE 2 (Marcus Inorganic)		
<b>Process Specs</b>	<ol style="list-style-type: none"> <li>1. Use the Standard Oxide etch to remove 400nm of Oxide (25 minutes 168A/min)</li> <li>2. Use the Standard Nitride etch to remove 100nm of Oxide (15 minutes)</li> <li>3. If necessary, etch remaining SiO<sub>2</sub> at this time so that Poly Silicon Layer is seen.</li> </ol>		
<b>Time</b>	1 Hour		
<b>Comments</b>	At the end of the process contact pads should be open with no dielectrics and the Polycrystalline Silicon layer should be seen (check with Nanospec).		



## FabStep 32: Inspection Under Nanospec



Process	Inspection Under Nanospec
Machine/Vendor	Nanospec Refractometer (Marcus Inorganic)
Process Specs	1. Use Oxide on Silicon recipe to make sure all SiO <sub>2</sub> is gone.
Time	5 minutes
Comments	Remember to calibrate before every use.

PECVD Oxide
 Thermal Oxide

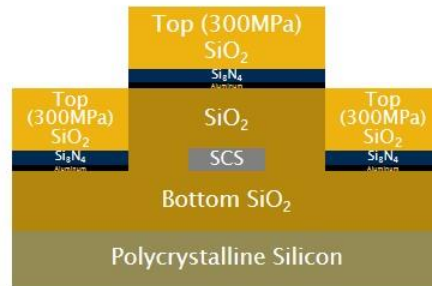
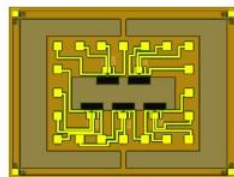
Nitride
 SCS N-Doped

Poly Silicon
 Aluminum

Photoresist

38

## FabStep 33: Resist Removal



Process	Acetone, Methanol, Isopropanol Wash
Machine/Vendor	Wet Bench (Marcus Inorganic)
Process Specs	1. Pour Acetone on the wafer and wash off all the photoresist. 2. Wash both sides of the wafer with Methanol. 3. Wash both sides of the wafer with Isopropanol.
Time	3 minutes or until all resist has been removed.
Comments	If resist is not coming off, soak in Acetone overnight and repeat the wash steps in 24 hours. Consider reducing the hard bake time if this occurs.

PECVD Oxide
 Thermal Oxide

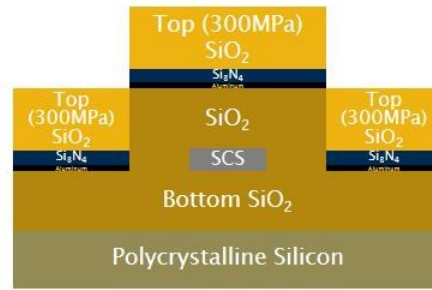
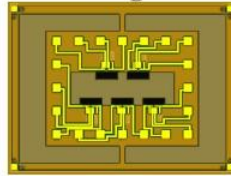
Nitride
 SCS N-Doped

Poly Silicon
 Aluminum

Photoresist

39

## FabStep 34: Inspection of Backside Under Nanospec



<b>Process</b>	Check Thickness of SiO <sub>2</sub> on the Back Side of the Wafer
<b>Machine/Vendor</b>	Nanospec Refractometer (Marcus Inorganic)
<b>Process Specs</b>	1. Use Oxide on Silicon recipe to measure thickness of SiO <sub>2</sub> . (Expected 400nm)
<b>Time</b>	5 minutes
<b>Comments</b>	Remember to calibrate before every use.

PECVD Oxide

Thermal Oxide

SCS N-Doped

Poly Silicon

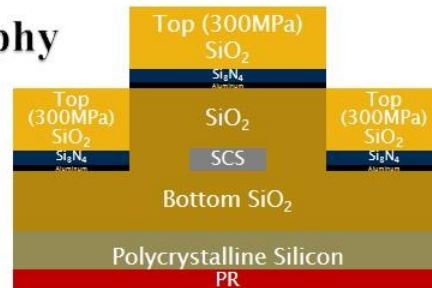
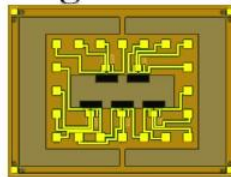
Nitride

Aluminum

Photoresist

40

## FabStep 35: Photo Lithography Backside Patterning



<b>Process</b>	Spin Photo Resist		
<b>Machine/Vendor</b>	SCS GP38 Spinner (Marcus Inorganic)		
<b>Process Specs</b>	First Spin: HMDS (P-20) Then Spin: Positive (SPR-220-7)	Spin Parameters: 2000RPM for 50 seconds Ramp Up Rate: 500RPM/s (takes 4 seconds)	
<b>Time</b>	5 minutes per wafer		
<b>Comments</b>	Pre-bake in oven at 110°C for 3 minutes		
<b>Process</b>	Pattern Photo Resist (Backside Alignment)		
<b>Machine/Vendor</b>	EVG-620 Mask Aligner (Marcus Inorganic)		
<b>Process Specs</b>	Exposure Wavelength: 365nm Alignment Gap: 50µm	Contact Type: Hard Dosage: 625 mJ/cm <sup>2</sup>	MASK #6 (Dark Field FeO <sub>2</sub> )
<b>Time</b>	Measure lamp power. (Sample Power: 5 mW/cm <sup>2</sup> then 625/(5-1) = 156.25s exposure		
<b>Comments</b>	<ol style="list-style-type: none"> <li>1. Post-exposure bake in oven at 110°C for 3 minutes</li> <li>2. Develop in 500mL of MF-319 for 4 minutes one wafer at a time. Change every 3 wafers.</li> <li>3. Hard Bake: 5 minutes in oven at 110°C</li> </ol>		

PECVD Oxide

Thermal Oxide

SCS N-Doped

Poly Silicon

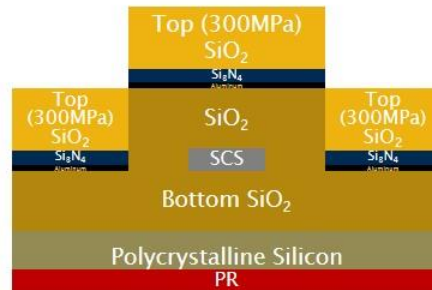
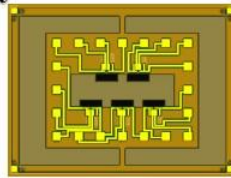
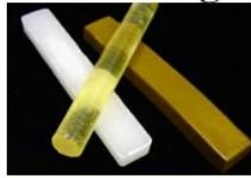
Nitride

Aluminum

Photoresist

41

## FabStep 36: Attach Carrier Wafer Using CrystalBond

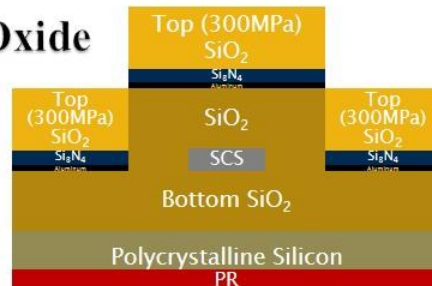
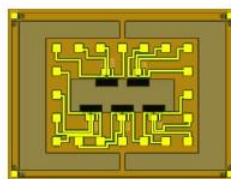


<b>Process</b>	Attach Carrier Wafer Wafer to Prepare for Backside Etch
<b>Machine/Vendor</b>	Hotplate (Marcus Inorganic)
<b>Process Specs</b>	<ol style="list-style-type: none"> <li>1. Preheat the hot plate to 130°C</li> <li>2. Place carrier wafer and some crystal bond and let melt for 5 minutes</li> <li>3. Use razor blade to achieve an even coat on the surface</li> <li>4. Place process wafer face down, backside up on the carrier wafer.</li> <li>5. Apply pressure at photoresist free spots and align the wafers.</li> <li>6. Remove and let cool down for 5 minutes</li> <li>7. Clean the carrier wafer with acetone to remove any crystalbond on the carrier wafer.</li> </ol>
<b>Time</b>	30 minutes
<b>Comments</b>	Make sure to cover hotplate with a clean aluminum sheet.



42

## FabStep 37: Etch Backside Oxide Layer

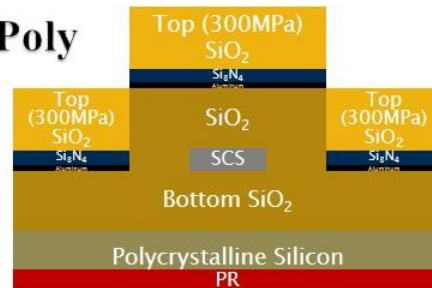
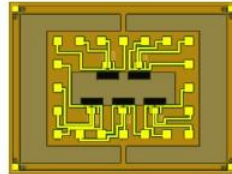


<b>Process</b>	Remove Oxide and Nitride from Contact Pads and Define Die/Cantilever Shapes
<b>Machine/Vendor</b>	Vision RIE 2 (Marcus Inorganic)
<b>Process Specs</b>	<ol style="list-style-type: none"> <li>1. Use the Standard Oxide etch to remove all oxide on the back (168A/min).</li> </ol>
<b>Time</b>	30 minutes for 400nm
<b>Comments</b>	Verify all oxide was removed with Nanospec refractometer. Repeat until all SiO <sub>2</sub> is gone.

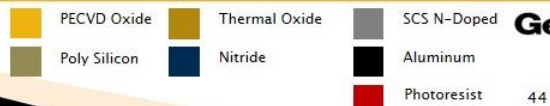


43

## FabStep 38: Deep RIE Etch Poly Silicon

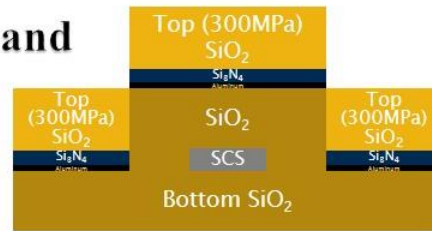
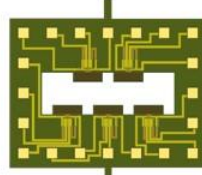


<b>Process</b>	Etch Polycrystalline Silicon All the Way Through
<b>Machine/Vendor</b>	STS HRM (Marcus Inorganic)
<b>Process Specs</b>	<ol style="list-style-type: none"> <li>1. Use IEGENMEMS recipe to etch most of the way through the wafer (400 cycles)</li> <li>2. Check state of release after 400 cycles</li> <li>3. If needed etch further 30 cycles.</li> <li>4. Check release state</li> <li>5. Repeat 3 and 4 until all devices have been released.</li> </ol>
<b>Time</b>	2 Hours (500 cycles)
<b>Comments</b>	Visually ensure all devices have been released (you should see mirrors appear in all the trenches).

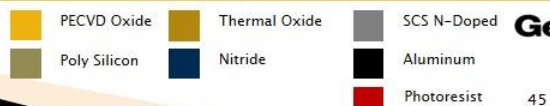


44

## FabStep 39: Resist Removal and Release



<b>Process</b>	Acetone, Methanol, Isopropanol Wash
<b>Machine/Vendor</b>	Wet Bench (Marcus Inorganic)
<b>Process Specs</b>	<ol style="list-style-type: none"> <li>1. Submerge in Acetone for 24 Hours.</li> <li>2. Remove all liquid using a syringe.</li> <li>3. Slide process wafer off of carrier wafer.</li> <li>4. Place process wafer in container and slowly fill with Acetone.</li> <li>5. Remove all liquid using a syringe.</li> <li>6. Repeat 4 and 5 for Methanol and then Isopropanol.</li> <li>7. Air Dry</li> </ol>
<b>Time</b>	25 Hours
<b>Comments</b>	Hard part is over, now go probe the 827 devices (3308 resistance values) X number of wafers you released.



45

## APPENDIX B: PACKAGING INSTRUCTIONS

### **Purpose**

Due to shipping damage to cantilever sensors a standardized packaging procedure is necessary. The following sections describe materials to be used as well as usage tips to maximize effectiveness of and reduce the likelihood of damage during shipping.

### **Testing Method and Results**

The following tests were conducted on three arrays of microcantilevers to verify the effectiveness of the packaging technique described in this paper. The following four tests were conducted. After every step images of the sensors were taken to verify no damage was sustained. These tests were limited and were designed to gauge effectiveness of packaging at preventing impact damage to the cantilevers. Further revision may be necessary if impact is not the primary mechanism causing the cantilever failure after shipping.

Each microcantilever was placed in a different container. First sample was placed in a GelPak 5 box, second sample was glued with double sided sticky tape to a regular box while the third sample was in Sandia gel pack box. The following tests were conducted on each sample separately.

#### Five Foot Drop

Package was dropped once from a height of five feet six inches. No damage was observed on packaging or microcantilevers.

#### Repeated Five Foot Drop

Package was dropped once on each side from a height of five feet six inches (resulting in a total of 6 consecutive drops per cantilever array). No damage was observed on packaging or microcantilevers.

#### Seven Foot Drop

Package was pushed from a shelf roughly 7' tall. No damage was observed on the package or on the microcantilevers.

#### Six Foot Toss into a Wall

Package was tossed into a wall once. Physical damage to the package was observed (slight bending of package corners), however, cantilevers were undamaged.

Effectiveness of Packaging Technique

The process described above resulted in no visible damage to the microcantilevers. These results were achieved independent of the box used to store the device. A small gelpack box was earlier thought to have caused damage to cantilevers during shipping. It was hypothesized that adhesion to the gel in the Sandia box was insufficient, however, this was not upheld in testing. A residue on the bottom of the cantilever array may have resulted in poor adhesion, as inferior adhesion of the said device was observed in all three tested boxes (adhesion to Sandia package is especially bad with in presence of residue).

## **Suggested Packaging Procedure**

### Materials

For images of each step see appendix.

1. A cardboard box roughly 6 X 6 X 4 inches.
2. A cardboard box with minimum dimensions of: 10 X8 X 6 inches.
3. Large bubble shipping envelope
4. Foam (or bubble wrap, packaging paper, airbags).
5. Regular 3/4in tape.
6. GelPak 5 or higher box (or double sided sticky tape with regular box).
7. Large 4”X4” wafer box.
8. ¼” Kapton Tape
9. 2” wide tape

### Warnings

1. MAKE SURE NOTHING IS LOOSE IN EVERY STEP. NOTHING IN THE PACKAGE SHOULD RATTLE WHEN YOU ARE DONE. PACK PACKAGING MATERIAL TIGHTLY.
2. ONE MICROCANTILEVER ARRAY PER EACH SMALL PLASTIC GEL PACK BOX.
3. NO MORE THAN 9 GEL PACK BOXES PER WAFER SIZED BOX.
4. AVOID TOUCHING THE TOP SURFACE OF THE CANTILEVER CHIP WITH TWEEZERS (HANDLE BY TABS ON THE SIDE). USE AN ERASER IF YOU NEED TO APPLY PRESSURE (TO ADHERE TO THE GEL).
5. PLEASE DO NOT THROW AWAY THE BOXES WHEN THEY ARRIVE. REUSE THEM IF THEY ARE IN GOOD CONDITION.

### Procedure

\*For a printable pictorial sequence please refer to last section\*

1. Place sensor in the center of the gel pack box.
2. Place up to 4 gel pack boxes in a large wafer box one at a time. If using less than 4 gel packs, tape each box separately to the bottom of the large wafer box with regular tape. You must tape it in at least two spots (one piece on each side of the box). Make sure the boxes can't move within the large container.
3. Place one layer of bubble wrap to further secure the gel packs inside the large box.
4. Close the large container and tape it shut on at least three sides.
5. Place large wafer container in bubble wrap envelope and wrap it around itself until it resembles the shape of the container box.
6. Place a thin (1/2inch) layer of foam (or bubble wrap) at the bottom of the large cardboard box.
7. Place the small cardboard box inside the center of the large cardboard box and place foam on all four sides so that the small box is held tight inside the large box (or pad with paper or bubble wrap).
8. Place the bubble wrapped container in the small box. Pad with foam and tape the small box shut.
9. Tape the large box shut and place the following labels on all four sides (see Appendix B for sample label):

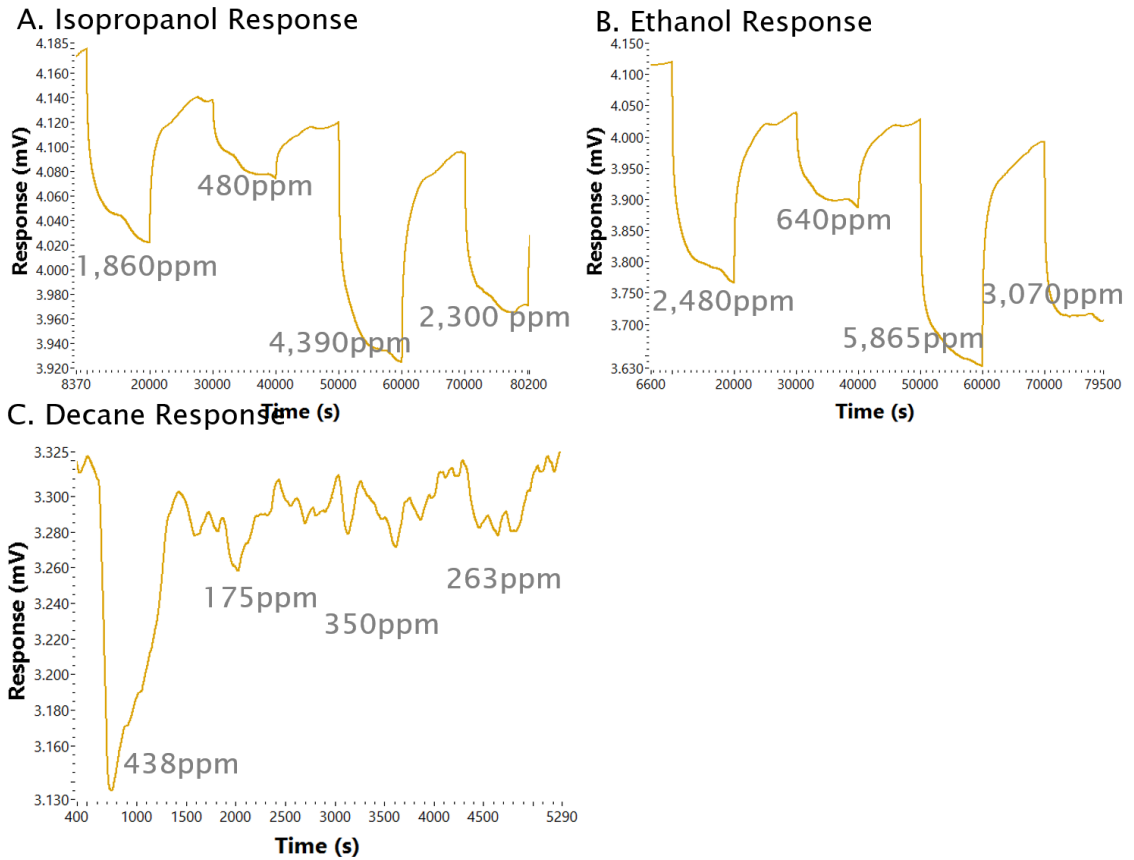
- a. "Fragile"
  - b. "Handle With Care. Thank You."
  - c. Arrows pointing in the direction of the top of the box with "UP" written somewhere in proximity.
10. Place shipping information on top of the box and it is ready to be mailed.
- \*\*PLEASE KEEP ALL PACKAGING MATERIALS WHEN THE PACKAGE ARRIVES AND REUSE IT WHEN YOU SEND THE SAMPLE BACK UNLESS THE BOX IS PHYSICALLY DAMAGED\*\***

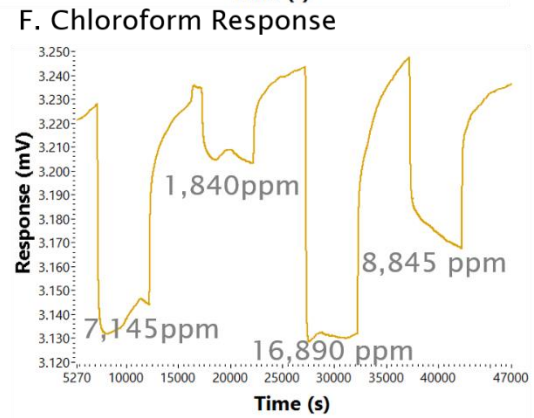
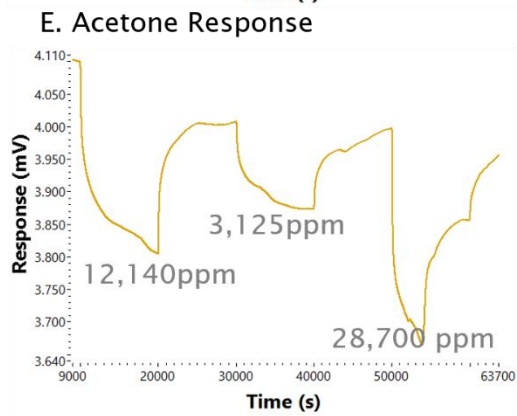
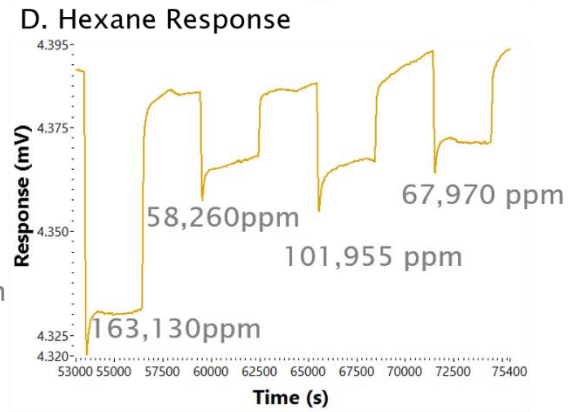
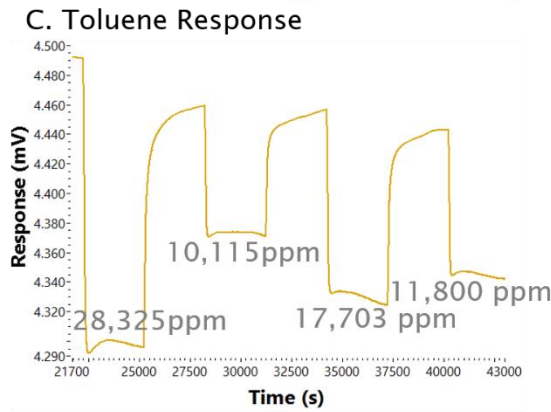
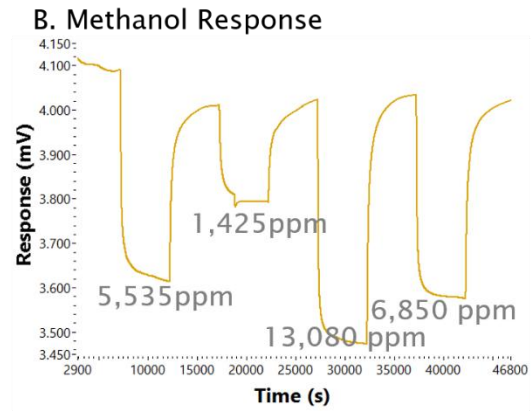
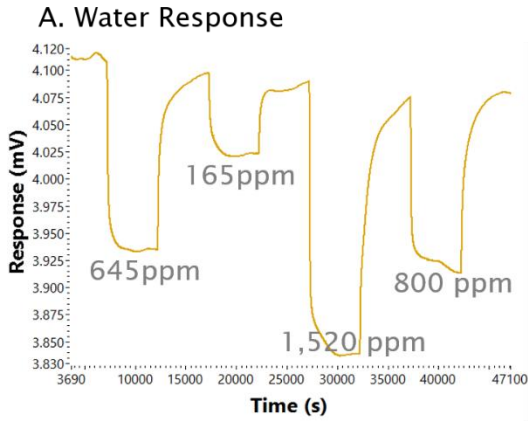
## Pictorial Guide



## APPENDIX C: SAMPLE RESPONSE DATA

Plots below show response of nine analytes side by side. Response was measured on old type piezoresistive microcantilevers with HKUST-1 (CuBTC) MOF. 40 cycles of deposition on SAM.





## REFERENCES

- [1] S. K. Vashist, "A Review of Microcantilevers for Sensing Applications," *Journal of Nanotechnology Online*, vol. 10.2240/azojono0115, pp. 1-15, 2007.
- [2] T. Thundat, P. I. Oden and R. J. Warmack, "Microcantilever Sensors," *Microscale Thermophysical Engineering*, vol. 1, no. 3, pp. 185-199, 1997.
- [3] L. A. Beardslee, J. Lehmann, C. Carron, J. J. Su, F. Josse, I. Dufour and O. Brand, "Thermally Actuated Silicon Tuning Fork Resonators for Sensing Applications in Air," in *IEEE International Conference on Micro Electro Mechanical Systems*, Paris, 2012.
- [4] C. Liu, *Foundations of MEMS*, Upper Saddle River: Prentice Hall, 2011.
- [5] J. Nakhla, "Metal Organic Frameworks (MOFs)," *Aldrich ChemFiles*, vol. 9, no. 2, p. 19, 2009.
- [6] D. Farrusseng, *Metal-Organic Frameworks: Applications from Catalysis to Gas Storage*, Weinheim: Wiley, 2011.
- [7] A. L. Robinson, V. Stavila, T. R. Zeitler, M. I. White, S. M. Thornberg, J. A. Greathouse and M. D. Allendorf, "Ultrasensitive Humidity Detection Using Metal-Organic Framework-Coated Microsensors," *American Chemical Society*, vol. 84, pp. 7043-7051, 2012.
- [8] J.-R. Li, R. J. Kuppler and H.-C. Zhou, "Selective Gas Adsorption and Separation in Metal-Organic Frameworks," *Chemical Society Reviews*, vol. 38, no. 5, pp. 1477-1504, 2009.
- [9] S. T. Meek, J. A. Greathouse and M. Allendorf, "Metal-Organic Frameworks: A Rapidly Growing Class of Versatile Nanoporous Materials," *Advanced Materials*, vol. 23, pp. 249-267, 2011.
- [10] O. Shekhah, S. K. H. Wang and F. S. e. al., "Step-by-Step Route for the Synthesis of Metal-Organic Frameworks," *Journal of the American Chemical Society*, vol. 129, no. 49, pp. 15118-15119, 2007.
- [11] L. E. Kreno, K. Leong, O. K. Farha, M. Allendorf, R. V. Duyne and a. J. T. Hupp, "Metal-Organic Framework Materials as Chemical Sensors," *Chemical Reviews*, vol. 112, no. 2, pp. 1105-1125, 2012.
- [12] V. Stavila, J. Volponi, A. M. Katzenmeyer, M. C. Dixon and M. D. Allendorf, "Kinetics and Mechanism of Metal-Organic Framework Thin Film Growth: Systematic Investigation of HKUST-1 Deposition on QCM Electrodes," *Chemical Science*, vol. 3, pp. 1531-1540, 2012.
- [13] C. Carbonell, I. Imaz and D. MasPOCH, "Single-Crystal Metal-Organic Framework Arrays," *Journal of American Chemical Society*, vol. 133, pp. 2144-2147, 2011.
- [14] J.-H. Lee, R. Houk, J. A. Greathouse, M. D. Allendorf and P. J. Hesketh, "Microcantilever Array Sensors Using Nanoporous Metal-Organic Frameworks (MOFS) for Gas Detection," in *Hilton Head Sensors and Actuators Workshop*, Hilton Head, 2010.

- [15] K. S. Park, Z. Ni, A. P. Cote, J. Y. Choi, R. Huang, F. J. Uribe-Romo, H. K. Chae, M. O'Keeffe and O. M. Yaghi, "Exceptional Chemical and Thermal Stability of Zeolitic Imidazolate Frameworks," *PNAS*, vol. 103, no. 27, pp. 10186-10191, 2006.
- [16] X. Zou, G. Zhu, I. J. Hewitt, F. Sun and S. Qiu, "Synthesis of a Metal-Organic Framework Film by Direct Conversion Technique for VOCs Sensing," *The Royal Society of Chemistry*, no. 16, pp. 3009-3013, 2009.
- [17] R. C. Huxford, J. Rocca and W. Lin, "Metal-Organic Frameworks as Potential Drug Carriers," *Current Opinion in Chemical Biology*, vol. 14, no. 2, pp. 262-268, 2010.
- [18] A. Choudhury, "A Piezoresistive Microcantilever Array for Chemical Sensing Applications," Dissertation at Georgia Institute of Technology, Atlanta, 2007.
- [19] S. K. Henniger, F. P. Schmidt and H. M. Henning, "Water Adsorption Characteristics of Novel Materials for Heat Transformation Applications," *Applied Thermal Engineering*, vol. 30, pp. 1692-1702, 2010.
- [20] G. Pahl, W. Beitz, K. Wallace, L. Blessing and F. Bauert, *Engineering Design: A Systematic Approach*, Springer, 1995.
- [21] A. Venkatasubramanian, J.-H. Lee, V. Stavila, A. Robinson, M. D. Allendorf and P. J. Hesketh, "MOF @ MEMS: Design Optimization for High Sensitivity Chemical Detection," *Sensors and Actuators B: Chemical*, vol. 168, pp. 256-262, 6/20/2012.
- [22] S. R. L. and D. Scott, "An Integrated Sensor for Electrochemical Measurements," *IEEE Transactions on Biomedical Engineering*, vol. 33, no. 2, pp. 83-90, 1986.
- [23] G. Yoshikawa, T. Akiyama, S. Gautsch, P. Vettiger and H. Rohrer, "Nanomechanical Membrane-type Surface Stress Sensor," *Nano Letters*, vol. 11, p. 1044, 2011.
- [24] G. Yoshikawa, T. Akiyama, F. Loizeau, K. Shiba, S. Gautsch, T. Nakayama, P. Vettiger, N. F. De Rooij and M. Aono, "Two Dimensional Array of Piezoresistive Nanomechanical Membrane-Type Surface Stress Sensor (MSS) with Improved Sensitivity," *Sensors*, vol. 12, p. 15873, 2012.
- [25] I. Ellern, A. Venkatasubramanian, J. H. Lee, P. J. Hesketh, V. Stavila, M. D. Allendorf and A. L. Robinson, "Characterization of Piezoresistive Microcantilever Sensors with Metal Organic Frameworks for the Detection of Volatile Organic Compounds," *ECS Transactions*, vol. 50, no. 12, pp. 469-476, 2012.
- [26] W. M. Rohsenow and H. Choi, *Heat Mass and Momentum Transfer*, New York: Prentice Hall, 1961.
- [27] D. Farruseng, C. Daniel, C. Gaudillere, U. Ravon, Y. Schurmann, C. Mirodatos, D. Dubbeldam, H. Frost and R. Q. Snurr, "Heats of adsorption for seven gases in three metal-organic frameworks: Systematic comparison of experiment and simulation," *Langmuir*, vol. 25, pp. 7383-7388, 2009.
- [28] S. Brodiga, L. Regli, F. Bonino, E. Groppo, C. Lamberti, B. Xiao, P. S. Wheatley, R. E. Morris and A. Zecchina, "Adsorption properties of HKUST-1 toward hydrogen and other small molecules monitored by IR," *Physical Chemistry Chemical Physics*, vol. 9, pp. 2676-2685, 2007.
- [29] M. D. Allendorf, R. J. Houk, L. Andruszkiewicz, A. A. Talin, J. Pikarsky, A. Choudhury, K. A. Gall and P. J. Hesketh, "Stress-induced chemical detection using

- flexible metal-organic frameworks," *Journal of American Chemical Society*, vol. 130, pp. 14404-14405, 2008.
- [30] P. Chowdhury, C. Bikkina, D. Meister, F. Dreisbach and S. Gumma, "Comparison of adsorption isotherms on Cu-BTC metal organic frameworks synthesized from different routes," *Microporous and Mesoporous Materials*, vol. 117, no. 1, pp. 406-413, 2009.
- [31] E. Garcia-Perez, J. Gascon, V. Morales-Florez, J. M. Castillo, F. Kapteijn and S. Calero, "Identification of Adsorption Sites in Cu-BTC by Experimentation and Molecular Simulation," *Langmuir*, vol. 25, no. 3, pp. 1725-1731, 2009.
- [32] J. G. Speight, *Lange's Handbook of Chemistry Sixteenth Edition*, New York: McGraw-Hill Professional, 2005.
- [33] J. Liu, Y. Wang, A. I. Benin, P. Jakubczak, R. Willis and D. LeVan, "CO<sub>2</sub>/H<sub>2</sub>O Adsorption Equilibrium and Rates on Metal-Organic Frameworks: HKUST-1 and Ni/DOBDC," *Langmuir*, vol. 26, no. 17, pp. 14301-14307, 2010.
- [34] J. Moellmer, A. Moeller, F. Dreisbach, R. Glaeser and R. Staudt, "High pressure adsorption of hydrogen, nitrogen, carbon dioxide and methane on the metal-organic framework HKUST-1," *Microporous and Mesoporous Materials*, vol. 138, no. 1-3, pp. 140-148, 2011.
- [35] O. Yazaydin, A. I. Benin, S. A. Faheem, P. Jakubczak, J. J. Low, R. R. Willis and R. Q. Snurr, "Enhanced CO<sub>2</sub> Adsorption in Metal-Organic Frameworks via Occupation of Open-Metal Sites by Coordinated Water Molecules," *Chemistry of Materials*, vol. 21, no. 8, pp. 1425-1430, 2009.
- [36] AZoOptics, "New Method to Produce Metal-Organic Frameworks for Optics, Phononics Applications," 6 12 2012. [Online]. Available: <http://www.azooptics.com/News.aspx?newsID=16538>. [Accessed 9 03 2013].
- [37] S. Jin, H. Son, O. Farha, G. P. Wiederrecht and J. T. Hupp, "Energy Transfer from Quantum Dots to Metal-Organic Frameworks for Enhanced Light Harvesting," *Journal of the American Chemical Society*, vol. 135, no. 3, pp. 955-958, 2013.